Dissertation
submitted to the
Combined Faculties for the Natural Sciences and for Mathematics
of the Ruperto-Carola University of Heidelberg, Germany
for the degree of
Doctor of Natural Sciences

presented by
Diplom-Physiker Thomas Scholl
born in Speyer

Oral examination: 14.02.2006

Photon Path Lengths Distributions for Cloudy Skies

—

Their first and second-order moments inferred from high resolution oxygen A-Band spectroscopy

Referees: Prof. Dr. Klaus Pfeilsticker
Prof. Dr. Frank Arnold

Zusammenfassung

Der Strahlungstransport in der Atmosphäre bei Bewölkung stellt eine der bedeutendsten Herausforderungen der Klimamodellierung dar. Die vorliegende Arbeit soll einen Beitrag zum verbesserten Verständnis des Photonentransports in Wolken liefern. Hierzu wurde aus spektroskopischen Sauerstoff-A-Banden Messungen (760-780 nm) die Weglängenverteilung von zenit-gestreuten Photonen bestimmt. Für diese Messungen wurde eine bestehende Methode verbessert und optimiert. Im Vergleich zu früheren Arbeiten ist es nun möglich einzelne Spektren innerhalb weniger Sekunden mittels moderner CCD-Detektoren und eines optimierten Instrumentariums zu messen. Hierdurch wird über räumliche Skalen integriert, welche kleiner als die Skalen der Strahlungsglättung sind. Die Validierung der Methode wurde in zwei unabhängigen Studien durchgeführt. Zum einen wurde unter Verwendung verschiedener Verteilungsfunktionen gezeigt, dass zur Beschreibung der gemessenen Spektren die Annahme einer Weglängenverteilung notwendig ist. Zum anderen wurde mittels eines Monte Carlo Strahlungstransportmodells ein synthetisches Transmissionspektrum berechnet, hieraus eine Weglängenverteilung ermittelt und mit den Modellergebnissen verglichen. Die spektroskopischen Messungen für die Photonen Weglängenbestimmungen wurden zusammen mit anderen In-Situ Messungen während zweier europäischer Wolkenforschungskampagnen (BBC1 und BBC2) durchgeführt, die auf dem Forschungsgelände des KNMI in Cabauw/Niederlande im September 2001 und Mai 2003 stattfanden. Durch die Kombination mit anderen gemessenen Wolkenparametern wie optische Dicke, Flüssigwassergehalt und geometrischer Wolkendicke ist es gelungen, die Theorie der Photonendiffusion experimentell zu bestätigen. Die in dieser Arbeit vorgestellten Beobachtungen liefern einen (weiteren) Hinweis auf den anormalen Diffusionstransport solarer Photonen in Transmission bei komplizierten Bewölkungssituationen und die Notwendigkeit der Beschreibung des Photonentransports in Wolken durch Lévy Verteilung.

Abstract

Modelling radiative transfer in cloudy skies is one of the most challenging tasks in climate modelling. The goal of this thesis is to achieve an improved understanding of photon transport in clouds. For this purpose, photon path length distributions are retrieved from spectroscopic oxygen A-band measurements (760-780 nm). An existing measurement method is improved and optimized. In comparison to former studies, it is now possible to measure single skylight spectra within a few seconds of one another using modern CCD detectors and optimized instruments. This enables a reduction of the spatial resolution to scales smaller than the radiative smoothing scale. Two different studies are performed for the validation of the method. It is shown, that a distribution function must be assumed for the correct description of the measured spectra. Furthermore, an absorption spectrum is calculated using a Monte Carlo radiative transport model. This spectrum is used to retrieve a path length distribution, which is subsequently compared to the model result. The spectroscopic measurements for the photon path length distribution retrieval were performed simultaneously with other in-situ measurements during two dedicated European cloud research campaigns (BBC1 and BBC2) held at the KNMI experimental site in Cabauw/Netherlands in September 2001 and May 2003. The measurement of other cloud parameters like optical thickness, liquid water content and geometrical cloud extension makes it possible to experimentally prove a new theory of photon diffusion of cloudy sky for the first time. The presented observations provide (further) evidence for the anomalous diffusion transport of solar photons being transmitted by complicated cloud covers. It is also shown, that Lévy walks are well suited for the description of photon transport in clouds.

Contents

1 Introduction **11**

2 Theory **17**

2.1 Basics of Radiative Transfer - Definitions 17

2.2 Scattering 18

2.2.1 Rayleigh-Scattering 19

2.2.2 Mie-Scattering 20

2.2.3 Raman-Scattering 21

2.3 DOAS - Differential Optical Absorption Spectroscopy 22

2.4 Basics of the Oxygen A-Band Spectroscopy 26

2.4.1 Absorption Spectrum 26

3 Concepts **33**

3.1 Concepts of Cloudy Skies Radiative Transfer 33

3.1.1 Cloud optical depth 33

3.1.2 Transport Mean-Free Path 34

3.1.3 Liquid Water Path 34

3.1.4 Classical Diffusion Theory 35

3.1.5 Anomalous Diffusion 37

3.2 Photon Path Length Distributions 38

3.2.1 Lambert Beers Law 38

3.3 Measuring Photon Path Length Distributions 40

3.4 Spectral Line Properties 41

3.4.1 Line Strength 41

3.4.2 Line Shape 42
3.5 Spectrum Evaluation 45
3.5.1 Nonlinear Least Square Fit 45
3.6 Measured Spectra 47
3.7 Spectroscopic Model 48
3.8 Direct Light Measurements 50
3.9 Retrieval of Photon Path Length Distributions 50
3.9.1 Retrieval of in-cloud photon path 51

4 Instrumentation **57**
4.1 Grating Spectrometer 57
4.1.1 Instrumental set-up 58
4.2 Out Of Band Rejection 62
4.3 Direct Sun Measurements 64
4.4 Sensitivity Tests 66
4.5 Model calculation 71
4.5.1 The GESIMA cloud model 71
4.5.2 The GRIMALDI Monte Carlo Model 73
4.5.3 Validation Of The Modelled Oxygen A-Band Spectrum 76

5 Results **79**
5.1 The 4D Cloud Project 79
5.2 Case Studies 80
5.2.1 BBC1 Campaign September 2001 80
5.2.2 BBC2 Campaign May 2003 90
5.3 Discussion 110

6 Summary and Outlook **113**

A HITRAN **117**

B Andor basics **119**

List of Figures **125**

List of Tables 125

References 127

Acknowledgements 137

Chapter 1

Introduction

Clouds affect radiation through their three dimensional geometry and the amount, size and nature of the droplets they contain. Currently, the inability to properly model clouds and their radiative effects under present and future conditions is a major source of uncertainty in climate change forecasts. The possibility that models underestimate solar absorption in clouds remains a controversial matter. Probably the largest uncertainty in climate forecasts arises from clouds and their interactions with radiation. Consequently clouds are the greatest unknown in all of physical climate modelling. Here some aspects of the importance of detailed cloud studies are discussed shortly.

The knowledge of the influence of clouds on the radiative balance of the Earth's climate is very important for climate modelling and weather forecasts. Clouds influence the radiative balance mainly by two effects, which work against each other[1]. Solar radiation in the visible can pass high optically thin clouds without significant interference and reach the surface. On the other hand clouds reflect incoming solar radiation back into space and absorb the terrestrial infrared emission and emit it on the cloud's top at a lower temperature than the surface they overlie. In the long wave regime clouds emit only at low temperatures, leading to a net warming of the atmosphere and surface. Optical thick clouds in the middle and lower atmospheric layers allow only for passing of a small fraction of the incoming solar radiation. But they emit infrared radiation at higher temperatures than the ambient temperature and therefore longer wavelengths having a net cooling effect on the atmosphere. The competition between these two effects depends on cloud

[1]The interaction of clouds and radiation also involves for example the asymmetry factor of Mie scattering, which depends on cloud composition, and most notable on cloud phase. The subtle balance between cloud impact on the solar short-wave (SW) and terrestrial long-wave (LW) radiation may be altered by a change in any of these parameters. It is long known that clouds play an important but perhaps the least understood role in determining global climate.

thickness, height and radiative properties.

Radiation from the sun is the driving force of Earth's climate system. About half of the incoming radiation is in the infrared wavelength range. The other half is mostly in the visible short-wave range and a small amount in the ultraviolet. In total 342 Wm^{-2} reach the Earth on a global average. The surface of the Earth, the atmosphere and clouds reflect 31 percent or 107 Wm^{-2} of the incoming solar radiation back into space. The remaining radiation is absorbed in the atmosphere (67 Wm^{-2}) or warms the land and the ocean (168 Wm^{-2}). To maintain a radiation equilibrium a balance between outgoing terrestrial radiation and incoming solar radiation is required. Therefore most of the absorbed energy is emitted to space as long wave infrared radiation, see Figure 1.1.

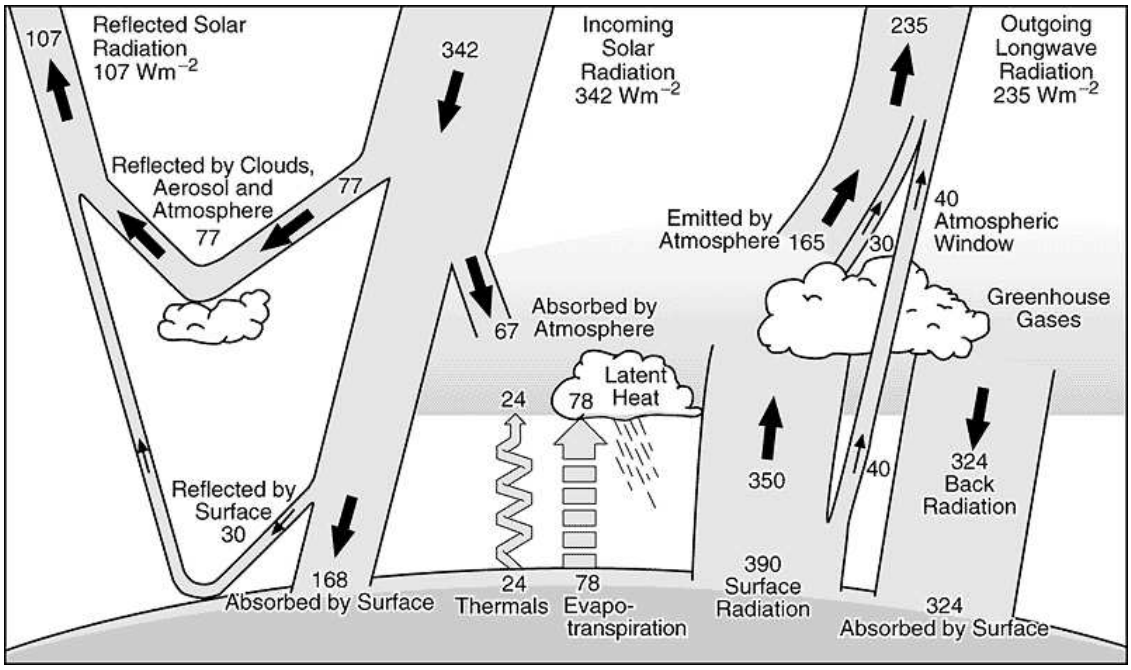

Figure 1.1: *Overview of the earth atmosphere energy balance. Left hand side the incoming shortwave solar radiation, right hand side the outgoing infrared terrestrial radiation [Houghton et al. 2001]*

Comparison between observation and Global Circulation Models (GCM) and the comparison of different GCMs shows large disagreements in the cloud radiation rate. This is caused mainly by GCM cloud treatments. The cloud radiative forcing in all models differs widely from the best satellite measurements. Commonly clouds are included in GCMs as plane parallel layers. This treatment does not account

for 3D effects. Therefore the Independent Pixel Approximation[2](IPA) is now used in GCMs, because of the improved computational possibilities. The IPA is an improvement for spatial averaged radiation but do not match the correct 3D calculated cloud feedback. Most GCMs used for climate simulations now also include interactive cloud optical properties and a more comprehensive representation of sub-grid scales and explicit microphysics. But the cloud optical feedbacks produced by these GCMs differ both in strength and sign. Even for a given water phase, the sign of the variation of cloud optical properties with temperature is a matter of controversy. But simulations with those advanced models demonstrate their capability to reproduce realistically many features of the cloud radiative forcing.
Progress have also been made in the qualitative understanding of the complexity of the relation of clouds and climate. There is also an important and ongoing evolution of the cloud parameterizations included in the models, which is characterized by a greater physical consistency and a greatly enhanced physical content. Because of the wide variety of interacting processes which contribute to cloud-radiation interaction or cloud formation, clouds remain a dominant source of uncertainty. Uncertainties exist in the understanding of microphysical processes controlling the growth and phase of cloud droplets or large-scale and sub-grid scale dynamic processes. Most of these processes need to be parameterized in climate models.

Even there is not much solar heating of the atmosphere, the knowledge of the radiative heating rate in the atmosphere is another important aspect of cloud science. Recent simulations of equilibrium climate with doubling of CO_2 indicate that the induced variation of net cloud radiative forcing short-wave or long-wave, ranges within $\pm$ 3 Wm^{-2}, which is a small fraction of the mean cloud long-wave warming (+30 to +35 Wm^{-2}) or mean cloud short wave cooling (-45 to -50 Wm^{-2}). But already a change by 1 Wm^{-2} in the radiational heating can cause a significant change in the precipitation rate. The correct simulation of the mean distribution of cloud cover and radiative fluxes is therefore a necessary but by no means sufficient test of a model's ability to handle realistically the cloud feedback processes relevant for climate change.

Detailed knowledge of cloud physics is required to properly characterize and model clouds, i.e. to improve weather forecast models. Thus it is important to have detailed data sets to describe different types of clouds. In the last decades the key properties of clouds are characterized by many remote-sensing measurements. The challenge of characterizing and understanding all the processes lies in putting

[2]The IPA bases on the assumption that the radiative transfer within each pixel occurs indipentently of neighboring pixels

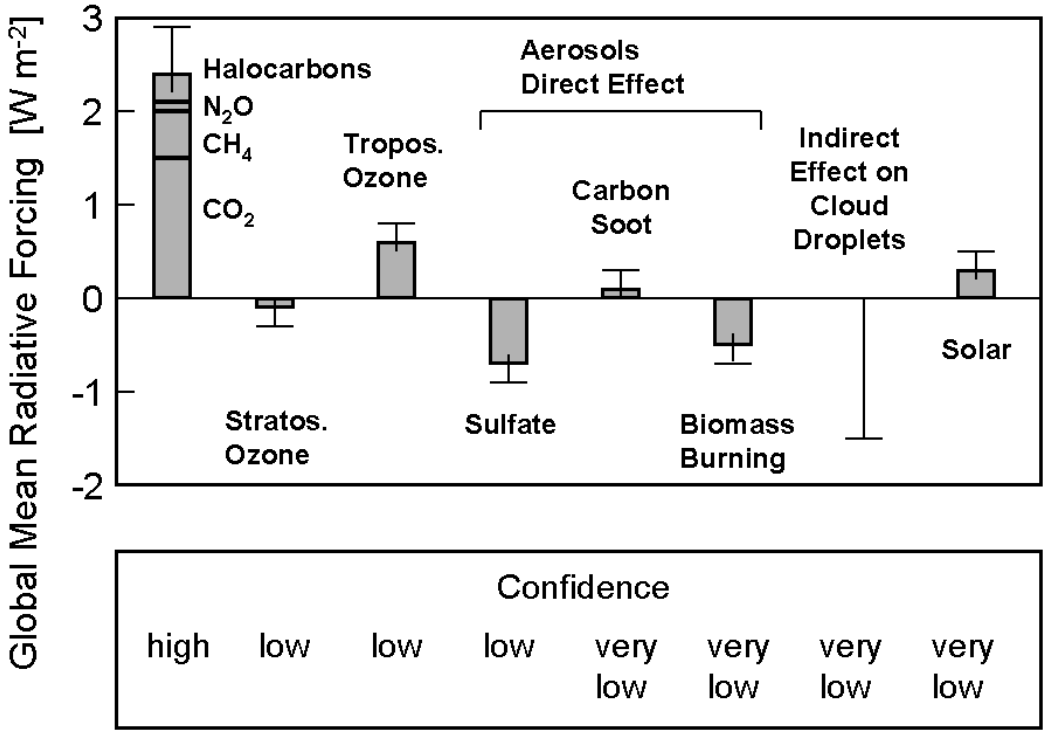

Figure 1.2: *Sources of uncertainties in climate modelling*

together all the measured quantities describing the complexity of clouds. The unique 4D Clouds project in the framework of the German AFO 2000 programm is an attempt to combine many different cloud research remote sensing measurements for a better understanding of cloud microphysics. Evaluation and improvement of existing cloud models using these data sets is a major aim of this project. The combination of the presented oxygen A-band measurements to retrieve photon path length distributions (PDF) and other cloud related quantities allows verification of existing radiative transfer theories and models.

Photon path length distribution is commonly a hidden property of standard radiative transfer models, controlled by the spatial distributions of scattering and absorption. The distribution in the near infrared region are very representative for the shortwave region as a whole. The principle of equivalence allows to draw conclusions about radiative properties of the atmosphere from a photon PDF measured in one wavelength band, since the scattering properties of clouds and aerosols vary slowly and predictably with wavelength. The technique to determine photon

path length distributions using absorption spectroscopy of the oxygen A-band has been primarily developed at the Institute for Environmental Physics in Heidelberg [*Pfeilsticker et al.* 1998; *Veitel et al.* 1998; *Funk* 1996; *Greiner* 1998; *Funk* 2000] and at the State University of New York, Albany [*Min et al.* 2001; *Min et al.* 2004]. An excellent overview of the background and theoretical aspects of photon PDF and 3D radiative transfer in cloudy can be found in *Marshak and Davis* [2005].

The prime objective of this study is to improve the experimental technique of photon path length distribution measurement and to test the applicability of a new theory of anomalous photon diffusion through clouds. The prime objective is achieved by using a CCD camera and a high resolution grating spectrometer. The underlying retrieval method is validated by analyzing a calculated absorption spectrum. Combining the spectroscopic measurements with other cloud properties measured simultaneously by in-situ techniques during two campaigns allows to test the theory of anomalous photon diffusion through clouds.

Outline of the thesis

In the *second chapter* an overview of the radiative processes in the Earth's atmosphere is given. Especially the different types of scattering processes occurring in the atmosphere are briefly discussed. Furthermore a short introduction to the DOAS technique and the spectroscopic basics of the oxygen molecule are presented.
An overview of the basic concepts used in this study is given on the *third chapter*. The theory of photon diffusion inside clouds is introduced. Beside the description of the relation between the different measured quantities, the basic ideas of the classical versus anomalous photon diffusion are discussed. Additional spectroscopic background for atmospheric stray light measurements and concepts used for the analysis and interpretation of the measured data are presented.
The *fourth chapter* is an overview of the used instrumentation for the oxygen A-band measurements. The spectroscopic system and several sensitivity studies to specify the used instrument are described. These enclose the measurement of the spectrometer's out-of-band rejection as well as the retrieval of the curve of growth from direct sun measurements. To validate the used method, a comparison between a cloud model (University of Kiel) and the spectra evaluation procedure (University of Heidelberg) is given. The radiative transfer calculations inside a modelled cloud are used to generate a simulated highly resolved oxygen A-band spectrum. The latter serves as input spectrum for the data evaluation algorithm to retrieve the photon path length distribution inside the model cloud.

The results from the A-band spectroscopic measurements for the BBC1[3] and BBC2 cloud campaigns are presented in the *fifth chapter*. For selected cloud scenarios the retrieved first two moments of the photon path length distributions ($\langle L_{tot} \rangle$ and $\langle L_{tot}^2 \rangle^{0.5}$) and additional measurements of the inner cloud structure and geometrical vertical extension (ΔH) and the liquid water path (LWP) are shown. Combination of these measurements allows to determine a Lévy index α and the ratio $\langle L_c^2 \rangle^{0.5} / \langle L_c \rangle$. These are used to validate the theory of classical vs anomalous photon diffusion inside clouds.
The final chapter summarizes the most important findings of this study and gives an outlook on further scientific work and perspectives.

[3]BBC: **B**altic **B**ridge **C**ampaign

Chapter 2

Theory

There are many processes in which radiation interacts with the atmosphere. As sunlight passes through the Earth's atmosphere it is subject to a variety of effects, such as refraction and scattering, in addition to the absorption. In the first two sections of this chapter the basic quantities of radiative transfer and the different scattering processes are briefly discussed. After this in the second part the principals of the Differential Optical Absorption Spectroscopy (DOAS) technique are described.

2.1 Basics of Radiative Transfer - Definitions

• The Radiation Flux Φ

The incident radiation energy per time is called the radiation flux Φ:

$$\Phi = \frac{\text{radiation energy}}{\text{time}} = \frac{\mathrm{dE}}{\mathrm{dt}}[W] \tag{2.1}$$

• The Spectral Flux $\Phi(\lambda)$

The spectral flux $\Phi(\lambda)$ is defined as Φ differentiated with respect to the wavelength λ:

$$\Phi_\lambda = \Phi(\lambda) = \frac{\text{radiation energy}}{\text{wavelength and time}} \frac{\mathrm{d}\Phi}{\mathrm{d}\lambda} = \frac{\mathrm{d}^2\mathrm{E}}{\mathrm{dt}\ \mathrm{d}\lambda}\left[\frac{W}{nm}\right] \tag{2.2}$$

• Specific Intensity or Radiance I_λ

The Specific Intensity or Radiance is the fundamental quantity defining the radiation field. It measures the spectral energy flux $\Phi(\lambda)$ in a given direction dA_E per unit time per solid angle $d\Omega$ per wavelength:

$$I_\lambda = I(\lambda) = \frac{\text{spectral flux}}{\text{solid angle and area}} = \frac{d^2\Phi_\lambda}{d\Omega \cdot dA_E} \left[\frac{W}{nm\ m^2\ sr}\right] \tag{2.3}$$

• Irradiance E_λ

The Spectral Irradiance is the radiance I_λ integrated over the half sphere considering the factor $\cos(\theta)$.

$$E_\lambda = \int_0^{2\pi} I_\lambda \cdot \cos(\theta) \cdot d\Omega \left[\frac{W}{nm\ m^2}\right] \tag{2.4}$$

where θ is the angle between the normal of dA_E and the incident radiation.

• Actinic Flux F_λ

The Actinic Flux F_λ determines the availability of photons at a certain point. It is gained by integration the radiance I_λ over the whole sphere. The direction of the radiance is not considered, i.e. neglecting $\cos(\theta)$.

$$F_\lambda = \int_0^{4\pi} I_\lambda \cdot d\Omega \left[\frac{W}{nm\ m^2}\right] \tag{2.5}$$

2.2 Scattering

Solar radiation passing through the atmosphere can undergo several scatter processes by atmospheric constituents. Scattering causes changes in the direction and the intensity of radiation. The probability of scattering depends on several factors including the wavelength of the radiation, the abundance of particles or gases, and the distance the radiation travels through the atmosphere. When the size of atmospheric particles with which the incoming radiation interacts is close to, or greater than, the wavelength of the radiation Mie scattering occurs. The equations describing Mie scattering may be derived by the solution of Maxwell's equations for the interaction of electromagnetic radiation with a dielectric spherical particle, the theory may be extended to non-spherical particles. It can be shown that the total cross section of Mie scattering shows very little variation with wavelength ($\sigma_{Mie} \sim \lambda^{-1.3}$), as is usually the case in the atmosphere, there is a large distribution of sizes amongst the scattering particles.

The theory of Rayleigh scattering describes the interaction of light with particles which are small compared to the wavelength of the radiation. Although it is usually

considered as a separate entity, and indeed was proposed earlier, Rayleigh scattering may be considered as the small particle (or long wavelength) limit of Mie scattering. In general, scattering decreases with increasing wavelength of the radiation. There are three types of scattering that take place. In this connection inelastic scattering processes have to be distinct from elastic processes. Raman scattering is inelastic molecular scattering, elastic is Rayleigh scattering. For Mie scattering the wavelength and the composition of the aerosol particle determine if inelastic (i.e. for liquid water droplets with large absorption at the considered wavelength) or elastic scattering occurs.

2.2.1 Rayleigh-Scattering

Rayleigh scattering occurs when particles are considerably smaller than the wavelength of the radiation. The assumption is valid when the scattering particles are less then 0.2 $\cdot\lambda$ in diameter. The incident electromagnetic wave produces a oscillating electric field E which generates a dipole configuration on the particle. The scattered light can be treated as radiation emitted by this excited oscillating dipole. Rayleigh scattering is inversely proportional to the fourth power of the wavelength λ^{-4}, causing shorter wavelengths of radiation to be scattered much more probable than longer wavelengths. This scattering is responsible for the blue color of the sky. Inspecting the free path length $\mathrm{l}_{Rayleigh} = 1/(\rho\sigma_{Rayleigh})$ for different wavelengths[1] yields that $\mathrm{l}_{Rayleigh} \sim 14$ km for UV light ($\lambda = 360$ nm), but ~ 50 km for blue light ($\lambda = 490$ nm) and ~ 160 km for red light ($\lambda = 650$ nm). The blue part of the spectrum is scattered more and reaches the ground from the entire hemisphere, while the red light reaches the ground directly from the sun. An accurate empirical formula for the total cross section $\sigma_{Rayleigh}$ is given by [*Nicolet* 1984]

$$\sigma_{Rayleigh} = \sigma_R = 4.02 \cdot 10^{-28}/\lambda^{4+x} cm^2 \tag{2.6}$$

where

$$\begin{aligned} x &= 0.389\lambda + 0.009426/\lambda - 0.3228 \qquad \text{for } 0.2\mu m < \lambda < 0.55\mu m \\ x &= 0.04 \qquad \text{for } \lambda > 0.55\mu m \end{aligned}$$

The differential cross section for unpolarized light is given by:

$$\frac{d\sigma_R}{d\Omega} = \sigma_R \cdot P_R(\Theta) \tag{2.7}$$

[1] ρ is the air density which is typically $2.7 \cdot 10^{19}$ cm^{-3} at ground level

The phase function $P_R(\Theta)$, describing the angular dependence of Rayleigh scattered radiation and the angle Θ between incident and scattered radiation, for unpolarized light is given by

$$P_R(\Theta) = \frac{3}{4}(1 + \cos^2 \Theta) \tag{2.8}$$

Taking into the anisotropy of the molecules, the phase function given by 2.8 is given by [*Penndorf* 1957]

$$P(\Theta) = 0.7629 \cdot (1 + 0.932 \cdot \cos^2 \Theta) \tag{2.9}$$

2.2.2 Mie-Scattering

Scattering from spherical particles of arbitrary dimensions is first treated by [*Mie* 1908]. Mie scattering occurs at particles with a linear dimension comparable to the wavelength of the radiation. To account for the particle size dependence of the Mie scattering, the size parameter $\alpha = 2\pi r/\lambda$, with particle radius r, is used. For a given α, the Mie extinction function $E(\alpha)$ can be calculated. In reality aerosols are a mixture of aerosols with different sizes described by the size distribution function n(r). For a known size distribution a macroscopical extinction coefficient $k_e(\lambda)$ can be calculated:

$$k_e(\lambda) = \int_0^\infty \pi r^2 E(\alpha) n(r) dr \tag{2.10}$$

For aerosols larger than 0.1 μm, n(r) usually obeys an r^{-s} dependence, with s≈4, which yields a simple wavelength dependence for k_e.

$$k_e(\lambda) \sim \lambda^{3-s} \tag{2.11}$$

This results in a far smaller wavelength dependence of Mie scattering compared to the Rayleigh case.

A frequently used analytical expression to describe the scattering phase function is the Henyey-Greenstein parameterization. It accounts for aerosol mixture by averaging over the different aerosol sizes weighted with their size distribution.

$$\Phi(\cos\vartheta) = \left(\frac{(1-g)^2}{4\pi(1+g^2-2g\cos\vartheta)}\right)^{3/2} \tag{2.12}$$

where the asymmetry factor g is

$$g = \langle\cos\vartheta\rangle = \frac{1}{2}\int_{-1}^{1} P(\cos\vartheta) \cdot \cos\vartheta \, d\cos\vartheta \tag{2.13}$$

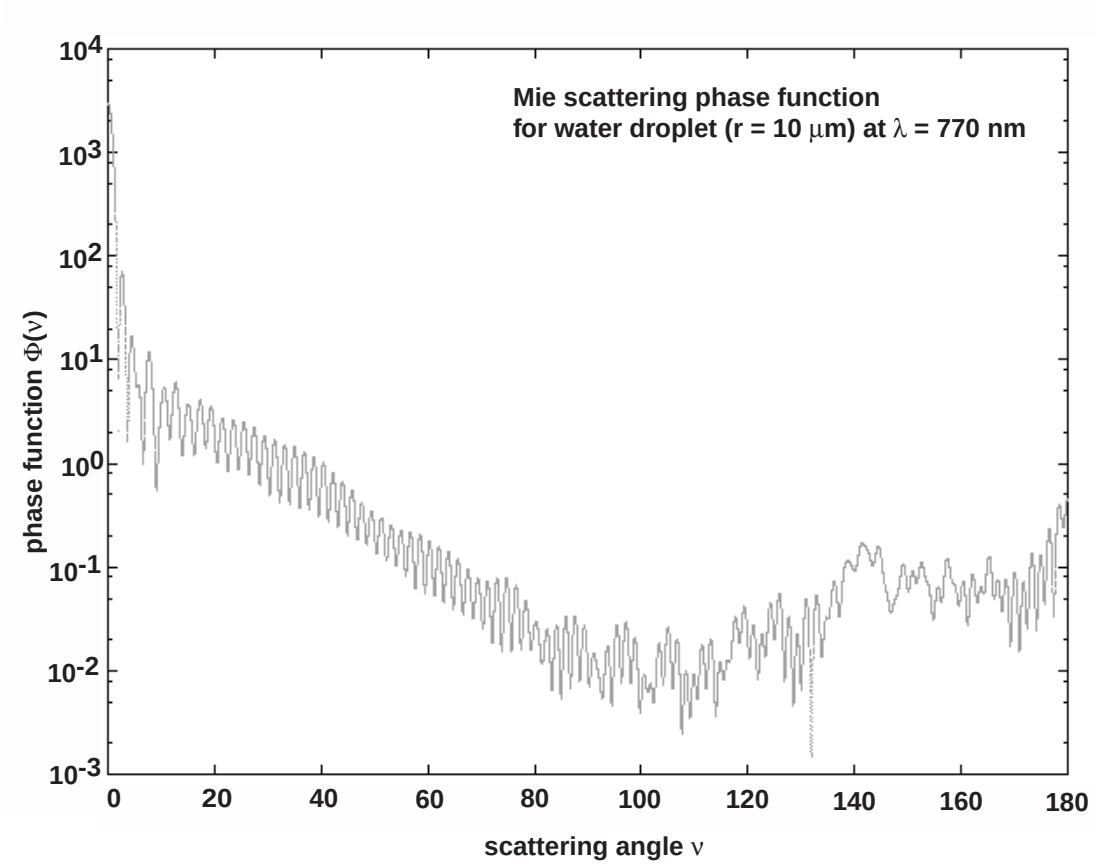

Figure 2.1: *Typical Mie scattering phase function for a cloud water droplet ($r = 10\ \mu m$) at wavelength $\lambda = 770$ nm, calculation tool provided by Sanghavi [2005].*

Typical values for cloud droplets are g $\sim$ 0.75 - 0.85 and g $\sim$ 0.6 -0.7 for tropospheric aerosol. Figure 2.1 shows an example of the phase function using Mie theory.

2.2.3 Raman-Scattering

Raman scattering depends upon the polarizability of the molecules. For polarizable molecules, the incident photon energy can excite vibrational and rotational modes of the molecules, yielding scattered photons which are altered in energy by the amount of the transition energies. If rotational excitation only is affected ($\Delta\nu = 0$), the term Rotational Raman Scattering (RRS) applies. The term Rotational-Vibrational Raman Scattering (RVRS) is used in the case that also the vibrational state ($\Delta\nu \pm 0$) changes. Only discrete amounts of energy given by the difference of the molecule's

excitation state before and after the scattering process can be absorbed or emitted, respectively. A spectral analysis of the scattered light under these circumstances shows several closely spaced vibrational Raman bands each consisting of several rotational Raman lines below and above a strong Rayleigh line. Such rotational Raman lines are called "Stokes lines" (ΔJ = +2, S-branch) and anti-Stokes lines (ΔJ = -2, O-branch).
For air, i.e. O_2, RVRS frequency shifts of up to $\pm$1555 cm^{-1} occur. For RRS $\pm$200 cm^{-1} for oxygen has to be added. Only RRS is usually regarded in atmospheric RT, as RRS is an order of magnitude stronger than the RVRS.
The RRS cross section is given by:

$$\sigma_{RRS} = \frac{256\pi\gamma^2 f_N b_{N,J,N',J'}}{27\lambda'^4} \tag{2.14}$$

with γ (given in [cm^3]) being the polarization anisotropy, b the Placzek-Teller coefficient, f_N the fractional populations in the initial state and λ' (given in [cm]) the wavelength of the shifted line. Detailed calculations of the σ_{RRS} for O_2 and N_2 can be found in *Haug* [1996], *Burrows et al.* [1996], *Sioris and Evans* [1999] and *Funk* [2000]. Latter developed a Raman scattering model to quantify the influence of Raman filling-in of oxygen absorption lines particularly with regard to the influence of the photon PDF retrieved from the absorption spectrum. In different case studies (different air masses) it has been shown that, Raman filling-in of oxygen lines in the A-band can be neglected. For the strong Fraunhofer line at 770.1 nm and for the oxygen line the maximum filling-in is lower than 1 ‰ for air mass of unity. For more than 10 air masses the filling in for the Fraunhofer lines can reach 1 %, as it scales lineary with the air column. For the oxygen lines it does not exceed 5 ‰ due to reduction by additional absorption.

Measurements of scattered sunlight are affected by Rotational Raman scattering which is connected to the Raman filling-in of Fraunhofer-lines, also referred as Ring effect, see [*Grainger and Ring* 1962]. This spectral artifact can also affect strong atmospheric absorption lines, like the oxygen A-band vibrational and rotational absorption lines.

2.3 DOAS - Differential Optical Absorption Spectroscopy

Absorption spectroscopy is an important tool for the analysis of the Earth's atmosphere. It has played an outstanding role in the discovery of the chemical and

physical properties of the atmosphere.
Light with intensity $I_0(\lambda)$ emitted by the sun passes the atmosphere. Along the light path the original intensity is reduced through the absorption of different gaseous species e.g. oxygen, but also scattering due to aerosol particles and air molecules, (see section 2.2). Both processes are called extiction.
For a description of the light attenuation through the atmosphere, Lambert-Beers law is used. For a thin layer dl the attenuation of light with fixed wavelength λ can be described by:

$$dI(\lambda) = -\alpha_\lambda \, I(\lambda) \, dl \tag{2.15}$$

with $\alpha = \alpha_{a,\lambda} + \alpha_{s,\lambda}$ being the overall extinction as the sum of the absorption and scattering coefficients, α_a and α_s, respectively. To account for all possible absorbers it is necessary to sum all present absorbers i. The individual absorption coefficient $\alpha_{a,\lambda,i}$ contains the particle density n_i and the corresponding absorption cross section σ_i. The total absorption coefficient is given by:

$$\alpha_{a,\lambda} = \sum_i \sigma_i(\lambda) n_i \tag{2.16}$$

As described in section 2.2 three scattering processes are possible in the Earth's atmosphere. Neglecting inelastic Raman scattering, the important scattering processes are Mie scattering at cloud droplets and aerosols and Rayleigh scattering at air molecules. With the particle density n and the scattering cross section σ for the different scattering processes, the overall scattering coefficient α_s is given by:

$$\alpha_{s,\lambda} = \sigma_M(\lambda) n_M + \sigma_R(\lambda) n_R \tag{2.17}$$

The ratio between the absorption coefficient and the total extinction is called single scattering albedo:

$$\omega_0 = \frac{\alpha_s}{\alpha_s + \alpha_a} \tag{2.18}$$

where α_s and α_a are the extinction parameter for scattering and absorption, respectively.

Integration of 2.15 leads to the Lambert-Beer's law:

$$\begin{aligned} I(\lambda) &= I_0(\lambda) \, \exp\left\{ -\left[\left(\sum_i \sigma_i(\lambda) n_i \right) + \sigma_M(\lambda) n_M + \sigma_R(\lambda) n_R \right] \times L \right\} \\ &= I_0(\lambda) \exp\{-\alpha_\lambda \, L\} \end{aligned} \tag{2.19}$$

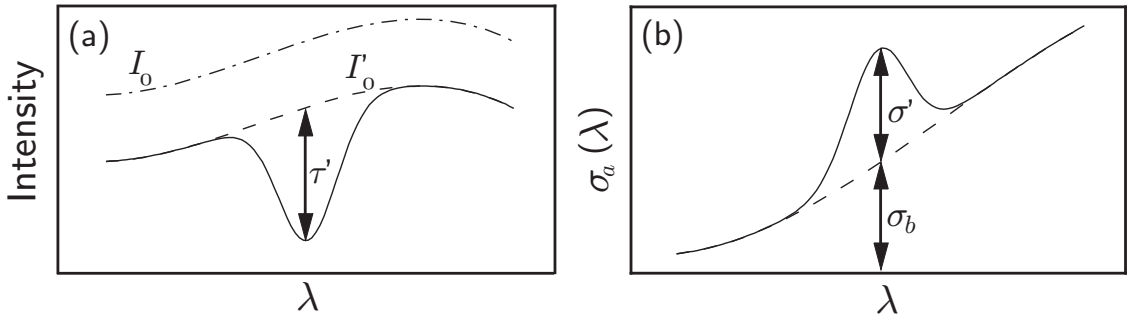

Figure 2.2: *The Principle of DOAS: The intensity I_0 and the absorption cross section σ can be separated by a filtering procedure into a broad and narrow band part.*

Unfortunately the incoming spectral solar irradiance $I_0(\lambda)$ outside the Earth's atmosphere is not known to a degree sufficient for spectroscopy. The problem of the badly known $I_0(\lambda)$ is avoided in introducing the Differential Optical Absorption Spectroscopy technique, DOAS (*Platt et al.* [1979], *Platt* [1994], *Stutz and Platt* [1996], *Platt and Stutz* [2004]). The technique allows to separate the absorption cross sections into the narrow band structures of absorption $\sigma'_i(\lambda)$ and the broad band spectral features $\sigma_b(\lambda)$. The narrow band part $\sigma'_i(\lambda)$ is then called the differential absorption cross section:

$$\sigma_a = \sigma_b + \sigma' \tag{2.20}$$

The separation into these two parts is possible due to the fact, that in general the scattering cross sections vary 'slowly' with the wavelength, while the (differential) absorption cross sections of molecules and atoms vary 'rapidly'. As mentioned in 2.2.2 for Mie scattering the wavelength dependency varies with $\lambda^{-1...3}$ depending on droplet size and size distribution, while for Rayleigh scattering the dependency goes with λ^{-4}. Applying this to the Lambert-Beers-law (equation 2.19) yields:

$$I_L(\lambda) = I'_0(\lambda)\exp\{-\alpha'(\lambda)L\} \qquad \text{with} \tag{2.21}$$

$$I'_0(\lambda) = I_0(\lambda)\exp\{-\alpha_b(\lambda)L\} \tag{2.22}$$

and $\alpha_b = \alpha_{a,b} + \alpha_s$. The differential optical depth only is then obtained from:

$$\tau'(\lambda) = -ln\frac{I_L(\lambda)}{I'_0(\lambda)} = \sum_i \sigma'_i(\lambda)n_iL \tag{2.23}$$

With the knowledge of the cross section σ_i the absorber concentration n_i can be determined from the optical depth. Even if n_i an σ_i change along the path L, a sensible mean can be derived from equation 2.23. High pass filtering to eliminate

broad band extinction structures are removed by division with a smooth function, e.g. a measured filter curve or polynomial of low order, see Figure 2.2.
For scattered light measurements the path L is also not known a priori. This means that for a given σ_i only the integral absorber concentrations along the path L can be measured. The integrated concentration is the so called slant column density SCD:

$$SCD = \int_0^L n_i(l)dl \tag{2.24}$$

The SCD is connected to the more significant vertical column density VCD via the so called air mass factor AMF = SCD / VCD. The air mass factor can be calculated with the solar zenith angle SZA (smaller than 70) as: AMF=1/cos(SZA).[2]

The possibility to measure many different species at the same time with high accuracy is the major ingredient and strength of the DOAS technique. It can be applied in many different observation geometries and platforms. The main distinction point of this technique is the used light source. The so-called active DOAS uses artificial light sources, while the so called passive DOAS uses natural light sources like the moon, stars or the sun.
The active DOAS setup consists of an artificial light source and retroreflectors. Accordingly it is possible to provide a long light path through the atmosphere (up to 20 km), which is important to detect weak and low trace gas concentrations in the troposphere. But it is also possible to use multi reflection systems to get long light paths under limited proportions like aerosol and smoke chambers (e.g. [*Volkamer* 2001], [*Trick* 2004]).
The passive DOAS technique relies on the sun as a natural light source. It is used in a wide range of different airborne and space platforms like planes, balloons or satellites. For example the satellite instruments like GOME or SCIAMACHY provide a detailed view of the global trace gas distributions in the troposphere and stratosphere (e.g. [*GOME* 1995], [*Burrows et al.* 1995], [*Beirle et al.* 2004], [*Frankenberg et al.* 2004]). Using an airborne multi axis DOAS system, it is possible to measure trace gas distributions under and above a plane simultaneously during a flight(e.g. [*Heue et al.* 2004]). Using high flying balloons detailed studies of the chemical composition of the upper troposphere and stratosphere are possible(e.g. [*Bösch et al.* 2003]). With the ground base passive DOAS system, some fundamental detection of trace gas source were made in the past (e.g. [*Wagner and Platt* 1998], [*Bobrowski et al.* 2003]).
The previously described active and passive DOAS methods are mostly used to determine unknown trace gas concentrations at known light paths. This study

[2]The AMF is a geometrical factor for direct light measurements. For scattered light measurements a radiative transfer model calculation is necessary to determine the air mass factor.

reverse this approach. It makes use of the known concentration of atmospheric constituents. In this study molecular oxygen (O_2) is used. A detailed description of the spectroscopic basics of the oxygen A-band is given in the next section.

2.4 Basics of the Oxygen A-Band Spectroscopy

The oxygen molecule O_2 is a diatomic molecule. Nearly all the oxygen is one particular isotope. ^{16}O makes up 99.76 % of all the oxygen on the Earth. The other two stable isotopes, ^{17}O and ^{18}O, are found only in trace amounts, 0.04 % and 0.20%, respectively. Here the basic optical properties of the oxygen molecule will be discussed to understand the structure and properties of the absorption lines and the resulting absorption bands. A detailed overview is given for example in [*Haken and Wolf* 1994] or [*Herzberg* 1950].

2.4.1 Absorption Spectrum

The spectrum of molecular oxygen O_2 in the visible and near-infrared region consists of three atmospheric bands (A-, B- and γ-Band). They belong to different rotation-vibration spectra of several electronic transitions. The A-, B-, and γ-bands, which are, respectively, the 0-0, 1-0, and 2-0 bands of the $b^1\Sigma_g^+$ - $X^3\Sigma_g^-$ atmospheric band system - and the 0-0 band of the infrared atmospheric system, at 1.27 μm. An overview of the different oxygen absorption bands is given in Table 2.1. The oxygen A-band is very suitable for atmospheric measurements. This is due to the fact, that oxygen is the only absorber in this wavelength region, while for the B- and γ- band water vapor absorption lines overlap a wide range of the oxygen absorption lines. For this reason, the oxygen A-band is of great interest for atmospheric remote sensing measurements from ground or from space borne platforms ([*Heidinger and Stephens* 1998], [*Stephens and Heidinger* 2000], [*Heidinger and Stephens* 2000]. In the early 60th *Yamamoto and Wark* [1961] proposed that oxygen A-band absorption observed in measured reflection spectra from space cloud be used to infer column oxygen amounts and hence provide a way to estimate cloud top pressure. Since then oxygen A-band measurements become a powerful technique of remote sensing of cloud top height from space (e.g., [*Guzzi et al.* 1994], [*Burrows et al.* 1999], [*Kokhanovsky and Rozanov* 2004], [*Rozanov et al.* 2004]).

For these reasons, precise spectroscopic parameters of 0_2 are necessary and were subsequently performed in the laboratory (for example: *Ritter and Wilkerson* [1987], *Gamache et al.* [1998]).

Table 2.1: *The atmospheric absorption bands of oxygen in the VIS and NIR spectral region. The spectroscopic data is taken from the HITRAN96 database, [Gamache et al. 1998].*

Electronic transition	Vibrational transition	Band center [nm]	Band strength [cm/molec]	Name
$B^3\Sigma_g^- \leftarrow X^3\Sigma_g^-$	-	UV 175.9	-	Schumann-Runge
$A^3\Sigma_g^+ \leftarrow X^3\Sigma_g^-$	-	UV 242-286	-	Herzberg I
$b^1\Sigma_g^+ \leftarrow X^3\Sigma_g^-$	$(2 \leftarrow 0)$	628.85	4.63E-25	$\gamma - band$
$b^1\Sigma_g^+ \leftarrow X^3\Sigma_g^-$	$(1 \leftarrow 0)$	688.47	1.49E-23	$B - band$
$b^1\Sigma_g^+ \leftarrow X^3\Sigma_g^-$	$(0 \leftarrow 0)$	762.19	2.24E-22	$A - band$
$b^1\Sigma_g^+ \leftarrow X^3\Sigma_g^-$	$(1 \leftarrow 1)$	771.07	9.53E-26	
$b^1\Sigma_g^+ \leftarrow X^3\Sigma_g^-$	$(0 \leftarrow 1)$	864.75	7.88E-27	
$a^1\Delta_g \leftarrow X^3\Sigma_g^-$	$(1 \leftarrow 0)$	1067.7	9.53E-27	
$a^1\Delta_g \leftarrow X^3\Sigma_g^-$	$(0 \leftarrow 0)$	1268.6	3.68E-24	
$a^1\Delta_g \leftarrow X^3\Sigma_g^-$	$(0 \leftarrow 1)$	1580.8	2.75E-28	

Vibration-Rotation Spectra

The total excitation energy E of a molecule is the sum of the rotational, vibrational and electronic excitations:

$$E = E_{el} + E_{vib} + E_{rot} \tag{2.25}$$

From this equation it follows that it is possible to distinguish between three different kinds of optical spectra. They will be briefly discussed:

- Rotational spectra are transitions between the different rotational levels for a given vibrational level and a fixed electronic state. Only the *rotational quantum number N* changes. The spectra are in the microwave and the far-infrared region, respectively. They can be observed by using the Raman-spectroscopy technique.

- Rotational-vibrational spectra are transitions between the rotational level of a certain vibrational level and the rotational level of another vibrational level

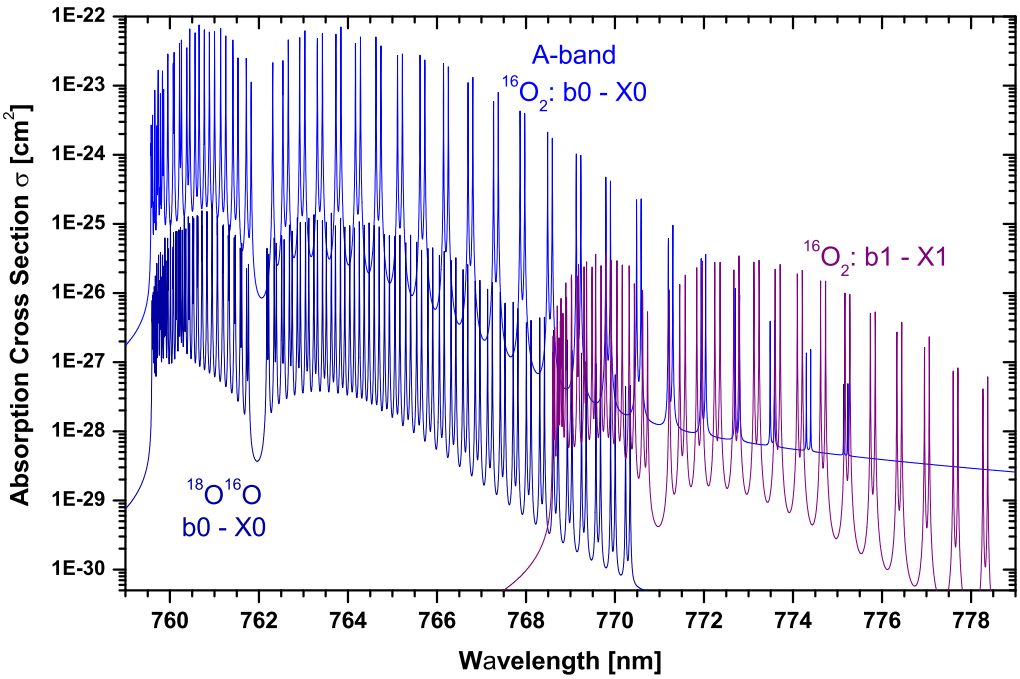

Figure 2.3: *Overview of the cross section spectrum of the oxygen A-band, adapted from [Funk 2000].*

with the same electronic state. The electronic quantum number is not changing, while the rotational quantum number J and the vibrational quantum number v are changing. The spectra are located in the near- infrared region. Rotational-vibrational spectra consist of groups of spectral lines, so called bands.

- Electronic spectra are transitions between the rotational level of the different vibrational levels of a given electronic state and the rotational- and vibrational level of a different electronic state. The spectra are in the UV, the visible and the near-infrared. The band systems of all allowed electronic transitions of a molecule are the band system of this molecule.

The spectral lines in molecular spectra can hence be described as:

$$\Delta E = (E'_{el} - E''_{el} + (E'_{vib} - E''_{vib}) + (E'_{rot} - E''_{rot}) = \Delta E_{el} + \Delta E_{vib} + \Delta E_{rot} \quad (2.26)$$

Here $(')$ means the initial state and $('')$ is the final state. Normally

$\Delta E_{el} \gg \Delta E_{vib} \gg \Delta E_{rot}$.

For rotational-vibrational spectra it is $\Delta E_{el} = 0$, so only the rotational and vibrational part of equation 2.26 applies.

$$\Delta E = E'_{el} + (E'_{vib} - E''_{vib}) + (E'_{rot} - E''_{rot}) \tag{2.27}$$

For the calculation of the rotational energy of a diatomic molecule, it is assumed that the molecule is a stiff rotator with the rotational axis being perpendicular to the molecule axis. For this configuration the energy eigenvalue can be calculated as:

$$E_{rot} = B\ N(N+1). \tag{2.28}$$

The rotational frequency B is characteristic for each molecule species and can be obtained from the spectra. *Ritter and Wilkerson* [1987] found $B = 1.437678$ cm^{-1} for $^{16}O_2$.

For the vibrational energy levels the quantum mechanical calculations yield:

$$E_{vib} = \nu_0(\nu + \frac{1}{2}) \quad \text{with} \quad \nu = 0, 1, 2, \ldots \tag{2.29}$$

where ν is the *vibrational quantum number*. For oxygen the vibrational frequency is $\nu_0 = 1556.3$ cm^{-1} for the $(1 \leftarrow 0)$ transition.

It is possible to observe three different branches in a rotational-vibrational spectrum :

P-branch: ΔN = −1 The rotational excitation decreases. The energy of the transition is smaller than for the band center i.e., the wavelength is longer.

Q-branch: ΔN = 0 The rotational excitation remains constant. For the A-band this branch is forbidden applying to the selection rules.

R-branch: ΔN = +1 The rotational excitation increases. The energy of the transition is larger than for the band center, the wavelength is shorter.

Electronic Configuration

Only the axial component of the orbital angular momentum for the electrons about the internuclear axis is a constant of motion. The axial components of the different electrons adds up algebraically: $\Lambda = |\sum_i \lambda_i|$. The quantum number Λ can take the values $\Lambda = 0, 1, 2, \ldots$. The corresponding molecular state is designated a

$\Sigma, \Pi, \Delta, \Phi, ...$ state. $\Pi, \Delta, \Phi, ...$ states are doubly degenerate (Λ can have two values, $-\sum_i \lambda_i, +\sum_i \lambda_i$), while Σ states are non-degenerate.
The spin of the individual electrons add up vectorially to $\vec{S}$ with the quantum number $S = \sum_i m_{S_i}$, where m_{S_i} is the spin quantum number of the different electrons. In Σ states the resulting spin S is fixed in space as long as the molecule does not rotate and if there is no external magnetic field. If $\Lambda > 0$, there is an internal magnetic field in the direction of the internuclear axis. This magnetic field causes a precession of S about the field direction. The referring quantum number is denoted with Σ (not to be mixed up with the $\Lambda = 0$ state) and quantum theory allows values for $\Sigma = S, S-1, S-2, ..., -S$. That is to say, 2S+1 different values are possible. For the oxygen molecule with two unpaired electrons S can be S = 1 and S = 0, hence the multiplicity is 3 and 1, resulting in a triplet or singlet state. This is indicated in the term symbol (e.g. $^3\Sigma$).
In the ground state, the oxygen molecule has two unpaired electrons in the $2p\pi_g^*$ orbital with antiparallel orbital angular momentum ($\Lambda = 0$) and parallel spin (S =1). This results in a $^3\Sigma_g^-$ configuration.
The total electronic angular momentum is obtained by adding Λ and Σ. Thus for the quantum number of the resultant electronic angular momentum about the internuclear axis we have $\Omega =\mid \Lambda + \Sigma \mid$. For singlet terms (S=0) we have $\Omega = \Lambda$, for triplet states (S=1) we have $\Omega = \Lambda - 1, \Lambda, \Lambda + 1$. All angular momenta are summarized in the total angular momentum J.
For the coupling of the different momenta, two types must be distinguished. For $\Lambda \neq 0$, $\overrightarrow{\Omega}$ is perpendicular to the rotational momentum $\overrightarrow{R}$. The total angular momentum is calculated from J = Ω + N. This case is called Hund's case (a). In Hund's case (b) for $\Lambda = 0$ (Σ state), the spin is not coupled to the internuclear axis. For this, electronic angular momentum Ω is not defined. The total angular momentum J is given by:

$$J = (N + S), (N + S - 1), ..., |N - S| \tag{2.30}$$

Symmetry properties

For the classification of molecular electronic states, the symmetry properties of the electronic eigenfunctions are of great importance. According to the previous examination the eigenfunction has an electronic, vibrational and rotational part $\Psi = \Psi_{el} + \Psi_{vib} + \Psi_{rot}$. Each part has to be examined for effects on symmetry operations. In a diatomic molecule any plane through the internuclear axis is a plane of symmetry due to the axial symmetry.
The sign of the electronic eigenfunction $\Psi_e l$ of a non-degenerate state (Σ state) ei-

ther remains unchanged (the state is called Σ^+) or changes, when reflected at any plane passing through both nuclei (the so called Σ^- state).
If the two nuclei in the molecule have the same charge, the field in which the electrons move has, in addition to the symmetry axis, a center of symmetry - the midpoint of the internuclear axis. In consequence of this symmetry the electronic eigenfunction $\Psi_e l$ remains either unchanged or only change sign when reflected at the center. In the first case the state to which the eigenfunction belongs is called an even state, the second case an odd state. The symmetry property even or odd is indicated by adding a subscript g or u, respectively, to the term symbol. The electron spin has no influence on the symmetry property even-odd and therefore the components of a given multiplet term are either all even (g) or all odd (u).
If the total eigenfunction changes sign in the case of reflection at the origin, the rotational level is called positive. In the opposite case (no changing sign) the rotational level is called negative[3].
For the $^{16}O_2$ molecule with two identical nuclei, only even N are allowed for Σ^+ states and odd N for Σ^- states. This is to the fact, that the total eigenfunction must be symmetric in the exchanging the labels of the nuclei. For $^{18}O^{16}O$ this restriction is not valid due to different nuclei. This means, that odd as well as even rotational levels are allowed. As it can seen in figure 2.3, this spectrum shows twice as many lines as the $^{16}O_2$ spectrum.

Selection Rules

The transition between states with different multiplicity are not allowed for electronic dipole radiation (E1). Due to that rule, the $^1\Sigma_g^+ \longleftarrow 3\Sigma_g^-$ transitions are spin- forbidden. This means, that the transitions have to be electronic quadrupole transitions (E2), which is according to *Herzberg* [1950] the case, or magnetic dipole transitions (M1):

$$\Delta J = 0, \pm 1 \qquad \text{with} \qquad J = 0 \not\longrightarrow J = 0 \qquad \text{(E1),(M1, E2)} \tag{2.31}$$

$$\Delta\Lambda = 0 \qquad \text{(E1)}, \qquad \Delta\Lambda = \pm 1 \qquad \text{(M1, E2)} \tag{2.32}$$

$\Delta\Lambda = 0$ is only allowed for inter-system transitions in the case of changing magnetic dipole moment.
For the symmetry of the rotational levels, the selection rule is:

$$+ \longleftrightarrow + \qquad - \longleftrightarrow - \qquad - \not\longleftrightarrow + \qquad \text{(M1,E2)} \tag{2.33}$$

[3]For $\Sigma-$ states the odd-numbered rotational levels are positive and the even are negative. For $\Sigma+$ it is the opposite way.

This rule is the cause for the missing Q-branch of the $\Sigma^+ \longleftarrow \Sigma^-$. For the parity following selection rule is valid for the magnetic dipole or electronic quadrupole transition:

$$g \longleftrightarrow g \qquad u \longleftrightarrow u \qquad g \not\longleftrightarrow u \qquad \text{(M1,E2)} \tag{2.34}$$

The Oxygen A-band

The total angular moment J and the rotational angular moment N describe the rotational level of oxygen. The transitions are characterized by the change of these two numbers ΔN and ΔJ. For a change of -1,0 or +1 the capital letters P, Q and R are used followed by the initial values of N and J.

Figure 2.3 shows the cross section spectra for the oxygen A-band. In the spectral region of the A-band three different band systems overlap:

- $^{16}O_2$: $b^1\Sigma_g^+ \leftarrow X^3\Sigma_g^-$ $(0 \leftarrow 0)$
- $^{16}O_2$: $b^1\Sigma_g^+ \leftarrow X^3\Sigma_g^-$ $(1 \leftarrow 1)$
- $^{18}O^{16}O$: $b^1\Sigma_g^+ \leftarrow X^3\Sigma_g^-$ $(0 \leftarrow 0)$

Since the Q branch is forbidden, the band systems consists of the P and R branches. The P-branch starts at 13120 cm^{-1} (762.3 nm) and extends upwards in wavelength. The PP and PQ lines are separated by approximately 2 cm^{-1} (0.12 nm). The line pairs have a distance of 6 $cm^{-1} \hat{=}$ 0.34 nm ($J'' = 1$) increasing up to 10 $cm^{-1} \hat{=}$ 0.57 nm ($J'' = 20$). The R-branch, formed by the RR and RQ transitions, is in the range 13125 - 13170 cm^{-1} (759.3 - 761.9 nm). The separation between pairs in this branch is about 4.5 cm^-1 for J''=1, decreasing to less than 2 cm^{-1} for J'' = 13. These pairs form a band head at about 13165 cm^{-1} or 759.59 nm, while the band center lies near 762 nm.

Chapter 3

Concepts

3.1 Concepts of Cloudy Skies Radiative Transfer

In this section a special theory of photon transport in cloudy sky is presented, namely the concept of photon diffusion. Specially the relation between the measured photon path length and other cloud properties like liquid water path, cloud optical thickness and cloud geometrical thickness is elaborated.

3.1.1 Cloud optical depth

The cloud optical depth is defined by:

$$\tau = \int_{z_1}^{z_2} \sigma(\lambda, T(z), p(z))\ n(z)\ dz \tag{3.1}$$

where σ denotes the extinction cross section of an individual particle and n(z) the number density of particles. T(z) is the temperature at given height z and p(z) the related air pressure. Under the assumption, that absorption can be neglected (inside the cloud), extinction would be primarily due to scattering. The scattering extinction is given by α_s. The cloud optical depth τ_c can be calculated by integration over a vertical path from the cloud base z_1 to the cloud top z_2. This is just the geometrical vertical extension of the cloud ΔH.
The average distance a photon travels before it is scattered is called the mean free path. On average, the photon will be scattered by the time it traverses a distance of just one mean free path. This mean free path can be interpreted as the inverse scattering extinction.
This leads to the following definition of the cloud optical depth:

$$\tau_c = \frac{\Delta H}{\lambda_{Mie}} \tag{3.2}$$

Here λ_{Mie} is the Mie scattering mean free path, defined by:

$$\lambda_{\text{Mie}} = \frac{1}{2\pi\overline{r^2} \cdot N} \tag{3.3}$$

Mie scattering can occur on cloud droplets and possibly on aerosols, even if Rayleigh scattering can be neglect at 770 nm.

3.1.2 Transport Mean-Free Path

Davis and Marshak [1997] introduced a transport mean free path $\lambda_{tr} = \lambda_{Mie}/(1-g)$ to treat the problem, that the Mie scattering phase function is not isotropic (see section 2.2.2, as isotropic scattering problem. Therefore the direction before and after the scattering are correlated. Actually it takes on the average 6 to 7 scattering events inside a liquid water cloud before the incoming light has forgotten its initial direction of incidence. Using this transport mean free path, the optical depth (equation 3.2) can be extend to a new rescaled cloud optical depth:

$$\tau_c^* = (1-g) \cdot \frac{\Delta H}{\lambda_{Mie}} = (1-g) \cdot \tau_c \tag{3.4}$$

The rescaled cloud optical depth accounts for the fact, that the Mie scattering favors forward scattering. The asymmetry factor g is chosen as g = 0.85, since the study mainly addresses the radiative transfer in liquid water clouds. The mean free path inside a cloud is of order of 10 m, while it is remarkable larger outside the cloud.

3.1.3 Liquid Water Path

Later the cloud optical depth is inferred from ground based microwave radiometer liquid water path measurements. Therefore some well-known relations are recalled. The effective cloud droplet radius r_e is defined by:

$$r_{\text{e}} = \frac{\int_0^\infty n(r) \cdot r^3 \cdot \mathrm{d}r}{\int_0^\infty n(r) \cdot r^2 \cdot \mathrm{d}r} = \frac{\int_0^\infty r^3 \cdot \mathrm{d}N(r)}{\int_0^\infty r^2 \cdot \mathrm{d}N(r)} = \frac{\overline{r^3}}{\overline{r^2}} \tag{3.5}$$

The liquid water content (LWC)[1] is given by:

$$LWC = \frac{4\pi}{3}\overline{r^3} \cdot \rho_{\text{w}} \cdot N \tag{3.6}$$

with ρ_{w} being the liquid water density.

[1]The LWC is the amount of liquid water per unit volume of air and usually expressed either in g/kg or g/m^3. On the average, for a typical cloud it varies from 0.05 to 3 g/m^3.

the effective radius can be written as:

$$r_{\mathrm{e}} = \frac{3 \cdot \mathrm{LWC} \cdot \lambda_{\mathrm{Mie}}}{2 \cdot \rho_{\mathrm{w}}} \tag{3.7}$$

From equation 3.7 follows:

$$\lambda_{\mathrm{Mie}} = \frac{2 \cdot r_{\mathrm{e}} \cdot \rho_{\mathrm{w}}}{3 \cdot \mathrm{LWC}} \tag{3.8}$$

The column integrated liquid water path is given by:

$$LWP = \int_{z_1}^{z_2} \mathrm{LWC}(z) \cdot dz = \overline{\mathrm{LWC}} \cdot (z_2 - z_1) = \overline{\mathrm{LWC}} \cdot \Delta H \tag{3.9}$$

Using this relation from equations 3.4 and 3.8, the relation between the effective cloud optical depth τ_c^* and the measured quantity LWP can be obtained:

$$\tau_{\mathrm{c}}^* = (1 - g) \cdot \tau = (1 - g) \cdot \frac{3 \cdot \mathrm{LWP}}{2 \cdot r_{\mathrm{e}} \cdot \rho_{\mathrm{w}}} \tag{3.10}$$

3.1.4 Classical Diffusion Theory

The path of photons through the atmosphere can be described as a long random walk. Random walk through a thick media ($\tau_c^* \geq 1$) can be described as (classical) diffusion process. This is possible, as the photon's random motion due to anisotropic Mie-scattering can be described as isotropic diffusion process by introducing the transport mean free path λ_{tr}. As a consequence the variability induced changes in the domain-average radiative fluxes are effectively smeared-out by anisotropic Mie scattering. This radiative smoothing refers to the fact that the radiance field reflected or transmitted through optically thick clouds is, below a certain spatial scale (the radiative smoothing scale η) smoother than the liquid water content or cloud droplet density fields. *Cahalan and Snider* [1989] as well as *Marshak et al.* [1995] and *Davis and Marshak* [1997] found a scale break due to radiative smoothing in reflected radiances observed by LANDSAT imagery at roughly 200m to 400m. Further investigations yield the radiative smoothing scale in reflection to be $\eta_R \propto \frac{\Delta H}{\sqrt{\tau_c^*}}$. For skylight transmitted through through optically thick cloud to the ground, [*Savigny et al.* 1999] showed, that in agreement with the diffusion theory prediction, the smoothing scale in transmition is related to the vertical extension of the cloud $\eta_T \propto \Delta H$. Radiative smoothing occurs because inhomogeneities in cloud structure are smoothed out by photon diffusion.

Davis and Marshak [2002] investigate the radiative transfer for transmitted light through dense plane-parallel clouds using photon diffusion theory, limited to nonabsorbing wavelengths. For this the linear transport equation to determine the time-dependent radiance field $I(t, \mathbf{r}, \mathbf{\Omega})$ is used:

$$\left(c^{-1}\frac{\partial}{\partial t}\right) = -\sigma(\mathbf{r})I(t, \mathbf{r}, \mathbf{\Omega}) + \sigma_s(\mathbf{r})\int_{4\pi} p(\mathbf{\Omega}' \cdot \mathbf{\Omega})I(t, \mathbf{r}, \mathbf{\Omega}')d\Omega' \tag{3.11}$$

Here the vector $\mathbf{r}$ denotes the position inside the cloud and $\mathbf{\Omega}'$ the propagation direction. $\sigma(\mathbf{r})$ is the extinction coefficient, while $\sigma_s(\mathbf{r})$ is the scattering extinction coefficient. $\mathbf{\Omega}' \cdot \mathbf{\Omega} = cos\Theta = \mu$ is the cosine of the scattering angle and $p(\mathbf{\Omega}' \cdot \mathbf{\Omega})$ is the corresponding phase function.
Taking a delta pulsed light source and assuming of to be isotropic, is placed on one side of the slap (cloud top). The detector is situated on the other side (cloud base). The transmitted flux field at the cloud base is described by:

$$G_T(t, x, y) = \int_{\mu \leq 0} |\mu| \left[\int_{2\pi} I[t, x, y, 0, \mathbf{\Omega}(\mu, \phi)]d\phi\right] d\mu \tag{3.12}$$

Interpreting the radiance field I as probability to find a photon out with space $\mathbf{r}$ and angle Ω at time t, equation 3.12 describes the probability and space-time variables for photons in transmission. This leads to:

$$T = 2\pi \int\int G_T(\lambda\rho)\rho \, d\rho \, d\lambda \qquad \text{for transmission} \tag{3.13}$$

$$\langle\lambda\rangle_T = 2\pi \int\int \lambda \, dP_T(\lambda, \rho) \qquad \text{for the mean path length} \tag{3.14}$$

Here λ denotes the path lengths and $\rho = (x^2 + y^2)^{0.5}$ the horizontal photon displacement relative to the position of the light source.
Polonski and Davis [2004] investigate the spatial Green's function G_T on the diffusion approximation. If the single scattering albedo $\omega_0 = 1$, the transmission T will depend only on τ_c^* and χ. It can been shown that:

$$T = \frac{1}{1 + \tau_c^*/2\chi} \tag{3.15}$$

In the steady state (no absorption inside the slap) the radiant energy is conserved, which means R+T=1. For the reflectance R following expression can now be found:

$$R = \frac{\tau_c^*/2\chi}{1 + \tau_c^*/2\chi} \tag{3.16}$$

If the ratio R/T denoted with ϵ it follows that :

$$\epsilon = \frac{T}{R} = \frac{2\chi}{\tau_c^*} = \frac{2\chi}{(1-g)\cdot\tau_c} \tag{3.17}$$

This ration becomes a small quantity as the rescaled optical depth τ_c^* becomes large. The value of χ is taken to be 0.7014, the proper answer to the (half space) Milne problem [*Case and Zweifel* 1967].

For the first moment $\langle L_c \rangle$ the following relation is found:

$$\langle L_c \rangle / \Delta H = \frac{1}{2} \cdot [(1-g)\cdot\tau_c] \cdot [1 + C_1(\epsilon)] \tag{3.18}$$

$$C_1(\epsilon) = \frac{\epsilon}{2} \cdot \frac{4+3\epsilon}{1+\epsilon} \tag{3.19}$$

Finally for the second moment $\langle L_c^2 \rangle$ the following relation is obtained:

$$\langle L_c^2 \rangle / \Delta H^2 = \frac{7}{20} \cdot [(1-g)\cdot\tau_c]^2 \cdot [1 + C_2(\epsilon)] \tag{3.20}$$

$$C_2(\epsilon) = \frac{\epsilon}{14} \cdot \frac{56 + \epsilon(166 + 15\epsilon(10+3\epsilon))}{(1+\epsilon)^2} \tag{3.21}$$

As explained earlier in this section, ϵ becomes a small quantity as the rescaled optical depth τ_c^* becomes large. This means that the correction terms $C_1(\epsilon)$ and $C_2(\epsilon)$, which only depend on ϵ, are not negligible for only small values of $\tau_c^* < 10$.

The ratio $\langle L_c^2 \rangle^{1/2} / \langle L_c \rangle$ converges to $\sqrt{7/5} \approx 1.18$ for $\tau_c^* \gg 1$. Although diffusion is not expected to be a valid transport theory when $\tau_c^* \ll 1$, that limit leads to $\langle L_c^2 \rangle^{1/2} / \langle L_c \rangle \approx \sqrt{2}$. In chapter 5 it is shown, that the ratio of the measured first and second moment of the path length distribution behave like the theoretical prediction.

3.1.5 Anomalous Diffusion

The previous examination of the classical diffusion does neither account for cloud inhomogeneities nor the patchiness of the cloud deck. The inhomogeneous variation of the extinction is linked to the distribution of the liquid water content inside the cloud. Local mean free pathes of the order of the extend of clouds or even of the distance between clouds or clouds and surface can occur. In all cases, an increase of longer step sizes between Mie scattering is obvious. *Davis and Marshak* [1997] suggested that truncated Lévy walks would give a better representation of the photon transport inside the clouds. The Lévy walk model predicts for the mean photon path [*Davis and Marshak* 1997] [*Buldyrev et al.* 2001]:

$$\langle L_c \rangle \approx \Delta H \cdot (\tau_c^*)^{\alpha-1} \tag{3.22}$$

The Lévy index α varies between 1 and 2. A Lévy index $\alpha = 2$ leads to a Gaussian distribution, while α =1 leads to a Cauchy distribution, respectively. Here the decay of the probability for longer step sizes between individual Mie scattering events is described by by a power law with exponent $-(\alpha + 1)$. The upper limit $\alpha = 2$ reverts to the classical diffusion, described in equation 3.18. Unfortunately the second and higher moments of the photon path length distribution have not yet been investigated theoretically for Lévy transport, neither for the scaling exponent nor for the prefactors nor the pre-asymptotic correction terms $C_1(\epsilon)$ and $C_2(\epsilon)$. To examine the scaling behavior of the first and second moment of the path length distribution equation 3.18 and equation 3.20 have to generalized. For this purpose, the right hand sides of these equations are simply taken to the power $(\alpha - 1)$. In chapter 5 the theoretical values for different Lévy indices were plotted into the $\langle L_c \rangle(\tau_c^*)$-plots.
For Lévy indices $\alpha < 2$ the mean total photon path length is reduced. This is a consequence of the increased mean free path for inhomogeneous clouds. It can be explained by the fact, that the propagation of light is enhanced in regions with lower local extinction than the average. This enhancement results in a photon transmission through a dense medium on a less diffusive, and therefore shorter path. This leads to an increased probability for larger steps in the Lévy model. Therefore the shape of the distribution (in comparison to a classical diffusion case) has an impact on the absorption. Further *Funk* [2000] has shown, that for regions with weak and moderate absorption the shape of the distribution has no impact on the amount of absorption for weak and moderate absorption.

3.2 Photon Path Length Distributions

The geometrical path length L is the length of the path of a particle from the top of atmosphere to the ground including all scattering processes. From this point of view extinction is solely gaseous absorption. The dimensionless optical path is the geometrical path length l multiplied with the scattering coefficient α_s: $\lambda_{op} = \alpha_s L$.

3.2.1 Lambert Beers Law

The attenuation of light along a path of length L is given by Beers law:

$$I_L(\lambda) = I_0(\lambda) \exp\{-\alpha_a L\} \tag{3.23}$$

The exponential factor is called transmission T. In a isotropic atmosphere it is given along a path of length L:

$$T(L) = \exp\left\{-\int_0^L \sigma n dl\right\} \approx \exp\{-\sigma n L\} = \exp\{-\alpha L\}\,. \tag{3.24}$$

Photons will not travel the same path length L through the atmosphere. The probability density function (PDF) of the geometrical path lengths p(l) is given by:

$$p(l)dl = P(l - 1/2\ dl < L < l + 1/2\ dl) \tag{3.25}$$

This equation describes the probability, that a photon travels a path length l without absorption. The total transmission is now given by the integral over all path lengths described by the PDF multiplied with the Beer factor:

$$T(\alpha) = \int_0^\infty p(l)\exp(-\alpha l)dl \tag{3.26}$$

This equation is formally equivalent to the Laplace transformation $\mathcal{L}$ of p(l) with respect to α:

$$\tilde{p}(\alpha) = \mathcal{L}_{\alpha\leftarrow l}p(l) = \int_0^\infty p(l)\exp(-\alpha l)dl = T(\alpha) \tag{3.27}$$

In general the function $\tilde{p}(\alpha)$ as well as the path length l have to be complex to do the transformation. In consequence, since no information is provided by the measurement process on the complex part of the Laplace transformation the inverse transformation results in a mathematically ill-posed problem .

For a non isotropic atmosphere the situation is more complicated. It has to be considered, that the extinction is different for each photon. For example, a photon path leading more through the lower part of a cloud picks up more gas column than another one, leading through the higher part of the cloud.

$$T_i(L_i) = \exp\left\{-\int_0^{L_i} \sigma_i(l)n_i(l)dl\right\} \tag{3.28}$$

It has also to be considered, that σ_i changes along the path because of the temperature dependency of the line strength. For N photons the total transmission $\overline{T}$ is given by the average:

$$\overline{T} = \frac{I}{I_0} = \frac{\sum_{i=0}^N I_{0,i}\cdot T_i(L_i)}{\sum_{i=0}^N I_{0,i}} = \frac{1}{N}\sum_{i=0}^N\left(-\int_0^{L_i}\sigma_i(l)n_i(l)dl\right) \tag{3.29}$$

The right hand side requires for each photon path the knowledge of the exact trajectory. This is for large photon numbers highly impractical. Furthermore since α depends on the path l, $\overline{T}$ is not an explicit function of α.

This problem can only be solved by introduction of the probability density function p(l) using a mean absorption coefficient $\overline{\alpha}$:

$$\overline{T(\alpha_i, L_i)} \approx T(\overline{\alpha}) = \int_o^\infty p(l) \exp\{-\overline{\alpha} \cdot l\}\, dl \tag{3.30}$$

Here the mean absorption coefficient $\overline{\alpha}$ for all paths is given by:

$$\overline{\alpha} = \frac{1}{N} \sum_{i=0}^{N} \frac{1}{L_i} \int_0^{L_i} \sigma_i(l) n_i(l) dl \tag{3.31}$$

Equation 3.30 is only true in a strict sense for constant σ_i and n_i for each path L_i. It is now possible to use the relation $\overline{\alpha} \cdot l = \alpha_i \cdot L_i$ to rewrite equation 3.29:

$$\overline{T(\alpha_i, L_i)} = \frac{1}{N} \sum_{i=0} N \exp\{-\alpha_i \cdot L_i\} \tag{3.32}$$

In Monte Carlo simulations *Funk* [2000] has shown that the approximation $\overline{T(\alpha_i, L_i)} \approx T(\overline{\alpha})$ is valid in general. For this purpose, Monte Carlo simulations of the path of a photon ensemble were performed and $\overline{T(\alpha_i, L_i)}$ as well as $T(\overline{\alpha})$ calculated and compared.

3.3 Measuring Photon Path Length Distributions

As previously mentioned, the transmission T(α) is formally equivalent to the Laplace transformation of p(l). In consequence a possible method to obtain the path length distribution could came to inverse the Laplace transformation of the measured transmission. This straight forward method is not valid as it requires integration in the complex plane along a parallel to the imaginary axis. Unfortunately $\tilde{p}$ is only known on the positive half of the real axis. The inverse Laplace transformation for complex α and l is given by the Bromwich integral, see [*Boas* 1983]:

$$p(l) = \frac{1}{2\pi i} \int_{c-i\infty}^{c-i\infty} \tilde{p}(\alpha) e^{\alpha l} d\alpha \tag{3.33}$$

Another direct method is the calculation of p(l) as the inverse Fourier transformation of the characteristic function $\mathcal{X}$ of p(l). This function is described by all moments m_j of the searched quantity p(l):

$$\mathcal{X}^{(k)} = \sum_j \frac{(-ik)^j}{j!} m_j \qquad \text{where} \qquad m_j = \int_0^\infty \tilde{p}(\alpha) l^j dl \tag{3.34}$$

Applying the inverse Fourier transformation gives p(l):

$$p(l) = \frac{1}{2\pi} \int_0^\infty \mathcal{X}^{(k)} e^{ikl} dk \tag{3.35}$$

The moments m_j can be found by expanding the exponential function. This exponential function converges very slowly. Also a discrete inverse Fourier transformation is not suitable, because for only 5 points already 100 moments are required.

For the evaluation of the measured spectra an indirect approach is used. Accordingly assumptions about the analytical form of the photon path length distribution is made. In this study in most cases the Gamma distribution is used to describe the PDF:

$$p(l) = \frac{1}{\Gamma(\kappa)\left(\frac{\langle l \rangle}{\kappa}\right)^\kappa} (l)^{\kappa-1} e^{-\frac{\kappa l}{\langle l \rangle}} \qquad \text{with} \qquad \kappa = \frac{\langle l \rangle^2}{var(l)} \tag{3.36}$$

The photon path length distribution can be approximated for homogeneous finite slabs [*Hulst* 1957] as well as for inhomogeneous or fractal cloud layers [*Marshak et al.* 1995] by Gamma distributions. For the Gamma distribution the Laplace transform is well known and given by:

$$\tilde{p}(k) = \frac{1}{\left(1 + \frac{\langle x \rangle}{\kappa} k\right)^\kappa} \tag{3.37}$$

Accordingly, for the spectra evaluation the measured transmissions are fitted to the Laplace transform of the distribution. The photon path length L_{tot} is expressed in units of Vertically-integrated Oxygen Density or VOD.

3.4 Spectral Line Properties

3.4.1 Line Strength

The line strength S_i is determined by the occupation of the initial state, which dependents on temperature. This dependence of the line strength, which is related to the cross section σ by:

$$S_i = \int_0^\infty \sigma_i(\lambda) d\lambda \tag{3.38}$$

can be calculated with following relation:

$$\frac{S_{J''}(T_1)}{S_{J''}(T_0)} = (T_0)\frac{T_1}{T_0} exp\left\{\frac{-hcE_{J''}}{k}\left(\frac{1}{T_1} - \frac{1}{T_0}\right)\right\} \frac{1 - exp\{-hcE_{J''}/kT_1\}}{1 - exp\{-hcE_{J''}/kT_0\}} \tag{3.39}$$

Here T_1 is the atmospheric temperature, while T_0 is a reference temperature (296 K for HITRAN data). h denotes the Planck's constant, c the speed of light and k the gas constant. $E_{J''}$ is the energy of the initial state. At low temperatures highly excited states are less frequently occupied, while low excited states are occupied more frequently. For example the PP 5,5 transition has an initial state energy of 44.2 cm^{-1}. For a temperature of $T_1 = 280K$ the temperature correction coefficient of the line strength $S_{J''}(T_1)/S_{J''}(T_0)$ is 1.05, while for $T_2 = 260K$ the correction coefficient is $S_{J''}(T_2)/S_{J''}(T_0) = 1.10$. However, the temperature correction coefficient for the PP 31,31 transition is determined to be $S_{J''}(T_1)/S_{J''}(T_0) = 0.80$ and $S_{J''}(T_2)/S_{J''}(T_0) = 0.43$, respectively.
In Table A.2 in the appendix the used spectroscopic data are listed. These data are based on the 2000 edition of the HITRAN database *Rothman et al.* [2003] and on line strength corrections from [*Funk* 2000]. For the (0,0) $^{16}O_2$ the line strength data based on *Funk* [2000] are used, whereas the other data are taken from HITRAN2000. For the (0,0) $^{16}O^{18}O$ transitions and for the (1,1) $^{16}O_2$ transitions the spectroscopic data are also from HITRAN2000.

3.4.2 Line Shape

Under atmospheric conditions several processes prevent the observation of the natural line width. This is only observable, if spontaneous emission dominates the relaxation of the excited state. Under atmospheric conditions collisions between molecules is the dominant effect and induce relaxation. This leads to a spectral broadening of the monochromatic transition. In the following Doppler broadening and pressure broadening will be briefly discussed.

Doppler Broadening

The Doppler broadening is the dominant reason for line broadening for gases under low pressure conditions. The thermal motion leads to a shift in the absorbing frequency ω_0. The velocity of the absorbing gas molecules are distributed in the thermal equilibrium according the Maxwell's law with v_{mean} being the most likely velocity, e.g. [*Demtröder* 1998]:

$$I(\omega) = I(\omega_0) \exp\left\{\frac{-c(\omega - \omega_0)}{(\omega_0 v_{mean})^2}\right\} \tag{3.40}$$

This result is a Gaussian line shape with a half width at half maximum:

$$HWHM = 2\sqrt{ln2}\omega_0 v_M/c) = (\omega_0/c\sqrt{8kTln2/M}) \tag{3.41}$$

Here it has to be considered that the mean thermal velocity of the molecules depends on the mass M of the molecules and on temperature T.
This process is dominant for low pressure in high altitudes, where pressure broadening becomes negligible.

Pressure Broadening

Collisions between molecules lead to a spectral broadening of the spectral lines due to variations of the energy levels. This leads to the Lorentz profile:

$$\sigma(\nu - \nu_0) = \frac{S \cdot \gamma_L}{\pi\left((\nu - \nu_0)^2 + \gamma_L^2\right)} \tag{3.42}$$

γ_L denotes the half width at half maximum of the Lorentz line. As it is shown in Figure 3.1 the Lorentz line shape is more narrow at the line core compared to the Gauss profile. At the line wings the decrease is slower in comparison with the a Gaussian line shape.

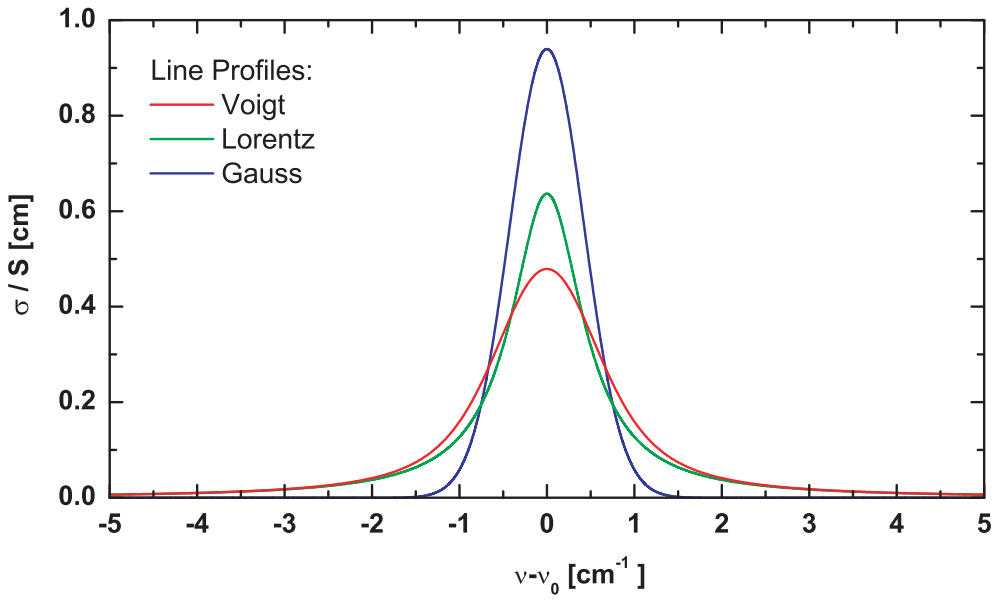

Figure 3.1: *Comparison of the most important spectral line profiles - Voigt, Lorentz and Gauss. The Voigt line has a full width half mean of* $1.5cm^{-1}$*. The Lorentz and Gauss lines have the same FWHM of* $1cm^{-1}$*. All lines are normalized to 1.*

The half width at half maximum depends on pressure and temperature:

$$\gamma_L(T,p) = \gamma_{L,0}\frac{p}{p_0}\left(\frac{T_0}{T}\right)^{0.76} \tag{3.43}$$

The constant 0.76 is empirical derived from measurements by *Ritter and Wilkerson* [1987]. $\gamma_{L,0}$ denotes γ_L at temperature T_0 and pressure p_0. As reference temperature T_0 the standard HITRAN temperature of 296 K is used [*Rothman et al.* 2003]. A typical Lorentz line width is $4.7pm \sim 0.08cm^{-1}$ at standard conditions. In the lower stratosphere and in the troposphere pressure broadening is the dominant effect.

Voigt Line Profile

The convolution of the Lorentz profile and the Gaussian profile leads to the so called Voigt Profile:

$$\sigma(\nu-\nu_0) = \frac{S_{\gamma_l}}{\gamma_D\pi\sqrt{\pi}}\int_{-\infty}^{+\infty}\frac{1}{(\nu-\nu_0-\delta)^2+\gamma_L^2}exp^{-\delta^2/\gamma_D^2}d\delta \tag{3.44}$$

Here it is assumed, that Doppler broadening and pressure broadening occurs independently. Figure 3.1 shows the discussed line shapes for equal conditions. The Voigt line has a full width at half maximum of 1.5 cm^{-1}, whereas the Lorentz and Gauss line have the same FWHM of 1 cm^{-1}.

Beyond Voigt line Profile

Detailed studies indicate that the Voigt profile cannot reproduce measured oxygen absorption lines without leaving a significant residual structure *Ritter and Wilkerson* [1987]. This can be overcome by accounting for collision narrowing. All models (soft collision model, hard collision model, speed dependent) used by *Ritter and Wilkerson* [1987] showed an improvement in the fit results. In this study the Galatry line profile is used.
Dicke [1953] introduced the principle idea of collision narrowing. Collisions induce velocity changes, but only negligible phase changes in the emitted radiation. *Galatry* [1961] extended this theory taking the phase shifts in to account. A significant change in the velocity of the emitting/absorping system occurs after many collisions. This is the so called soft collision approximation. The Galatry profile is given by [*Ritter and Wilkerson* 1987]:

$$G(x,y,\eta) = \frac{1}{\sqrt{\pi}}Re\left(\int_0^\infty d\tau \exp\left\{-ix\tau - y\tau + \frac{1}{2\eta^2}[1-\eta\tau - exp(-\eta\tau)]\right\}\right) \tag{3.45}$$

y denotes the normalized collision broadening collision parameter and x is the frequency normalized by the Doppler half width. The narrowing parameter $\eta = 0.0145$ is empirically determined by *Ritter and Wilkerson* [1987]. The use of the Galatry line profile instead of the Voigt line profile is required, if an accuracy better than 5 % is aspired.

3.5 Spectrum Evaluation

This section describes the retrieval of the photon path length distribution from the measured spectra. The method and spectroscopic model underlying the analysis will be discussed in detail. In the case of a non constant path length, the path length distribution modifies the line shape. Therefore a nonlinear fit of the measured intensities is required.
A measurement process can be understand as the relation between the real quantities x_i and the measured quantities m_i, represented by the matrix $\mathbf{M}$:

$$\mathbf{m} = \mathbf{M} \cdot \mathbf{x} + \mathbf{e} \tag{3.46}$$

Here $\mathbf{e}$ represents the error vector, including systematical errors as well as statistical errors. For an ideal measurement this vector is equal to the zero vector and the matrix $\mathbf{M}$ is the unit matrix. Generally $\mathbf{M}$ has other entries than in the main diagonal, as the instrument, used for the measurements, introduces correlations between the measured values. For the spectroscopic measurements in this study, this matrix is given by the instrumental function M_λ, see section 4.1. In the following the variance $V = \sigma_i^2$ is used instead of the error vector $\mathbf{e}$.
The real quantities or more precisely the modelled real quantities $\mathbf{x}$ are described by a set of parameters $\mathbf{p}$:

$$\mathbf{x_i} = f_i(\mathbf{p}) \tag{3.47}$$

Aim of the data analysis is the description of the measurement according to the model using this set of parameters. To derive these parameters the data analysis algorithm minimizes the difference between model and measurement. This is done by least square fitting. A schematic overview of the data analysis algorithm is shown in figure 3.2.

3.5.1 Nonlinear Least Square Fit

The basic idea of a least square fit is to reduce the sum of the squared residual Δx. This vector is defined as the difference between data and model. In the simplest case

of uncorrelated data with the same standard deviation the quantity S is defined as:

$$S(p) = \sum_{i=1}^{N} \Delta x_i^2 \rightarrow Minimum \tag{3.48}$$

For a general case, described by a vector x with dimension n this equation can be written as:

$$S(\mathbf{p}) = \mathbf{\Delta x^T V^{-1} \Delta x} \rightarrow Minimum \tag{3.49}$$

$\Delta x = (x_i(\mathbf{p}) - m_i)$ is called residual vector. The matrix $\mathbf{V}$ can be identified as the covariance matrix $V_{ij} = \sigma_{ij}$. The covariances can be expressed by the correlation coefficient ρ_{ij} as $\sigma_{ij} = \rho_{ij}\sqrt{\sigma_i^2 \sigma_j^2}$. The correlation coefficient ranges from -1 to 1. If the data are uncorrelated ($\rho_{ij} = 0$), the quantity S can be calculated by:

$$S(\mathbf{p}) = \sum_{i=1}^{N} \frac{(x_i(\mathbf{p}) - m_i)^2}{\sigma_i^2} \tag{3.50}$$

If the measurement errors follow a normal distribution, S follows a χ^2 distribution. The method for this special case is referred to as chi-square fitting. In comparison to the general case, equation 3.49, the parameter set $\mathbf{p}^*$ has to be found with following restriction:

$$S(\mathbf{p}^*) = min\{S(\mathbf{p})\} \tag{3.51}$$

In the case of linearity in all parameters, the quantity y can be expressed by: $\mathbf{x} = \mathbf{A} \cdot \mathbf{p}$. By finding the inverted matrix $\mathbf{A^{-1}}$, this linear least square problem can be solved analytically, see e.g. [*Blobel and Lohrmann* 1998]. In the case of non-linearity more complex numerical methods or approximations are necessary to determine the parameter set $\mathbf{p}^*$. In the data analysis method a modified Levenberg Marquard algorithm is used, implemented in the MIGRAD minimizer of MINUIT [*MINUIT* 1992].
For the error estimation, the Hesse matrix defined as $H_{ij} = \partial^2 S / \partial p_i \partial p_j$ is calculated to derive the errors for S[2].

[2]For nonsymmetric errors ($|-\Delta p_i| \neq |+\Delta p_i|$) the MINUIT function MINOS is also implemented in the data analysis program. In practice, the errors calculated from HESSE and MINOS only differ slightly, with the absolute HESSE error being smaller than the MINOS error. In this study the HESSE error is calculated to reduce computing time.

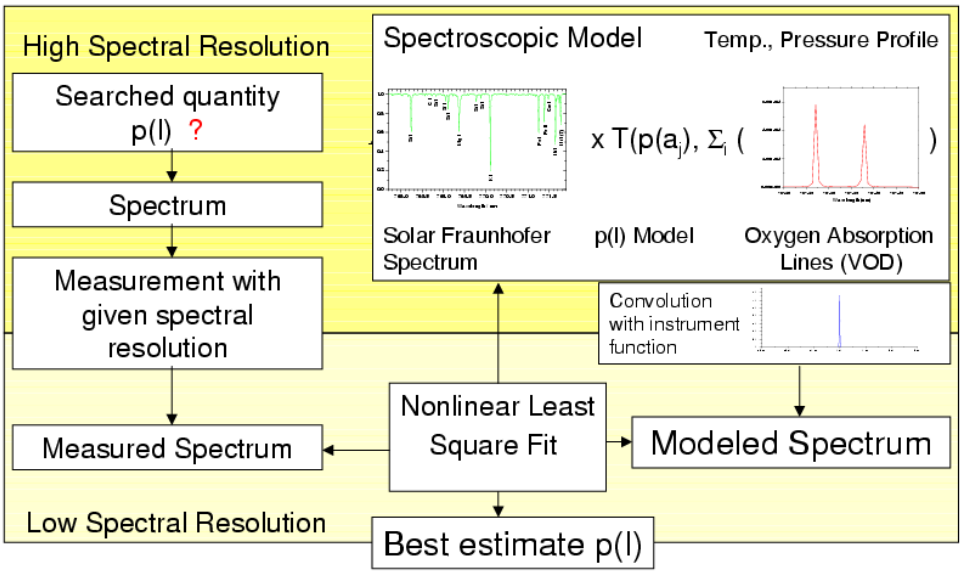

Figure 3.2: *Schematic view of the photon path length retrieval process. The spectral calculations are performed at high spectral resolution. The fit optimizes the parameter of the PDF model. The Nonlinear Least Square Fit yields the best estimated values for the different moments of the PDF.*

3.6 Measured Spectra

The raw detector signal from the CCD chip has to be corrected for the different background and noise signals. The offset signal **O** is measured by adding up a large number of scans N_O without illumination using the shortest possible exposure time. The dark current signal **D** is obtained by a long exposure time T_D measurement. Then the background is calculated by:

$$b_i = \frac{N_m}{N_O} O_i + \frac{T_m}{T_D} \frac{1}{N} \sum_{j=1}^{N} D_j \tag{3.52}$$

Here T_m is the measurement time for N_m added scans for the measured spectra and N is the number of used channels. As the dark current is not equal for all channels due to hot pixels (pixel with significantly higher or lower dark current), a correction of the dark current has to be applied. The measured spectrum **m'** has to be corrected for the background **b**:

$$\mathbf{m} = \frac{\mathbf{m}' - \mathbf{b}}{\mathbf{a}} \tag{3.53}$$

a is the relative acceptances vector for the individual channel, free from background. To retrieve **a** a halogen lamp is mounted in front of the entrance optics. This light source exhibiting a smooth spectrum is measured without passing the atmosphere. Furthermore the error due to shot noise has to be calculated. The shot noise of the photo electrons is the main source of error. For large electron numbers it is distributed according to the normal distribution. The standard deviation σ_s calculated by: $\sigma_{s,i} = \sqrt{g \cdot (m'_i - b_i)}/g$, where g is the electron number corresponding to 1 count. The offset readout noise for a single channel and readout process is given by:

$$\sigma_O^2 = \frac{1}{N_0 N(N-1)} \sum_{i=0}^{N} (O_i - \mu_0)^2 \qquad \text{with} \quad \mu_0 = \frac{1}{N} \sum_{i=1}^{N} O_i \tag{3.54}$$

The shot noise of the dark current is another instrumental error. It is calculated by:

$$\sigma_d = \frac{\sqrt{g \cdot \mu_d}}{g} \qquad \text{with} \quad \mu_d = \frac{T_m}{T_D} \frac{1}{N} \sum_{i=1}^{N} D_i \tag{3.55}$$

All errors contribute quadratically to σ'_i. Finally the acceptance correction error must be taken into consideration:

$$\sigma_i = m_i \sqrt{\frac{\sigma'^2_i}{(m'_i - b_i)^2} + \frac{\sigma^2_{a,i}}{a_i^2}} \tag{3.56}$$

with $\sigma_{a,i} = \sqrt{g \cdot a_i}/g$. The resulting measurement and error vectors have to be normalized. This is done by division by max $\{m_i\}$.

3.7 Spectroscopic Model

The absorption of light in the atmosphere is the most relevant physical process. It is described by Beer's law, see Equation 2.15. As the absorption cross sections for the different oxygen lines are very well known and are used as fixed parameters, the different moments of the photon path length distribution in the atmosphere are the only free parameters in the model. The path lengths are always given in units of Vertically-integrated Oxygen Density (VOD). This means, that for direct light measurements the mean photon path is directly given by the air mass factor (AMF, see 2.3). This is used for validation of the spectroscopic model, since for all

measurements (direct light and scattered light) the AMF is known.
For the derivation of the photon path length distributions the knowledge about the atmospheric conditions at the experimental site is necessary. For this purpose every three hour radiosondes where launched measuring temperature, humidity, air pressure and other meteorological parameters. The vertical profiles are extended to top of atmosphere using the barometric height formula together with the US standard atmosphere [*NOAA* 1976] temperature gradient. For the calculations the atmosphere is divided into n_{atm} layers with similar vertical air column, since the needed parameters are not constant in the atmosphere. In this study 40 vertical layers were used. The calculation of the layer boundaries uses the height of the closest measured pressure using the barometric height formula. The mean layer temperature is the pressure-weighted linearly interpolated temperature from the input profile. This mean temperature is used to calculate the line strengths according to equation 3.39
A base reference $\tau_i(\lambda)$ is calculated by multiplying the layer column density c_i with the cross section $\sigma_i(\lambda)$ and added up over all atmospheric layers:

$$\tau_i(\lambda) = \sum_{l=1}^{n_{atm}} c_i \cdot \sigma_i(T_l, p_l, \lambda) \tag{3.57}$$

Besides the atmospheric oxygen absorption, also the so called Fraunhofer absorption lines have to be considered. The solar spectrum shows strong absorption structures. These structures come from atomic absorption in the photosphere of the sun. Since the Fraunhofer spectrum generated from balloons, satellites or high flying platforms do not have the required spectral resolution[3], a Fraunhofer reference is generated from ground based measurements. The Fraunhofer spectrum, used in this study, is originally generated by [*Funk* 2000] using a base spectrum taken from the Kitt Peak Solar Flux Atlas [*Kurucz et al.* 1984]. The measurements of this solar spectrum were performed at the Kitt Peak National Observatory at Tucson, Arizona using a high resolution FTS (1.5 pm resolution). To obtain the Fraunhofer spectral lines, it is necessary to separate these lines out of the total atmospheric absorption spectrum. For this purpose a direct light oxygen absorption spectrum is generated using the atmospheric parameters which were present during the measurements of the Kitt Peak Solar Spectrum[4]. Dividing the initial spectrum by the oxygen absorption line spectrum obtain the searched Fraunhofer reference spectrum. The logarithm is taken to generate the optical depth reference F(λ).

[3] a 'top of the atmosphere' extra-terrestrial Fraunhofer spectrum is not available yet. Installing a high resolution Fourier Transform Spectrometer (FTS) on board of the International Space Station (ISS) could provide this required spectrum important for atmospheric science.

[4] Temperature and Pressure Profiles can be requested from the Goddard automailer system by sending an email with date, longitude and latitude the profiles are requested for.

3.8 Direct Light Measurements

The direct light intensity is given by using F(λ) and $\tau_i(\lambda)$

$$I(\lambda) = \exp\left[-\left(a_0 \cdot F(\lambda + s_0) + \sum_{i=1}^{n_{ref}} a_i \cdot \tau_i(\lambda + s_i)\right)\right] \tag{3.58}$$

Here a_i are the retrieved air mass factors for the individual lines and a_0 being the Fraunhofer fit coefficient. The calculated high resolution spectrum has to be converted to a low resolution spectrum to account for the influence of the measurement. This is done by convoluting this spectrum with the instrument function $\mathcal{F}_\lambda$:

$$I'(\lambda) = I * \mathcal{F}_\lambda \tag{3.59}$$

and binning of the high resolution spectrum to the CCD camera channels:

$$I_i'' = \frac{1}{\Delta\lambda_i} \int_{\lambda-\Delta\lambda_i/2}^{\lambda+\Delta\lambda_i/2} I'(\lambda')d\lambda' \tag{3.60}$$

where $\Delta\lambda_i$ is the dispersion for channel i. Finally an additive and multiplicative polynominal P_a and P_m of degree n_a and n_m, respectively, are used to calculate the final model values:

$$x_i = P_m(i) \cdot I_i'' + P_a(i) \tag{3.61}$$

The additive polyominal takes a possible stray light pedestal into account, while the multiplicative ones accounts for broad band effects. These can be effects, like extinction due to continuum absorption or scattering, or instrumental artifacts.

3.9 Retrieval of Photon Path Length Distributions

For the analysis of the measured spectra the cloudy sky is divide into three parts. Above the cloud top a direct path is assumed. The cloud top height is obtained from simultaneous cloud radar measurements. For the separation of the absorption above the cloud $\exp(-AMF \cdot \tau_{above}(\lambda))$ is calculated, where $\tau_{above}(\lambda)$ is the vertical optical depth above the cloud top and $\tau_{cloudtop}(\lambda)$ is the vertical optical depth up to the cloud top, respectively:

$$\tau_{(above/cloudtop)} = \sum_{i=1}^{n_{ref}} \tau_i(\lambda + s_i)_{a/c} \tag{3.62}$$

The parameter s_i represent the shifts calculated from the direct light model fit. They are fixed to reduce the number of free parameters.
The part below the cloud top and the cloud itself is represented by the high resolution part of the model:

$$I(\lambda) = exp-(a_0 \cdot F(\lambda + s_0) + AMF \cdot \tau_{above}(\lambda)) \cdot T_{cloud}(\lambda) \tag{3.63}$$

Here a_0 is the Fraunhofer fit coefficient, $F(\lambda)$ is the Fraunhofer optical depth reference retrieved from the Kitt Peak Solar Flux Atlas and T_{cloud} is the atmospheric transmission below the cloud top. The calculation of T_{cloud} includes the different types of distribution functions described in section 4.4:

$$T_{cloud}(\lambda) = \frac{1}{N} \sum_{i=1}^{n_{PDF}} P_i(p_{PDF}) \exp\{-l_i \cdot \tau_{cloud}(\lambda)\} \tag{3.64}$$

P is the distribution vector. It contains a discretization of the photon path length distribution for n_{PDF} path lengths **l**. The only free parameters in the model are p_{PDF}. All described increments are shown in Figure 3.2, which gives a schematic overview of the spectrum evaluation process.
Several sensitivity and model studies were performed to evaluate this path length retrieval method. *Funk* [2000] has shown, that the instrument function has a huge influence on the retrieved path length distribution. For example an error of $\approx 3\%$ in the mean and $\approx 15\%$ in the second moment were caused by a 2% change in the width of the instrument function. It also has been shown, that the line shape of a single strong absorption line contains all information on the path length distribution. Since the resolution of the measurements is not high enough, a set of absorption lines is used instead to increase the reliability of the retrieval.

3.9.1 Retrieval of in-cloud photon path

Figure 3.3 shows the principle view of the cloudy sky radiative transfer for randomly scattered photons. The total path length of the photons is the sum of the direct path length from the top of atmosphere to the cloud top, the path length inside the cloud and the vertical path length from cloud base to the ground and reflections between the ground and the cloud base. For the calculation cloud base height (z_{base}) and cloud top height ($z_{base} + \Delta H$) are needed. These two quantities can be retrieved from cloud ceilometer and cloud radar measurements, respectively.

As mentioned in section 3.7 the photon path length is given in units of vertically-integrated oxygen density [VOD]. A photon passing the atmosphere vertically per-

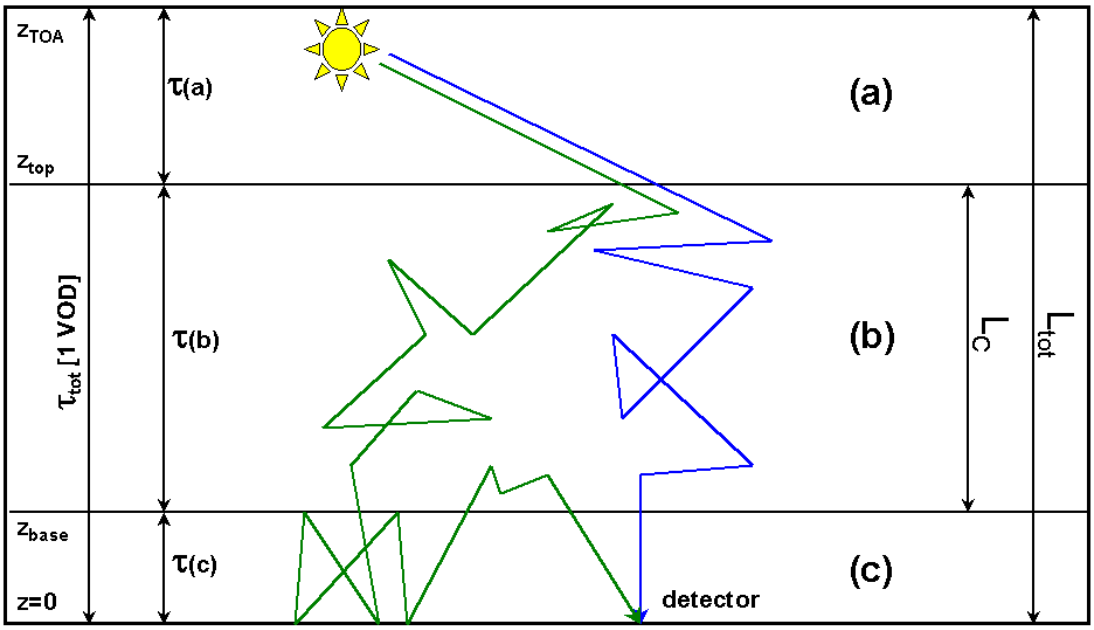

Figure 3.3: *Schematics of the cloudy sky radiative transfer for randomly scattered solar photons. To retrieve $\langle L_c \rangle$ the portions of $\langle L_{tot} \rangle$ under and above the cloud has to subtracted.*

pendicular to ground, travels a path of the length 1 VOD through the atmosphere. Knowing the altitudes of cloud base (z_{base}) and cloud top ($z_{\text{top}} = z_{\text{base}} + \Delta H$) from lidar and/or cloud radar, following optical paths through the atmosphere can be identified:

$$
\begin{aligned}
\tau_{O_2\text{col}}(\lambda) &= \tau_{O_2}(\lambda; 0, z_{\text{TOA}}) \\
\tau_{(\text{a})}(\lambda) &= \tau_{O_2}(\lambda; z_{\text{top}}, z_{\text{TOA}}) / \cos(\text{SZA}) \\
\tau_{(\text{b})}(\lambda) &= \tau_{O_2}(\lambda; z_{\text{base}}, z_{\text{top}}) \\
\tau_{(\text{c})}(\lambda) &= \tau_{O_2}(\lambda; 0, z_{\text{base}}) \cdot [1 + \frac{5 A_{\text{g}} R_{\text{c}}}{1 - A_{\text{g}} R_{\text{c}}}]
\end{aligned}
$$

The 1st and 3rd are straightforward vertical paths (hence optical depths), while the 2nd and 4th are respectively slant and more complex paths. The last expression for the oxygen path cumulated below the cloud is explicitly a correction term for

multiple ground/cloud base reflections.

For simplicity, it is estimated with a summed geometric series in $A_g R_c < 1$. Here R_c is the cloud reflectivity and A_g is the ground albedo. The geometric series is multiplied twice the hemispherical flux-weighted mean of the cosecant (which is 2) for both upward and downward path, plus one more VOD to get straight back into the instrument. In summary the correction is indeed:

$$\left(2 \times \frac{\int_0^1 (1/\mu)\mu\mu}{\int_0^1 \mu\mu} + 1\right) \sum_{N \geq 1} (A_g R_c)^N = \frac{5 A_g R_c}{1 - A_g R_c} \tag{3.65}$$

with $\mu = \cos(\mathrm{ZA})$.

In order to obtain the requested quantities $\langle L_c \rangle$ and $\langle L_c^2 \rangle$, the first moment $\langle L_{tot} \rangle$ and second moment $\langle L_{tot}^2 \rangle$ of the total photon PDF, inferred from the spectroscopic measurements, have to be corrected. Therefore the different contributions to the total photon path length have to be inspected:

- Above the clouds, it is assumed, that photon paths are slant bur no scattering occurs. Thereby photon path length are δ-distributed. This leads to the following expression, which is the vertical path length from TOA to the cloud top multiplied with the airmass factor for the inspected observation.

$$\langle L_{above} \rangle = \sqrt{\langle L_{above}^2 \rangle} = L(z_{top}, \infty) / \cos(SZA) \tag{3.66}$$

- Below the cloud base, multiple ground/cloud base reflection is assumed leading to an additional path length enhancement. For the calculation $R_c \approx 0.6$ [*Crewell et al.* 2004] and $A_g = 0.35$ for agriculture green land [*Wendisch et al.* 2004] are used. Both quantities are measured at 770 nm by an airborne albedometer instrument during the BBC1 and BBC2 campaigns.

$$\langle L_{below} \rangle = \sqrt{\langle L_{below}^2 \rangle} = L(0, z_{base}) \times \left(1 + \frac{5 A_g R_c}{1 - A_g R_c}\right) \tag{3.67}$$

- Photons can be reflected at the ground and penetrate into the cloud bottom and after multiple reflection return to the ground. [*Davis et al.* 1999] dealt already with this problem motivated by cloud lidar studies. Therefore a short laser pulse is used to illuminate the cloud base. The spatial and time distribution of the reflected light is recorded and analyzed to obtain different cloud parameters.

$$\langle L_{\text{refl}} \rangle \approx 2\chi \times L(z_{\text{base}}, z_{\text{top}}) \tag{3.68}$$

with $\chi = 0.7014$ derived from [*Case and Zweifel* 1967]. This expression is strictly speaking valid only for homogeneous cloud layers. [*Davis et al.* 1999] found a different expression for $\sqrt{\langle L^2_{\text{refl}} \rangle}$. Nevertheless, equation 3.68 is used to account for the mentioned phenomenon of cloud penetrating photons as the term above is good for the required correction.

Finally, the moments of the total photon PDF and for the in-cloud photon PDF are connected by simple relations. For the first moment the addition of the different contribution above and below the cloud to the in-cloud photon path yields:

$$\langle L_{\text{tot}} \rangle = \langle L_{\text{c}} \rangle + \langle L_{\text{above}} \rangle + \langle L_{\text{below}} \rangle + < L_{\text{refl}} > \times \frac{A_{\text{g}}}{1 - A_{\text{g}} R_{\text{c}}} \tag{3.69}$$

The contribution concerning the cloud-penetrating photons (last term) is also multiplied (see $\langle L_{\text{below}} \rangle$) with a weighting term to account for ground/cloud base reflections. For the second moment, it is assumed, that the variance for the in-cloud photon PDFs is equal the variance of the total photon PDFs. Therefore the simple relation is valid:

$$\langle L^2_{\text{c}} \rangle = \langle L_{\text{c}} \rangle^2 + \langle L^2_{\text{tot}} \rangle - \langle L_{\text{tot}} \rangle^2 \tag{3.70}$$

To illustrate the magnitudes of all contributions, the correction of the photon PDF is shown exemplarily for the observation on May 11, 2003, UT 14:59. Figure 4.9 shows in the upper panel the measured and simulated absorption spectrum for this observation. In the lower panel the retrieved photon PDF assuming a Γ distribution is shown. For the first moment $\langle L_{\text{tot}} \rangle = 2.165$ VOD and for the second moment $\langle L^2_{\text{tot}} \rangle = 5.94$ VOD^2 is retrieved, respectively.
The cloud top height and cloud base is retrieved from cloud radar and ceilomter measurements. In the upper panel of figure 5.14 the corresponding cloud radar image is shown. For the inspected observation date , marked in figure 5.14, a cloud base height of 1950 m (0.78 VOD) and a cloud top height of 5400 m (0.51 VOD) is retrieved, respectively. Hence the geometrical thickness of the cloud is $\Delta H = 3450$ m (0.27 VOD). From the simultaneously measured liquid water content (see lower panel of figure 5.14) the cloud optical thickness is calculated. For this exemplary case, equation 3.10 yields $\tau^*_{\text{c}} = 2.2$. The SZA for this specific date is 52.25°.
Accordingly, for the photon path above the cloud $\langle L_{\text{above}} \rangle = \sqrt{\langle L^2_{\text{above}} \rangle} = 0.832$

VOD is obtained. Below the cloud the photon path is $\langle L_{\text{below}} \rangle = \sqrt{\langle L^2_{\text{below}} \rangle}$ = 0.504 VOD. The contribution of the cloud penetrating photons to the total path is $\langle L_{\text{refl}} \rangle = 0.385$ VOD. This leads to a first moment of the in-cloud photon PDF of $\langle L_{\text{c}} \rangle = 0.659$ VOD and a second moment of $\langle L^2_{\text{c}} \rangle = 1.687\ \text{VOD}^2$, respectively.

The resulting quantities $\langle L_{\text{c}} \rangle$ and $\langle L^2_{\text{c}} \rangle$ are used together with the measured cloud optical depth (retrieved from simultaneous liquid water path measurements using microwave radiometer) and measured geometrical vertical extension retrieved from cloud radar measurements to verify the theoretical predictions in section 3.1.4 and 3.1.5, respectively. The results of this inspection are presented and discussed in chapter 5. For the given example the corresponding data points ($\langle L_{\text{c}} \rangle$ / $\Delta H = 2.24$ and $\langle L^2_{\text{c}} \rangle^{0.5} / \langle L_{\text{c}} \rangle = 1.97$) are marked in figure 5.21 and figure 5.22 by grey circles, respectively.

Chapter 4

Instrumentation

This chapter describes the instrumental aspect of this study. First, the instrumental setup used for the oxygen A-band measurements is described in detail. Then, measurements to evaluate the sensitivity of the instrumental setup and out-of-band rejection measurements are discussed.

4.1 Grating Spectrometer

To perform suitable oxygen A-band measurements for photon path length distribution studies, a high resolution spectrometer is necessary to separate the individual oxygen absorption lines. Therefore, a minimum resolution of 1 cm $^{-1}$ or 59 pm at 770 nm is required. The retrieval of the photon path length distributions requires the analysis of a set of lines or the line shape of a single strong absorption line. This means that the resolution has to be in the order of the actual line width (6 pm or 0.1 cm^{-1}). For this purpose, Fourier transform spectrometers (FTS) or grating spectrometers with large focal lengths can be used. Though modern FTS can achieve resolutions better than 0.01 cm^{-1}, these systems are not suitable for cloudy sky measurements [*Nägele* 2002]. FTS receive their spectral information using brightness variability in measured interferograms. However, it is impossible to distinguish between the variable brightness of a cloudy sky and the brightness variability inherent in the measurement method. Therefore, a grating spectrometer is used for the spectral measurements. Grating spectrometer systems have no problems with variable sky brightness due to the instantaneous spectral decomposition of the incoming light.

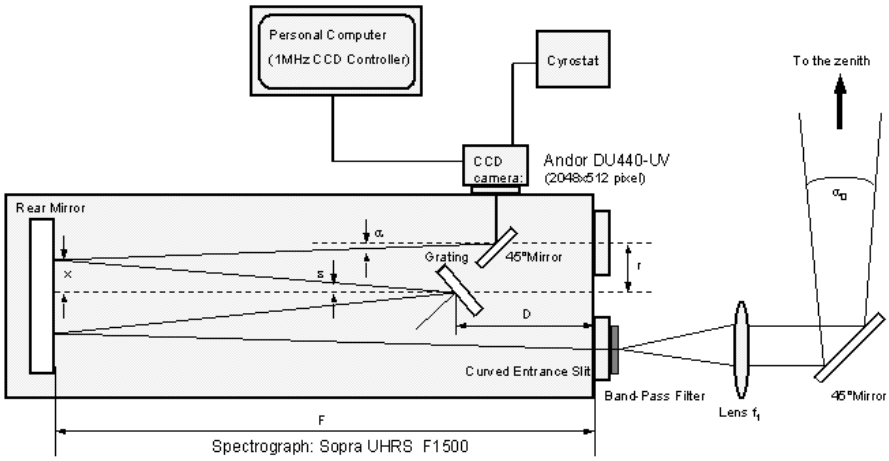

Figure 4.1: *Instrumental set-up for high resolution spectroscopic oxygen A-band measurements of zenith scattered skylight. The entire instrument is mounted inside a portable container laboratory to allow shipment to measurement sites.*

4.1.1 Instrumental set-up

The instrument used for the ground based, passive spectroscopic measurements consists of three major components (Figure 4.1) : (1) light intake entrance optics facing the solar zenith with a field of view of 1°. (2) a Fastie Ebert grating spectrometer (SOPRA UHRS F1500) and (3) a CCD camera (Andor DU440-UV with Marconi EE42-10 detector, (2048 x 512 pixel)). A more detailed description of the individual components is given in the following subsections.

Monochromator

The spectrometer is designed as a Fastie-Ebert mount, which is a modified Czerny-Turner mount in which a single large concave mirror serves as collimator and camera mirror. Through this arrangement, a small angle ε is achieved between the incoming and diffracted beam.

A dielectrical interference optical band filter with a central wavelength of 771.4 nm and a FWHM of 11.2 nm is mounted directly in front of the entrance slit to reduce stray light and suppress the superpositions of unwanted reflection orders on the grating. When measuring a discrete emission line, a maximum transmission of 72 % is found in the center of the line, and the attenuation on either side is found to be better than 99,85 %. The width of the entrance slit is 70 μm.

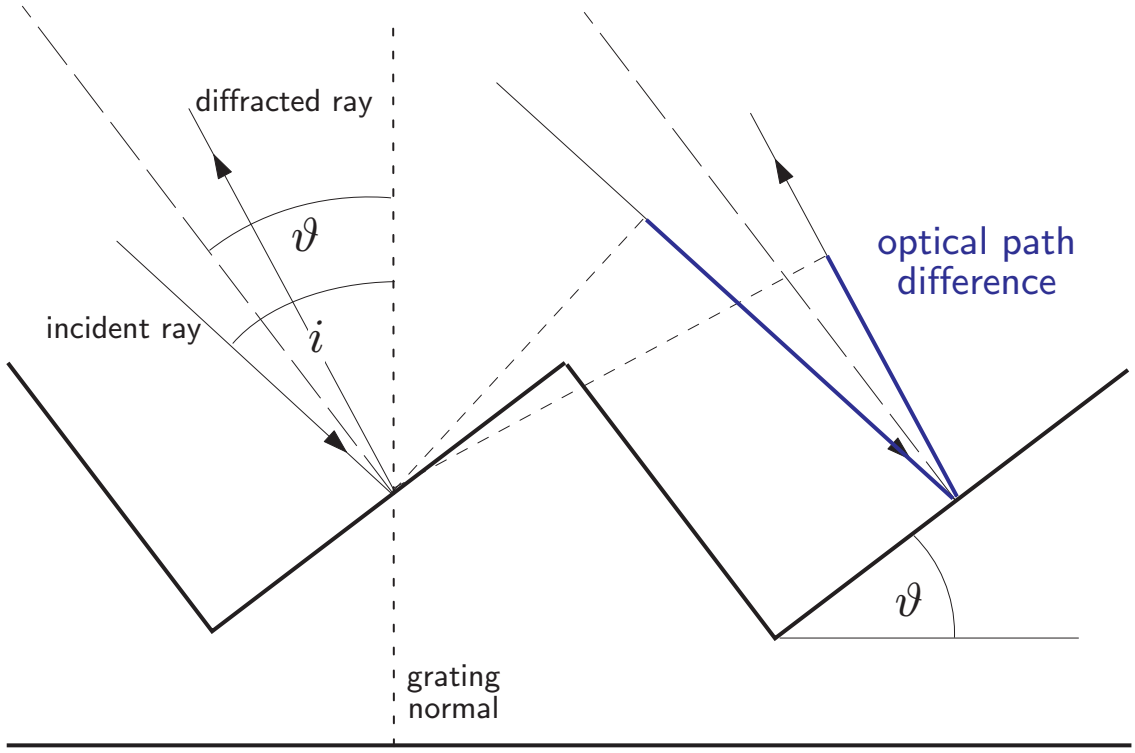

Figure 4.2: *Schematic of an Echelle grating. The maximum efficiency is obtained when the angle of incidence i equals the blaze angle ϑ. The grating used in this thesis has a blaze angle of* $63°26'$

The spectrometer has a focal length f of 1500 mm and a numerical aperture of f/13.5. The grating has a ruling density of 316 rulings/mm and a size of 206 x 106 mm^2. Even with this relatively low ruling density, high spectral resolutions are possible because Echelle gratings are optimized for high order use (Figure 4.2). Here, the grating is operated in the 7th order. The angle of the incoming light i on the grating is given by [*Sopra*]:

$$2 \cdot \sin(i) \cos(\varepsilon) = kN\lambda \tag{4.1}$$

where $\varepsilon = 3.24°$ is the Ebert angle, k is the grating order, N is the ruling number and λ is the wavelength in nanometers. For a wavelength of 770 nm, the incoming light angle amounts to 58.54°. The theoretical dispersion is given by following relation with f as the focal length:

$$D = \frac{\lambda}{2\ f\ tan(i)} \tag{4.2}$$

The theoretical dispersion for the 7th order is 0.157 nm/mm.

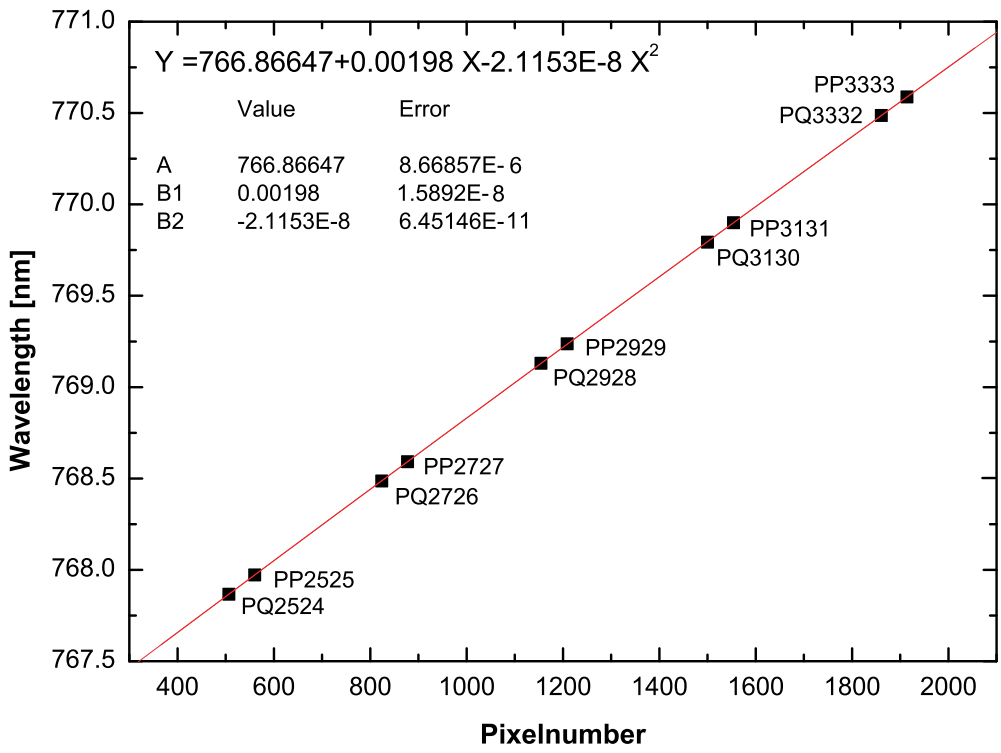

Figure 4.3: *Dispersion function for the used SOPRA F1500 spectrometer. A second order polynominal is used to approximate the function.*

To avoid interpolation errors in the analysis of the spectra, the FWHM of a spectral line must cover at least 5 pixel on the detector (see [*Roscoe et al.* 1996]). As described in the following subsection, a CCD camera with a total detection area of 27.6 x 6.9 mm^2 and a pixel size of 13.5 μm is used as detector in this study. The theoretical channel dispersion is 2.12 pm/channel, and the measured value of 1.93 pm/channel (0.143 nm/mm) lies close to that theoretical value. The CCD-chip features a register well-depth of 600,000 electrons.

The spectral decomposition of the spectrometer system is characterized by the instrument and dispersion functions. The instrument function (also called point spread function) describes the response of the entire system to a discrete wavelength delta peak. It combines response function of the detector and the diffraction pattern of the slit and grating. In this sense, a measured spectrum I_m can be expressed as the spectrum of the incoming light I_S convoluted with the generally wavelength

dependent instrument function M_λ.

$$I_m(\lambda) = \int M_\lambda(\lambda') \cdot I_S(\lambda - \lambda')\, d\lambda' \tag{4.3}$$

A well known atomic emission line of e.g. Krypton is measured to determine the instrument function. A low pressure halogen spectral lamp (Pen-Ray Krypton lamp, 130 Pa nominal pressure) is used for this purpose. The theoretical Doppler FWHM of the used lamp is 0.97 pm at 100° C operation temperature. In the wavelength region around 770 nm, Krypton has two Kr(I) emission lines: one at 768.5244 nm and the other at 760.4538 nm (air wavelengths). As the second line is more prominent and the narrower of the two, it is used to determine the instrument function. The measured function is a convolution of the instrument function and the atomic emission line.

As the instrument function is more than 10 times wider as the emission line, the emission line's contribution to the measured width can be neglected. The instrument function is also used to determine the resolution of the spectrometer system. It is defined as the FWHM and is measured $\Delta\lambda = 13.5$ pm. The resulting optical resolution is R = 57037[1].

The dispersion function can easily be inferred from the measurements, since the wavelengths of the oxygen absorption lines are accurately known. Figure 4.3 shows the dispersion function. It is determined by fitting a second order polynominal to the measured oxygen absorption lines.

The entire system is assembled in an insulated housing to allow stable measurement conditions. Four fans circulate the air inside the housing, and a thermostat controlled electric heater provides temperature stability within ±0.1° C.

CCD Detector

A commercial spectroscopic CCD camera (Andor DU440-UV) with a 2048 x 512 pixel CCD chip (Marconi EEV CCD 42-10)and an 1 MHz readout controller card is used for the instrument's detector. The CCD is front illuminated chip to avoid shifting pixels due to etalon effects from reflecting chip backs. The coating of the chip and the entrance window is optimized for the near infrared region, providing a quantum efficiency of 45 percent at 770 nm. The CCD camera is fully controlled by the readout electronics.

[1] The theoretical resolution is given by $R = \lambda/\Delta\lambda = k \cdot N \cdot b = 480004$, which corresponds to $\Delta\lambda = 1.604pm \hat{=}$ 0.831 pm/channel.

The exposure times are dynamically chosen depending on the brightness of the sky. It is also possible to bin individual pixel columns or pixel groups. The temperature of the chip is set and controlled by the camera software. The measurements were performed automatically using a script written in specific Andor basic [*Andor* 1999] which includes dynamic control of the exposure time to guarantee an optimal saturation level of the CCD chip (see B).

The measured signal is composed of the photo electron signal and of several other contributions called background.

Due to thermal electron activation in the semiconductor material, photo detectors like CCD chips show a low current through the depletion area, even when no activation by means of the inner photo effect has taken place. This phenomenon is called dark current of the CCD chip. The camera used in this study is thermo electrically cooled with a Peltier element, the heat sink of which is temperature stabilized by a closed-circle water cryostat. During the measurements, the chip is cooled to a temperature of $-50°$C. To measure the dark current, the system is shut off from incoming light. The wavelength dependent sensitivity of the entire system is required later for the analysis of the measured spectra. The relative spectral sensitivity of the detector, the reflection efficiency of the grating and mirrors and the transmission function of the bandpass all contribute to the total sensitivity. Any measured spectra have to be corrected for varying spectral sensitivity and backgrounds as described in Section 3.6.

4.2 Out Of Band Rejection

Heidinger and Stephens have conducted several theoretical studies regarding oxygen A-band spectroscopy for atmospheric observations [*Heidinger and Stephens* 2000; *Stephens and Heidinger* 2000]. Among other points, an estimation of the amount of information contained in spectral measurements is presented. The number of significant pieces of information contained in the spectrum is represented by the amount of significant eigenvalues (relative to the noise properties of the instrument).The addition of further channels to achieve a higher accuracy in the performed measurements results in more significant eigenvalues and therefore an increase in the vertical resolution of the retrieval. As the error in the individual measurements increases, the addition of further channels offers less additional significant eigenvalues and little new profile information. Only by increasing the spectral resolution more vertical resolution becomes available. Heidinger and Stephens' analysis indicates that an A-band spectrometer with a spectral resolution of 0.5 cm^{-1} and an accuracy of 2% or better should be able to provide four or five independent pieces of information.

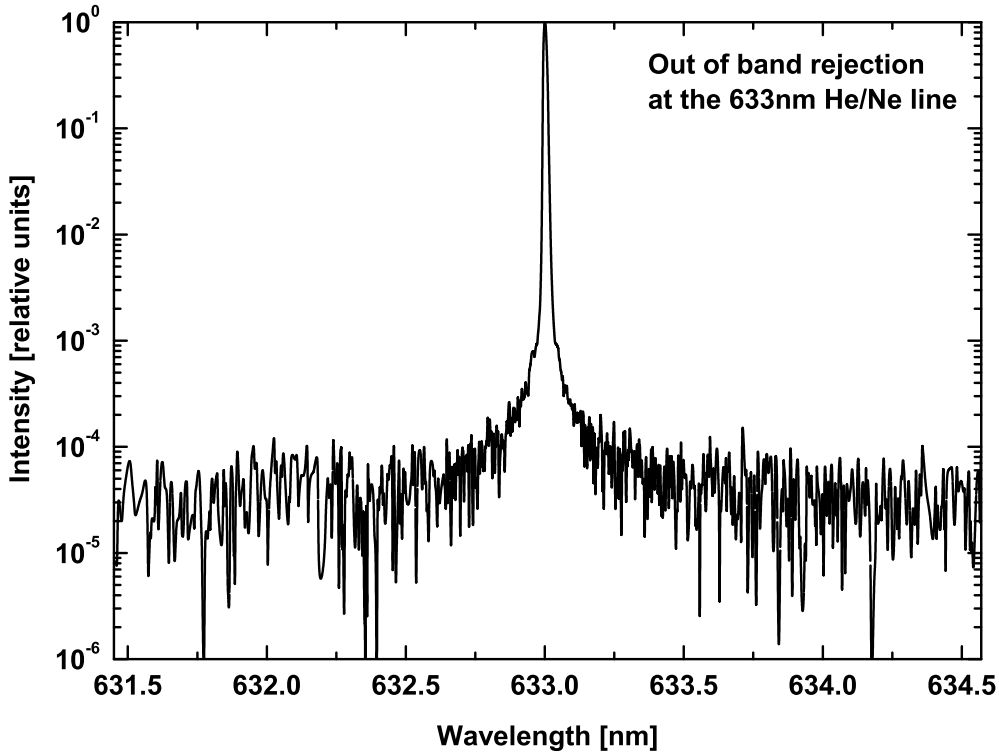

Figure 4.4: *Measured out of band rejection (OBR) for the HE/NE line at 633 nm. The OBR reaches values* $< 10^{-4}$ *for wavelengths 6 FWHM off the line center*

The out of band rejection (OBR) largely determines the possible number of independent parameters that can be determined in a spectral retrieval. In agreement with recent considerations from *Min et al.* [2004], the size of the relevant parameters indicate that the measurements should allow to infer four independent variables. Figure 4.4 shows the measured slit-scattering function of the 633 nm HeNe laser line. The measurements show that the achieved OBR is better than 10^{-4} with a FWHM resolution of 0.0135 nm (better than 0.5 cm^{-1}).
In the present study, two independent pieces of information are generally determined, in particular the first two moments of the assumed photon path length distribution.

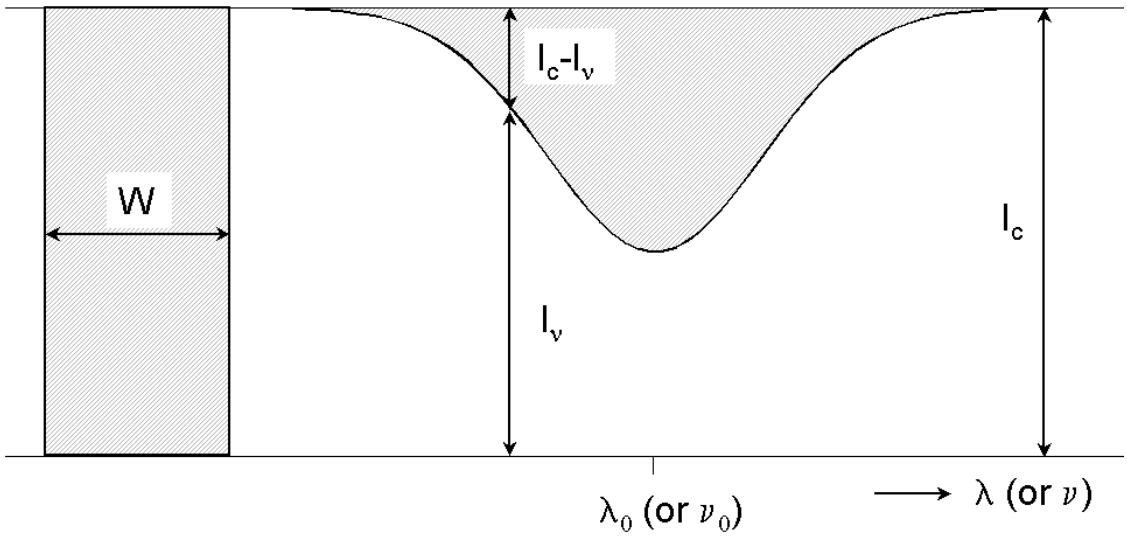

Figure 4.5: *Schematic and notations of the equivalent width W of an absorption line*

4.3 Direct Sun Measurements

The accuracy of the instrument function is validated by performing direct light measurements with the grating spectrometer. In this validations, sun light is reflected into the zenith looking telescope using a retractable mirror. The path through the atmosphere is well known for direct sun measurements, so they are well suited for accuracy validation of the instrumental function.

The validation measurements were performed during the BBC2 campaign in May 2003 with the same instrumental setup as the cloudy sky measurements. As the weather conditions did not allow continuous direct sunlight observations, measurements could only be recorded for certain AMFs. The atmospheric and meteorological data are taken from radio sonde launches. The minimum solar zenith angle is 32.06°, which corresponds to an AMF of 1.18. The AMFs are calculated from the sun-zenith distance at the time of measurement. Due to the geographical landscape geometry and the appearance of clouds, the maximum observed air mass

factor is 2.69. The same spectral range is observed in the direct light measurements as in the cloudy sky measurements.

Figure 4.5 gives a schematic overview of the notations in this section. The absorption at a wavelength λ or frequency ν is given by:

$$a(\nu) = \frac{I_c - I_\nu}{I_c} \tag{4.4}$$

Here c denotes continuum. The maximum absorption at the line center is

$$a(\nu) = \frac{I_c - I_{\nu_0}}{I_c} \tag{4.5}$$

This quantity is often denoted the central depth d. For a homogeneous photon path as is e.g. observed in direct sun measurements, the absorption can be written as:

$$a(\nu) = 1 - T(\nu) = 1 - exp(-k_\nu m) \tag{4.6}$$

The overall integral over ν is referred to as the equivalent width W:

$$W = \int a(\nu) d\nu = \int \frac{I_c - I_{\nu_0}}{I_c} d\nu \tag{4.7}$$

The relation between W and m is called curve of growth. The curve of growth describes how the line strength increases as the optical depth increases.

Equation 4.7 can be written as:

$$W = \int_{-\infty}^{\infty} [1 - exp(\tau)] dx \tag{4.8}$$

Goody and Yung [1989] showed, that the equivalent width can be calculated by:

$$W = \pi/2 \cdot I_{\nu_0} \cdot \text{FWHm} \tag{4.9}$$

The curve of growth is determined for each individual oxygen A-band line, especially for all (0,0)-transitions. Figure 4.6 displays an example of the measured equivalent width of the PP25,25 transition plotted against the AMF and compared to the theoretical predictions. For the calculation of the theoretical line equivalent width, the line shape is calculated for a given AMF and convoluted with the instrumental function. Therefrom the equivalent width W is determined. The measured equivalent widths for the discrete AMF are compared with the calculations (see equation 4.9). As the agreement between the measured and calculated W's is good, it indicates a correct description of the instrumental function.

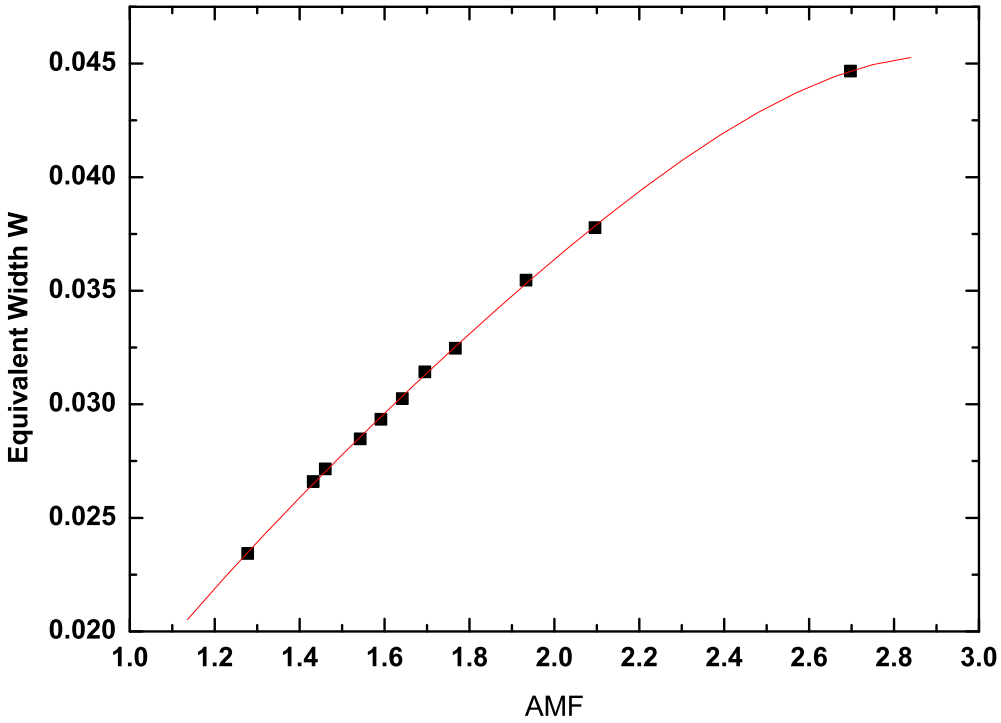

Figure 4.6: *Measured equivalent width of the PP 25,25 transition (black points) and theoretical prediction (red line)*

4.4 Sensitivity Tests

The photon path length is directly related to the strength of radiative absorption in the atmosphere and is therefore well suited to describe atmospheric radiative transfer. In order to examine the influence the assumed photon PDF has on the performed retrievals, several sensitivity tests using different distribution functions are presented in the following.

The necessity of assuming a statistical distribution to describe the photon path lengths can easily be shown by attempting a retrieval using a delta distribution. Figure 4.7 shows the obtained results for such a delta peak. The example measurement spectrum used for this particular study was measured on May 11, at UT 14:59. The upper panel shows the measured spectrum and the model spectrum retrieved by the photon PDF retrieval algorithm (see section 3.9). The middle panel of figure refresultdelta displays the resulting fit residuum. A significant restidual

structure can clearly be seen at the O_2 lines . Therefore, a detailed description of the oxygen absorption lines is not attainable when using a delta peak for the photon path length distribution.

The previous result indicates that for the description of the photon PDF a narrow distribution function is not applicable. In the following wider distribution functions (log-normal distribution and Gamma distribution) are used. Both distributions have with a single peak.

The log-normal distribution represents a the distribution of a statistical variable whose logarithm follows a normalized Gaussian PDF:

$$p(x) = \frac{1}{Sx\sqrt{2\pi}} \exp\left\{-\frac{(\ln x - M)^2}{2S^2}\right\} \tag{4.10}$$

with the real parameter S and the positive real parameter M. The low order moments are:

$$\mu = e^{M+S^2/2}, \qquad m_2 = e^{2(M+S^2)}, \qquad var(x) = e^{2M+S^2}(e^{S^2} - 1) \tag{4.11}$$

Figure 4.8 shows the results of the photon PDF retrieval assuming a log-normal distribution. The residuum shows some, however smaller spectral features left indicating that the log-normal distribution is not suited to describe the photon PDF for this case.

Van de Hulst [1980] demonstrates that the Gamma distribution is a good approximation for the photon path distribution for homogeneous slabs. *Pfeilsticker et al.* [1998] verifie its applicability for experimental absorption data and *Marshak et al.* [1995] show, that it can also be used to describe the displacement of photons escaping from fractional as well as homogeneous cloud layers. Gamma distributions represent a class of universal probability density functions that quickly decrease on either side of their respective center. They are composed of an exponentially decreasing term and a potentially growing term. Using the mean path length $\langle x \rangle$ as the parameter, the gamma distribution can be written as:

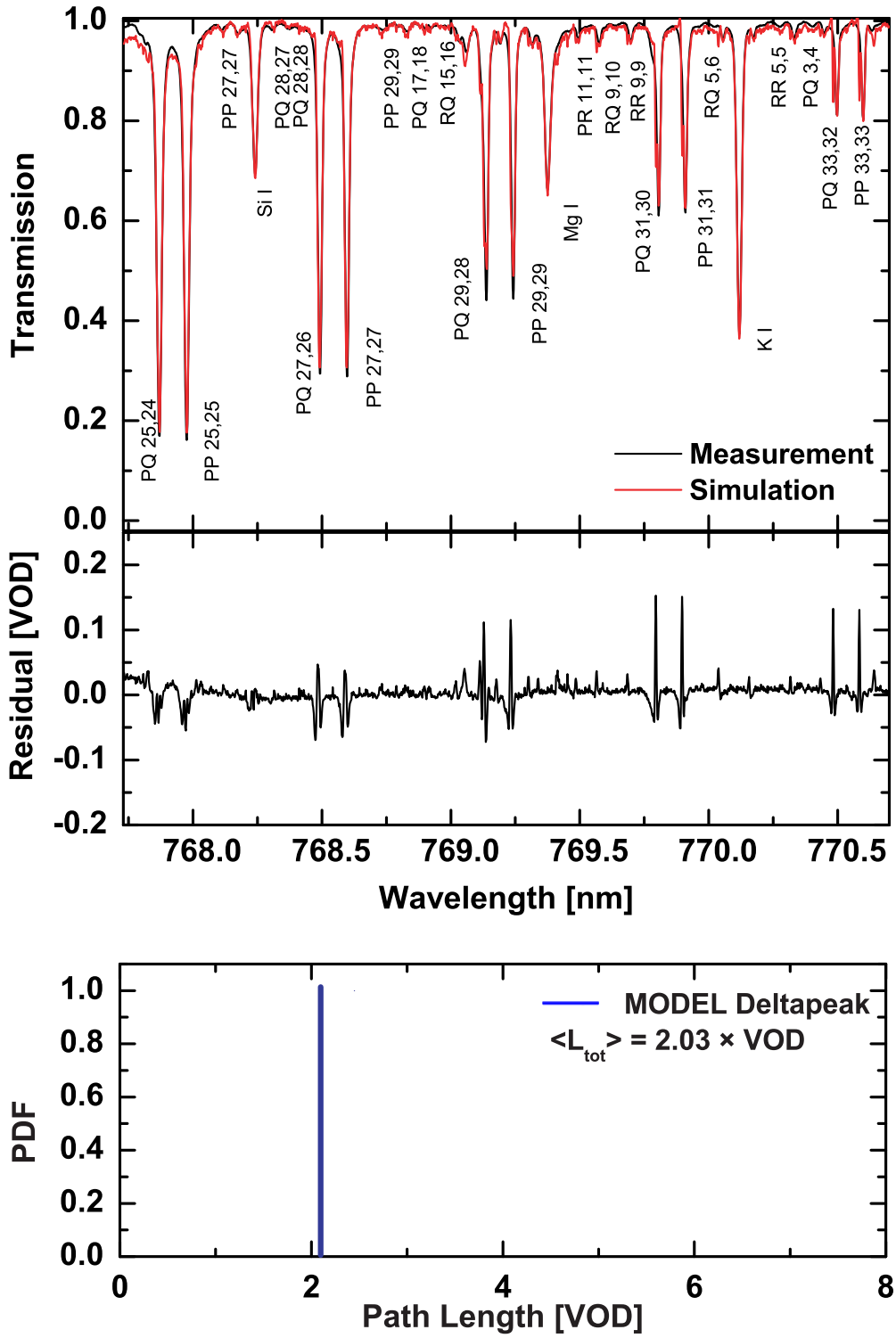

Figure 4.7: *Upper panel: Comparison of measured (black) and simulated (red) oxygen A-band spectrum for the observation at Cabauw/Netherlands on May 11, 2003 at UT 14:59. The identification of the oxygen a band and solar Fraunhofer lines is given next to each line. Middle panel: Residual spectrum composed of the ratio of the measured and the simulated spectra. Lower panel: Inferred probability density function (PDF) of photon path lengths assuming a delta distribution.*

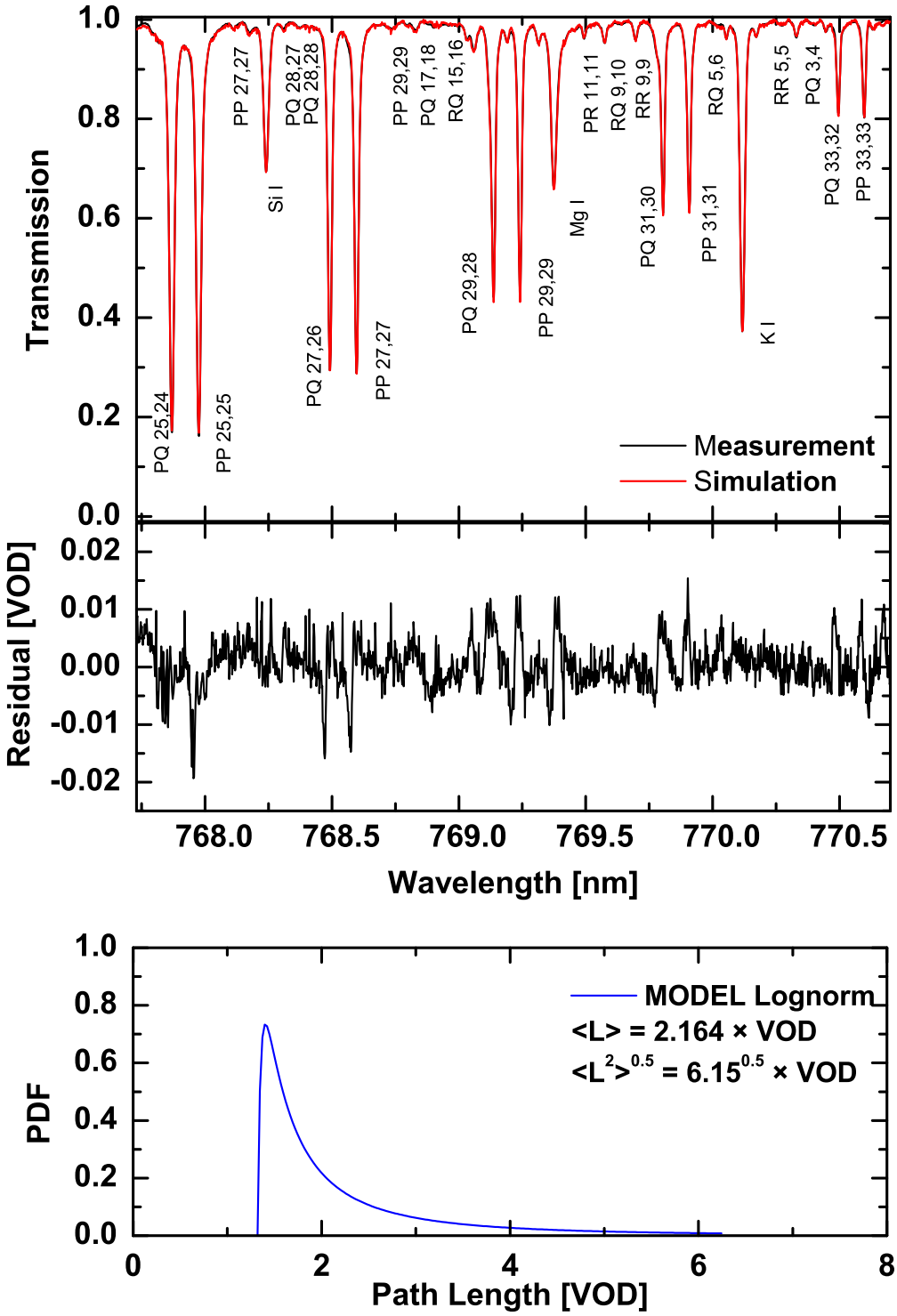

Figure 4.8: *Upper panel: Comparison of measured (black) and simulated (red) oxygen A-band spectrum for the same observation as Fig. 4.7 Middle panel: Residual spectrum. Lower panel: Inferred probability density function of photon path lengths assuming a lognorm type distribution.*

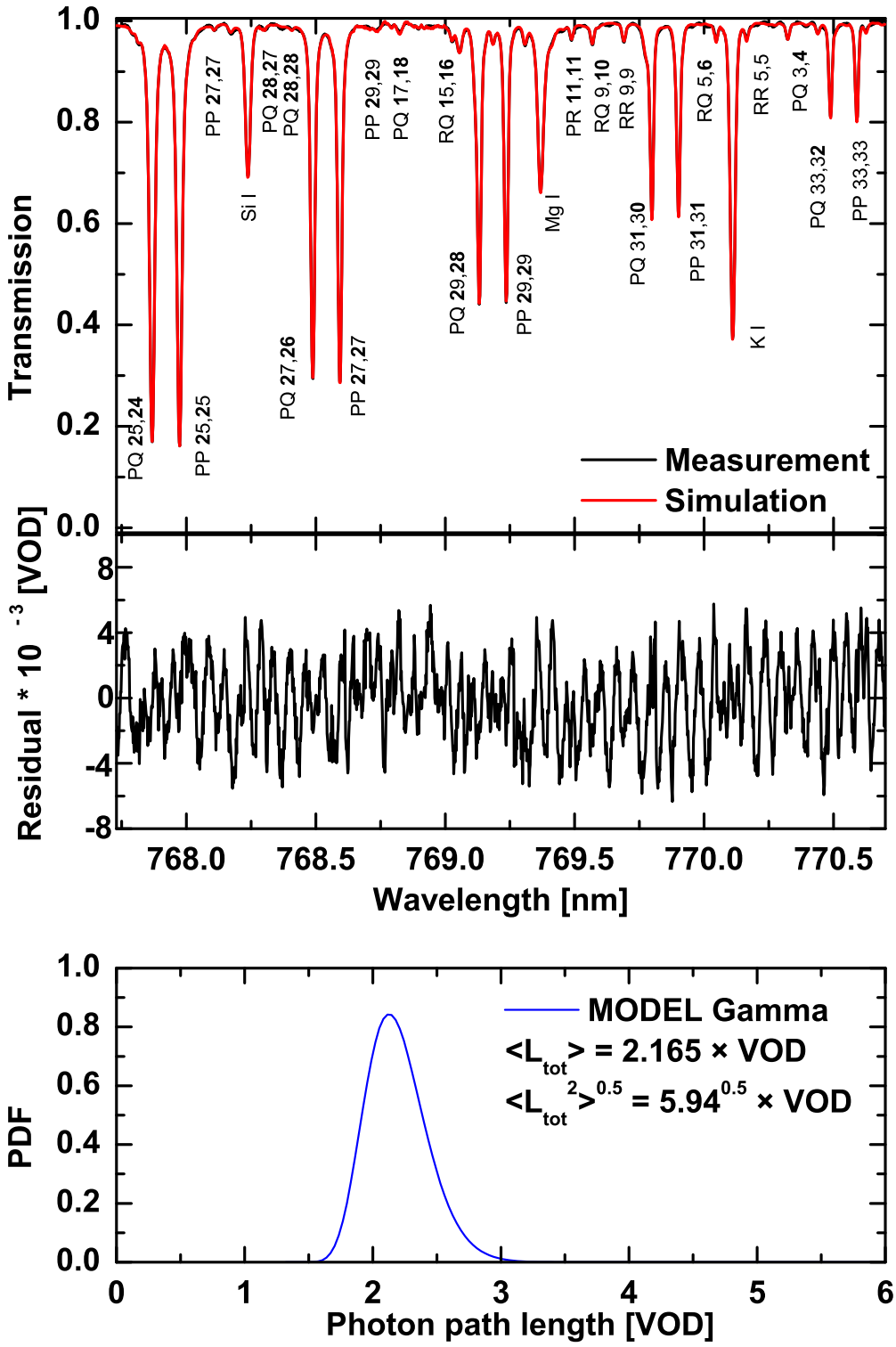

Figure 4.9: *Upper panel: Comparison of measured (black) and simulated (red) oxygen A-band spectrum for the same observation as Fig. 4.7 Middle panel: Residual spectrum. Lower panel: Inferred probability density function of photon path lengths assuming a gamma type distribution.*

$$p(x) = \frac{a}{\Gamma(\kappa)\left(\frac{<x>}{\kappa}\right)^{\kappa}} x^{\kappa-1} e^{-\frac{\kappa x}{<x>}} \tag{4.12}$$

Here, $\Gamma(\cdot)$ is the Euler Gamma function. The variance or second moment is given by:

$$V(x) =< x^2 > - < x >^2 \tag{4.13}$$

The parameter κ can then be defined as

$$\kappa = \frac{< x >^2}{V(x)} \tag{4.14}$$

Figure 4.9 shows the results of the photon PDF retrieval assuming a gamma distribution for the photon path length. The analyzed spectrum is the same as in previous test. The residuum shown in the middle panel is significantly smaller than that obtained when assuming a the delta peak distribution. In comparison with the residuum obtained from the log-normal distribution no spectral features left.

4.5 Model calculation and validation of the used method

As a part of this study, the cloud model GESIMA and Monte Carlo radiative transfer model Grimaldi were evaluated in cooperation with the radiative transfer modelling group of the Leibniz Institute of Marine Sciences at Kiel University (IFM-GEOMAR). For this purpose, a high resolution transmission spectrum is calculated using a randomly selected model cloud. This spectrum is then used as input for the path length distribution evaluation model (see 3.3), which is also used for the analysis of the measured spectra presented in chapter 5.

4.5.1 The GESIMA cloud model

GESIMA (**Ge**esthacht **Si**mulation **M**odel of the **A**tmosphere) is a three dimensional, non hydrostatic atmospheric model developed at the GKSS research center. It has a mesoscale horizontal resolution with grid cells of sizes between between 1 and 250 km. The advantage of models with mesoscale resolutions lies in the ability to focus on distinct areas, in which the physical processes can be described in added detail. In the GESIMA model, special efforts were made to parameterize the boundary layer, cloud development, and cloud interaction with solar radiation. The parameterization introduced by *Levkov et al.* [1992] is used in describing the cloud

microphysics.

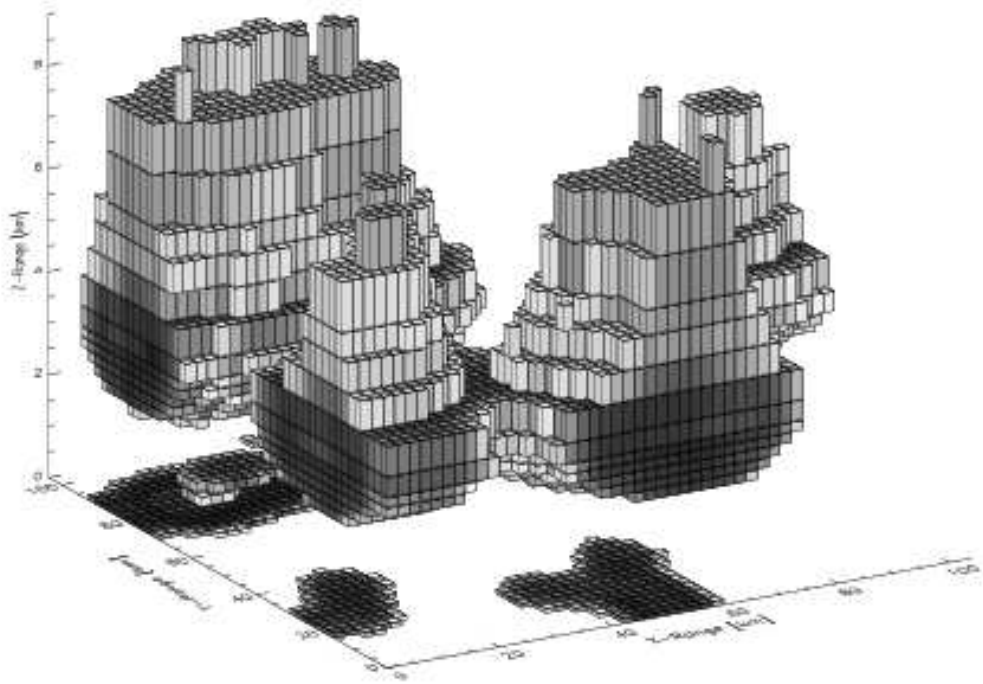

Figure 4.10: *Illustration of a cloud created by the GESIMA model. Dark boxes mark areas of high cloud extinction.*

An array of 52 × 52 × 26 grid boxes is used to describe cloud generation. With a horizontal resolution of 2 km, the model area has a total extension of 104 × 104 km. The vertical grid size varies from 100 m in the boundary layer up to 1000 m in the upper layers. In total, the model area extends over 10 km in vertical direction. The atmospheric initialization conditions used for cloud modelling were randomly chosen from a database of radiosonde data. This data set contains temperature and humidity profiles measured over the last few years over Europe and the North Atlantic. In the vertical direction, pressure, temperature and humidity profiles were overlaid on the grid boxes, while homogeneous starting conditions were assumed in horizontal direction. The GESIMA model is always initialized with an empty, cloud free area, and clouds only develop during the model run.

Adding humidity disturbance into randomly chosen areas near to the ground results in over-saturation. This subsequently results in an unstable atmospheric layering and activates convection. Because of the basic concept of the implemented

cloud modelling processes, the existing GESIMA clouds are convective and show high internal variability. Each grid box contains information about the basic physical properties like temperature, pressure and humidity and additional information such as liquid water content, effective cloud radius or rainfall rates.

4.5.2 The GRIMALDI Monte Carlo Model

The Monte Carlo method allows the description of three dimensional radiative transfer in inhomogeneous clouds. Using this method, the path of individual photons through the atmosphere can be modeled by simulating scattering and absorption events on gas molecules and hydrometeors. The Monte Carlo method has established itself in radiative transfer modelling in the atmosphere, especially for the problem of path length distributions. The elementary processes of scattering and absorption, as well as the free path length, are represented by probability distributions of the possible results. They can be directly tracked by using a large number of simulated photons. The accuracy of the result depends only on the number of used photons N, since the statistical error is proportional to $1/\sqrt{N}$.

The grid box data from a simulated GESIMA cloud is used to generate the input data for the Monte Carlo radiative transport model GRIMALDI. The entire modelled area is represented by grid boxes, and the conditions inside each individual box are homogeneous. Each box is fully described by position, geometrical extension, extinction coefficient, single scattering albedo and effective phase function (Rayleigh and Mie scattering). *Macke et al.* [1999] gives an overview of the underlying Monte Carlo radiative transfer calculations. A detailed description of the implemented algorithms and the usage of the program can be found in [*Scheirer* 2001] and [*Scheirer* 2002]. The model takes the interaction between radiation and atmospheric gases, cloud liquid water and water droplets, as well as ice crystals into account. The density of different gases such as water vapor, carbon dioxide and oxygen (the relevant gas for this study) vary with changing altitude. In fact, they also vary in horizontal direction, even if homogeneous in the initial state. This is caused by the dynamics in the model itself.

The angle of the incident photons can be chosen to be either random or fixed. In the random case, new azimuth and zenith angles are calculated for each incoming photon. In the other case, the azimuth and zenith angles are calculated from the sun's position relative to the model cloud and the cloud's orientation. These parameters can either be input directly by the user, or calculated from the

geographical position and local time.

For line by line calculations of absorption due to atmospheric gases, the effective molecular absorption coefficients for a given pressure and temperature are required. These data are taken from the HITRAN database [*Rothman et al.* 2003]. For the model-retrieval comparison the modified spectroscopic data from HITRAN are used in order to insure, that the Monte Carlo simulation and the analysis program have the same underlying spectroscopic data set. The pressure and temperature dependency of the line shapes caused by doppler and collision broadening, also have to be taken into account. This is achieved by using a Voigt profile to describe the line shape. The different line shapes are discussed in detail in section 3.4.2. For simplicity the Fraunhofer lines are ignored.

The Monte Carlo calculations for each individual photon are performed in several consecutive steps. First, the point where the photon interacts with molecules has to be determined. Therefore an 'available extinction' $\epsilon = \ln$ (r) with the random number $0 < r < 1$ is assigned to each photon. The point of interaction is attained, when the sum of all local extinctions along the photon path is equal ϵ.

In the next step, the type of interaction event is determined. In the scattering case, the direction of the photon is changed, while in the absorption case, the tracked photon vanishes. To reduce CPU runtime, single photons are treated in bunches. The photon number in each bunch is parameterized by a weighting factor between 0 and 1. In the case of interaction, each bunch is partially scattered and partially absorbed and a new weight assigned to represent the number of photons remaining in the bunch.

In the last step, the scattering direction of the photons must be determined. Therefore, an effective phase function is assigned to each grid box in the model to describe the zenithal change in photon direction. This phase function is calculated from Mie-theory (spherical cloud droplets) and from ray tracing simulations (non-spherical rain drops and ice crystals), and stored in a lookup table. to determine the scattering direction of a photon, a random number is generated for the change in azimuthal direction, and the grid box's phase function is used to calculate the deflection in zenithal direction.

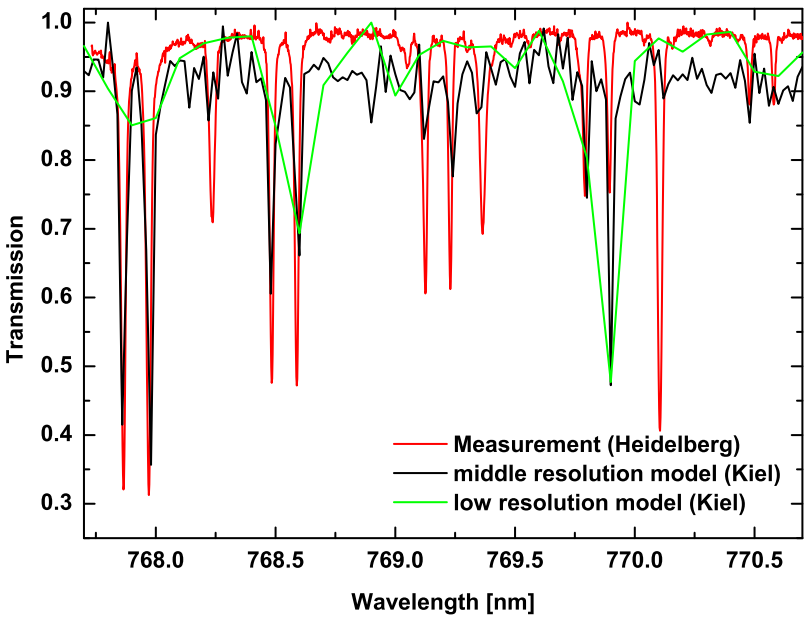

Figure 4.11: *Comparison of Monte Carlo simulations using different model resolutions (green 0.1 nm, black 0.02 nm) and a measured oxygen A-band spectrum (red). These model resolutions are not suited to reproduce the measurement spectrum in detail.*

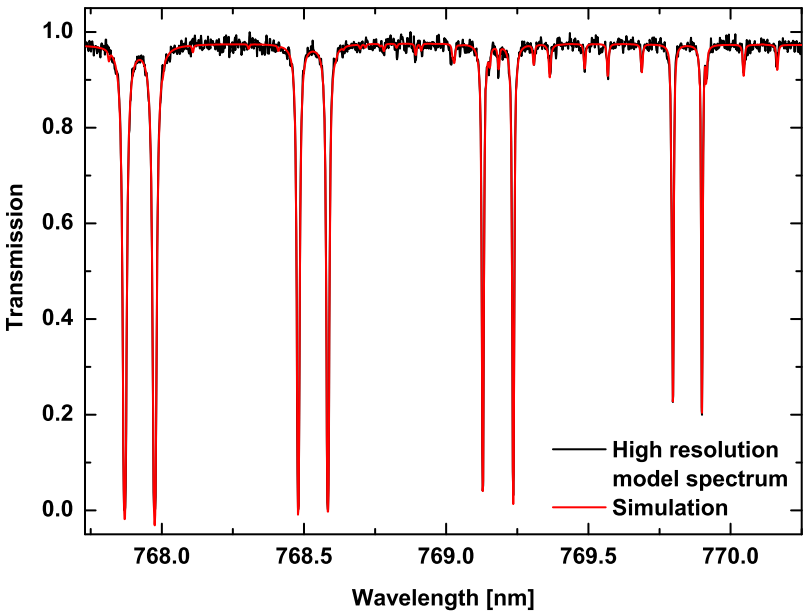

Figure 4.12: *High resolution model spectrum (0.002 nm resolution). The black line represents the model spectrum, while the red line represents the spectrum calculated in the path length distribution evaluation procedure*

4.5.3 Validation Of The Modelled Oxygen A-Band Spectrum

The model cloud, used for the validation study consists of only liquid water (no ice phase) and is 70 minutes old. Figure 4.10 shows the modelled GESIMA cloud. The Monte Carlo simulation of photon path lengths is used in a back calculation mode. This means that, technically the virtual photons are emitted vertically out of the detector. The simulated detector area is 9 cm^2 and is situated at ground elevation in the middle of the observed model area (50km, 50km). A solar zenith angle of 30° and hence a resulting air mass factor of AMF = 1.15 is used in all simulations. 1^{10} photons are simulated, which is a suitable number for the Monte Carlo simulation. When looking in zenithal direction, the model cloud has an optical depth of $\tau_c = 19.63$ or $\tau_c^* = 2.94$ directly over the detector.

Different model runs with different spectral resolutions were performed to find a reasonable compromise between model resolution and CPU runtime. Figure 4.11 shows the results of the first calculations. It is obvious that neither the low resolution of 0.1 nm (green spectrum in fig. 4.11) nor the middle resolution of 0.02 nm (black spectrum in fig. 4.11) could reproduce all spectral features of the simulated high resolution oxygen A-band spectrum (red spectrum in fig. 4.11). It is therefore impossible to obtain reasonable path length distributions using such low resolutions. Although the runtime is too long for many application such as forecast models or the postprocessing of data sets of entire measurement campaigns, a model resolution of 0.002 nm is necessary to correctly describe the absorption spectrum.

Figure 4.12 shows the high resolution model absorption spectrum (black) calculated by the Monte Carlo model. This spectrum is subsequently analyzed to determine the theoretical path length distribution. The spectrum calculated by the path length retrieval is shown in red and agrees well. The difference of the two spectra, the residual, is shown in figure 4.13, and no residual spectral features can be seen. The obtained results show the high potential of the cloud model and the radiative transfer model.

The photon path length through the atmosphere as determined by the GRIMALDI Monte Carlo simulation is given in kilometers, while the path length evaluation algorithm uses VOD. To compare both retrieved mean path lengths, the $\langle l_{tot} \rangle$ obtained from the cloud model is recalculated in kilometers. For this the scale height for molecule oxygen is required. The pressure at a given altitude is given by the weight of the gas above. At sea level, the pressure p_0 is 1013 hPa:= 1atm (at 25°C. Assuming constant temperature throughout the atmosphere, the pressure is a

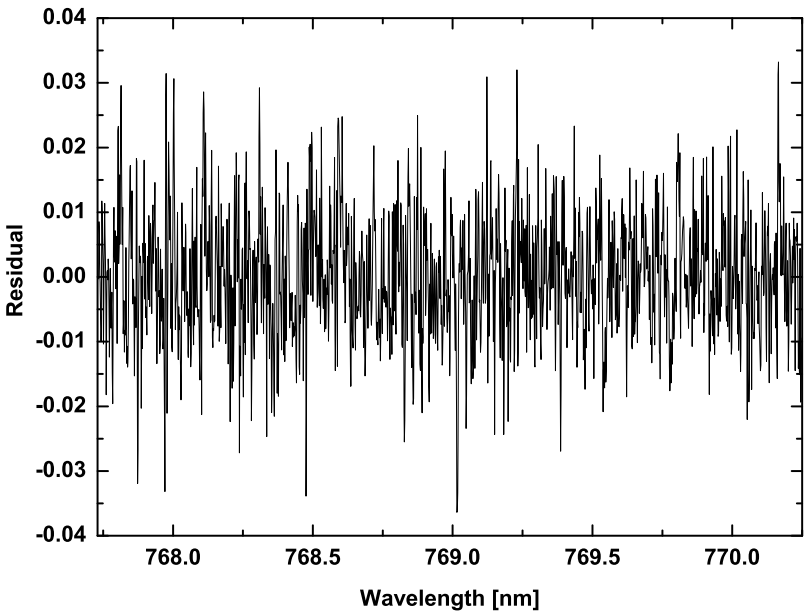

Figure 4.13: *Residual structure: difference of the calculated Monte Carlo spectrum and the calculated evaluation spectrum*

function of altitude and can be written as (the barometric formula): $p(z) = p_0 \cdot e^{-\frac{z}{z_0}}$. The scale height z_0 is given by:

$$z_0 = \frac{k \cdot T}{m \cdot g} \tag{4.15}$$

For molecular oxygen the scale height is 7480 m. This height corresponds to one VOD. Using this scale height, the mean path length retrieved by the path length retrieval algorithm is 11.67 km. The Monte Carlo simulation resulted in a mean path length of 11.8 km. Therefore, the values are in very good agreement with one another. For the examined model in the simulation $1.7 \cdot 10^6$ photons reached the detector. Figure 4.14 shows the retrieved photon path length distributions when using the high resolution model spectrum as input.
Compared to the mean photon path lengths, which agree very good, the widths of both distributions vary stronger. The distribution calculated by the MC simulation is narrower than the distribution obtained from the retrieval algorithm. Therefore the probability for the mean photon path length is higher than in the retrieval algorithm, as both distributions are normalized. The reason for the different widths of the distributions could be the calculation of the photon PDF in the MC model. The spectrum is calculated line-by-line (beginning at 767.4 nm in 0.002 nm steps).

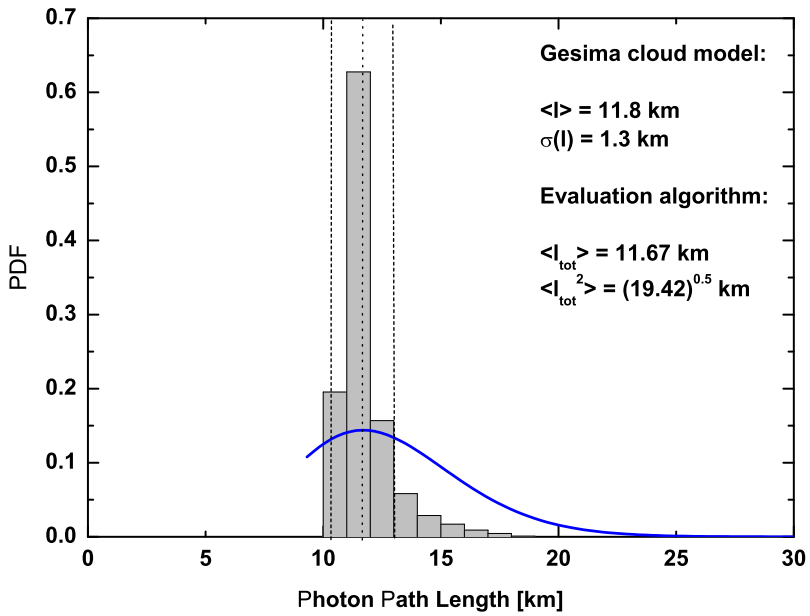

Figure 4.14: *Comparison of the photon path length distribution using the Monte Carlo simulation (grey bars) and the cloud model evaluation program (blue line). Both distributions are normalized to 1.*

For each line, a photon PDF is obtained. Finally all PDFs are summed up and renormalized. This could lead to an underestimation of larger photon paths in the MC radiative transfer model. The implementation of a better photon PDF calculation method in the MC model is still a subject of the ongoing investigation.

Chapter 5

Results

The presented measurements of the photon path length distributions are performed using the grating spectrometer system described in section 4.1. In comparison to former studies [*Funk* 1996; *Greiner* 1998; *Veitel* 1997] the improved instrumental setup allows integration times of less than 5 sec, depending on the brightness of the cloudy sky. Typical integration times are about 2 seconds. The spectra are co-added to 1 minute intervals to obtain a reasonable signal-to-noise ratio. The integration time and the speed of the clouds determine a scale, over which a spatial averaging is done. The time integration, corresponding to an intensity-weighted average, assumes that the cloud structure changes slowly. Photon diffusion inside the cloud leads to a spatial averaging, depending on the degree of inhomogeneity, e.g. for a single layered homogeneous cloud layer the mean lateral displacement of the photons in transmission is equal to the cloud thickness.
This chapter presents results measured during two international cloud campaigns in Cabauw/Netherlands.

5.1 The 4D Cloud Project

In 2001 and 2003 two large field experiments are conducted around the central meteorological measurement facility of the Dutch Meteorological Service at Cabauw (51°58.2' N, 4°55.6' E), the Netherlands. This facility is part of a regional network consisting of ten remote sensing stations covering a region of 100 by 100 km^2 in the central Netherlands.
Both field experiments are carried out in the framework of BALTEX (Baltic Sea Experiment). BBC1 (First BALTEX BRIDGE Campaign) lasted from August till September 2001. During the first four weeks a Microwave Intercomparison Campaign (MICAM) took place in which seven to ten microwave radiometers from

all over Europe performed simultaneous measurements. In September the rest of the cloud remote sensing instruments, like the oxygen A-Band spectrometer, started measurements. The BBC2 (Second BALTEX BRIDGE Campaign) was performed in May 2003. The focus of both BBCs is experimental research in the cloudy continental troposphere.

Both BBCs are funded from many national and international projects and organisations. Besides KNMI and CLIWA-Net (Cloud Liquid Water Network, a Fifth Framework European Commission project), the 4DClouds project is significantly involved in the organization and realization of the experiments. This study is performed within the framework of this project, which is part of the German AFO2000 (Atmosphärenprogramm 2000) research programme. Main topics of this project are the evaluation of the spatial variability of clouds in three spatial dimensions and the analysis of three-dimensional effects in cloud radiative transfer. These measurements should contribute to the development of cloud parameterizations in weather and climate models. Important contributions also came from Meteo France, the MetOffice UK and the military of the Netherlands.

5.2 Case Studies

5.2.1 BBC1 Campaign September 2001

To study the inner structure of the clouds three cloud radars operating at different frequencies are available, the 3GHz radar TARA operated by TU Delft, the permanently installed 35 GHz radar operated by KNMI and the 95 GHz radar MIRACLE from the Institute for Coastel Research at the GKSS Reserach Center [*Quante et al.* 2000; *Donovan et al.* 2001]. All three radar systems performed simultaneous zenith and sky scanning measurements. In this study measurements from the two latter cloud radars are used. During the first BBC campaign the liquid water path (LWP) was measured by the 22 channel microwave radiometer MICCY (MIcrowave radiometer for Cloud CarthographY) from the University of Bonn [*Crewell et al.* 2001]. In combination with the radar it allowed a quantitative estimate of cloud liquid water profiles. Backscatter lidars and lidar-ceilometers (CT75 K ceilometer (KNMI), LD40 ceilometer (KNMI), CT25 K ceilometer (U Bonn)) accurately determined the development of the cloud base. Three aircrafts (Merlin IV (Meteo France), Partenavia (IfT Leipzig), Cessna C2007 T (FU Berlin)) measured during coordinated flights in-situ cloud microphysical parameters and radiation below, inside and on top of the clouds. A tethered balloon (MAPSY (IfT Leipzig,

German Army)) equipped with measuring instruments for cloud microphysics and radiation sensors was used to take vertical and horizontal profiles through the clouds. Periodically radiosonde ascents (KNMI, Dutch Army), a multitude of ground based standard meteorological sensors including radiation measurements and the 200 meter meteorological tower completed the intense and detailed measurements of the cloudy sky properties. A brief overview of used instruments and some selected results from all participating groups can be found in *Crewell et al.* [2004].
For the first campaign two selected time periods on two days are presented.

September 18, 2001

The radar image in the upper panel of Figure 5.1 shows the cloud situation between UT 15:18 and UT 16:24. Due to a malfunction no cloud radar measurements are available for the time between UT 15:49 and UT 15:50. The cloud situation is characterized by an altostratus cloud deck with embedded cumulus clouds coursing some precipitation. The rain drops did not reach ground, but led to a strong reflectivity signal, due to the large droplet size. The interpretation of cloud radar images has to be carried out carefully, since the backscatter signal depends on the particle diameter D to the power of sixth (D^6). Therefore a cloud radar is less sensitive to small droplets. During the observed period the cloud top height increases from 5000 m to 6000 m, while cloud base decreases from 2000 m at the beginning of the presented measurements to 800 m at the end. This is a total geometrical cloud thickness ΔH of 4000 m to 5200 m. The wind speed during the observed period is 20 m/s measured by a radiosonde in 4000 m altitude. To be under the spatial scale of radiative smoothing η_T (see section 3.1.4 the integration time must be under 200 s to 260 s, respectively. For the observed period the integration time of 60 s is below this limit.

In the lower panel of Figure 5.1 the first and the second moment of the photon PDF ($\langle L_{tot} \rangle$ and $\sqrt{\langle L_{tot}^2 \rangle}$) in VOD units of the oxygen atmospheric column are plotted on the left ordinate-axis. The liquid water path derived from simultaneous MICCY measurements is shown on the right ordinate-axis. The black dashed line shows the photon path lengths for the direct sunlight. For the whole time period the mean photon path length is significantly larger than the direct sunlight path length[1].

Figure 5.2 shows the cloud situation over the Netherlands on September 18,

[1]The cloud radar image and the graph showing the measured quantities are arranged in a way, that the time axes coincide exactly. This is done for all measurements presented in this study. So it is possible to compare directly the vertical cloud structure with the measured moments of the photon path and the inferred liquid water path.

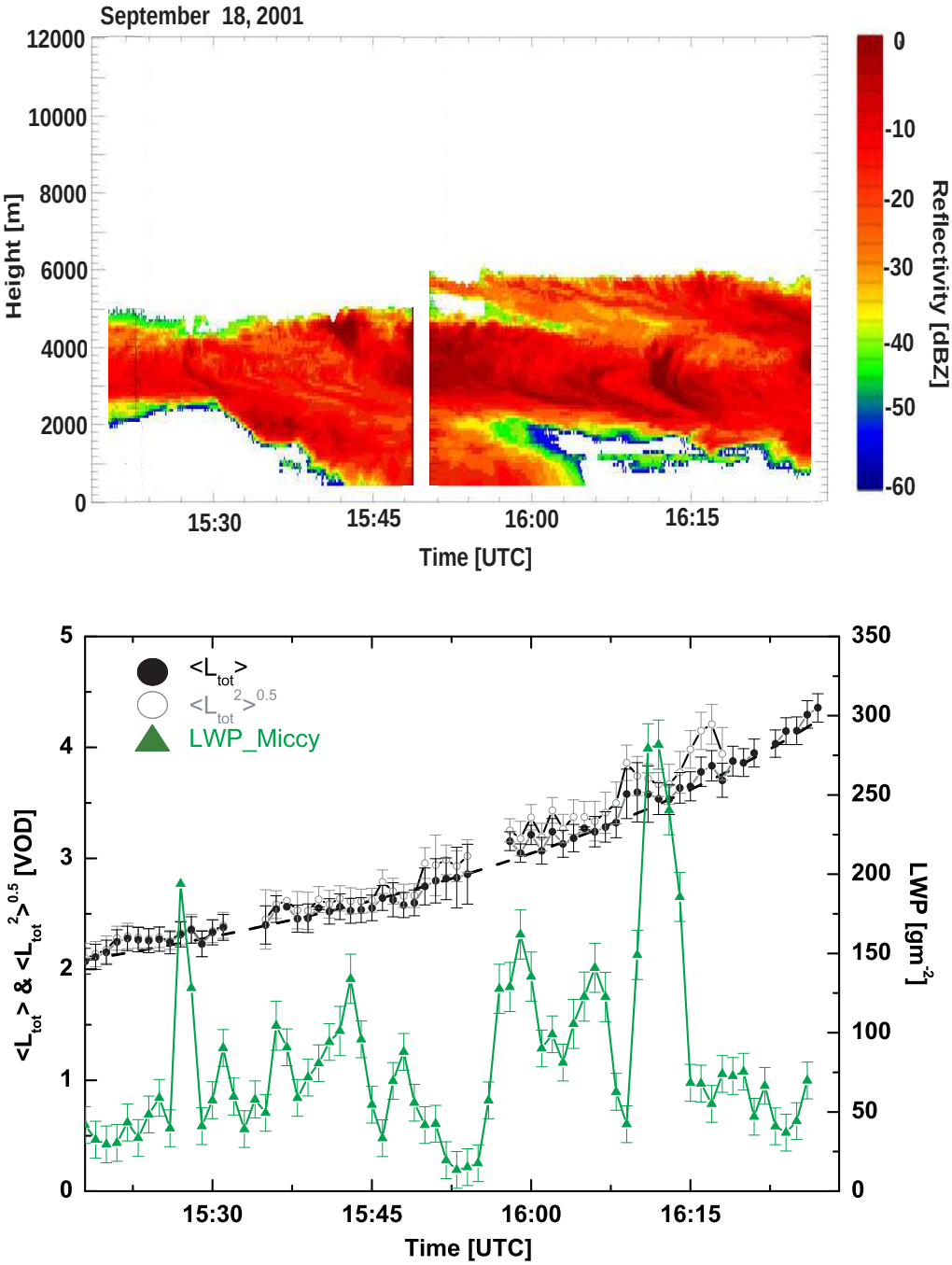

Figure 5.1: *Upper panel: Radar reflectivity measured by the by the GKSS 95 GHz Radar at Cabauw (NL) on September 18, 2001 between UT 15:18 and UT 16:24. Lower panel: Time series of inferred first two moments of the photon paths ($\langle L_{tot} \rangle$ and $\sqrt{\langle L_{tot}^2 \rangle}$) in VOD units of the oxygen atmospheric column (left ordinate-axis) and liquid water path (LWP, right ordinate-axis) measured by MICCY. The black dashed line shows the photon path lengths for direct sunlight 1/cos(SZA).*

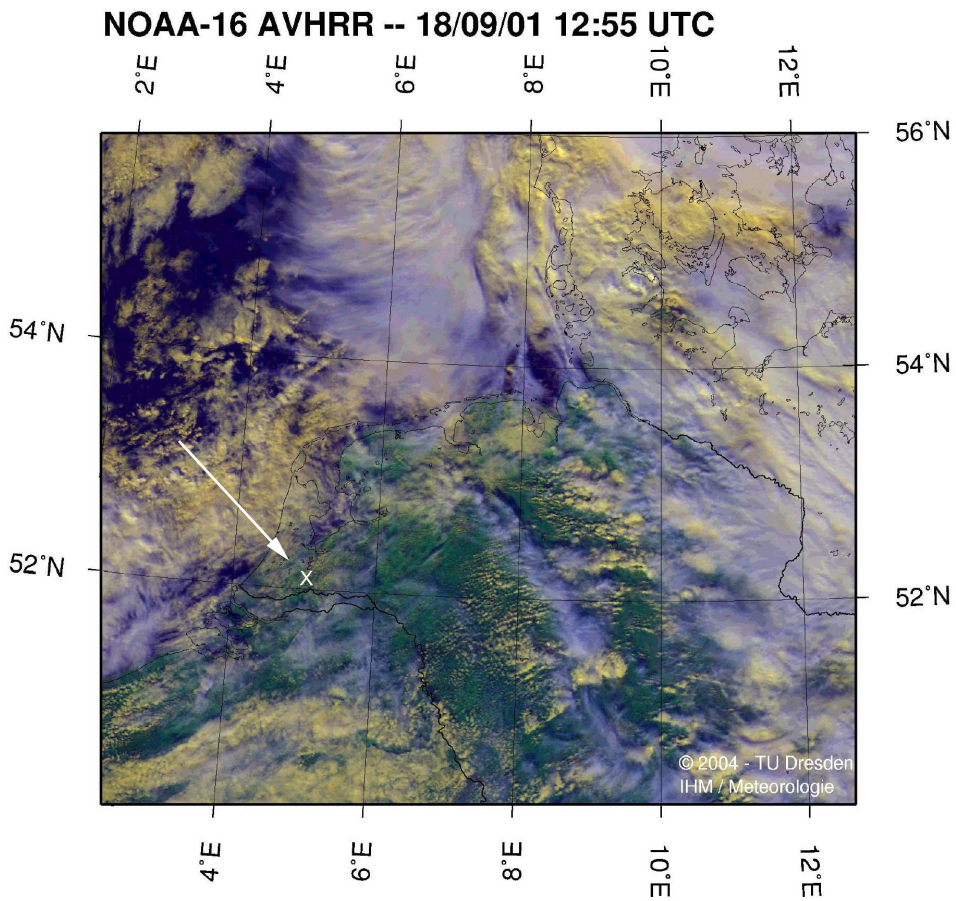

Figure 5.2: *NOAA-AVHRR Satellite Image of Central Europe for September 18, 2001. The cloud top temperature is color coded, ranging from white (cold high clouds) to ochre (warm low clouds).*

2001 at 12:55 UTC. The image is taken from the NOAA-16 satellite operational since early 2001. One of the main instruments onboard the satelitte is the AVHRR (Advanced Very High Resolution Radiometer) for observation of cloud-, land- and sea- surface at 1 km resolution. It measures in the visible and infrared wavelength regions (cloud observations at 0.58-0.68 μm and 1.58 -1.68 μm). For all presented measurement in this study, satellite images of the cloudiness taken with the AVHRR instrument are available. The temperature at cloud top is color coded. White and blue correspond to colder high clouds, while ochre stands for warmer lower clouds.

In chapter 3 an overview of the theory of anomalous diffusion of photons in dense media, especially clouds is given. To validate the modified equation 3.18,

the mean photon path length inside the cloud $\langle L_c \rangle$ is inferred from the total mean path length $\langle L_{tot} \rangle$ according to section 3.9.1. The in-cloud mean path length is given in units of the vertical cloud extension ΔH. Therefore the ΔH term is expressed in air mass units. $\langle L_c \rangle / \Delta H$ is plotted as a function of the rescaled optical depth τ_c^* (equation 3.10). For the calculation of τ_c^* from measured LWP and ΔH an asymmetry value g of 0.85 is assumed and a constant effective radius of $r_e = 8$ μm ($\pm$ 1 μm) is taken. The latter value is inferred from tethered balloon r_e-measurements up to 1500 m altitude [*Schmidt et al.* 2004; *Crewell et al.* 2004]. Figure 5.3 shows the retrieved $\langle L_c \rangle (\tau_c^*)$ values and the theoretically predicted values from classical and anomalous photon diffusion theory (black lines). The theoretical values for the classical diffusion case ($\alpha = 2$) are directly calculated from equation 3.18. For the anomalous diffusion case ($1 < \alpha < 2$) the right hand side of equation 3.18 is simply taken to the power of ($\alpha - 1$). The cloud cover studied over the almost one hour long period demonstrate, that the Lévy index α is between 1.6 and 2 for this altostratus cloud cover.
A rough classification of the different cloud types can be done based on the different heights in which the clouds normally appear. In the lowest layer (0 to 2 km), clouds normally consist of liquid water. Typical clouds are stratus and stratocumulus clouds. In the middle layer, between 0.5 and 9 km, clouds are a mixture between supercooled water and ice. Typical clouds are altocumulus and altostratus clouds. In the top layer (5 - 13 km), almost only ice clouds appear, namely cirrus and cirrostratus clouds.

Additionally the ratio of the square root of the second moment and the mean photon path $\langle \sqrt{L_c^2} \rangle / \langle L_c \rangle$ is calculated and compared with the theoretical prediction of equation 3.20. Figure 5.4 shows the measured ratios for the inferred first two moments and the prediction based on the classical diffusion theory. The results provide evidence, that the numerical value of the exponents and prefactors of the generalized expression for the first and second moment is reasonably accurate in the anomalous diffusion regime.

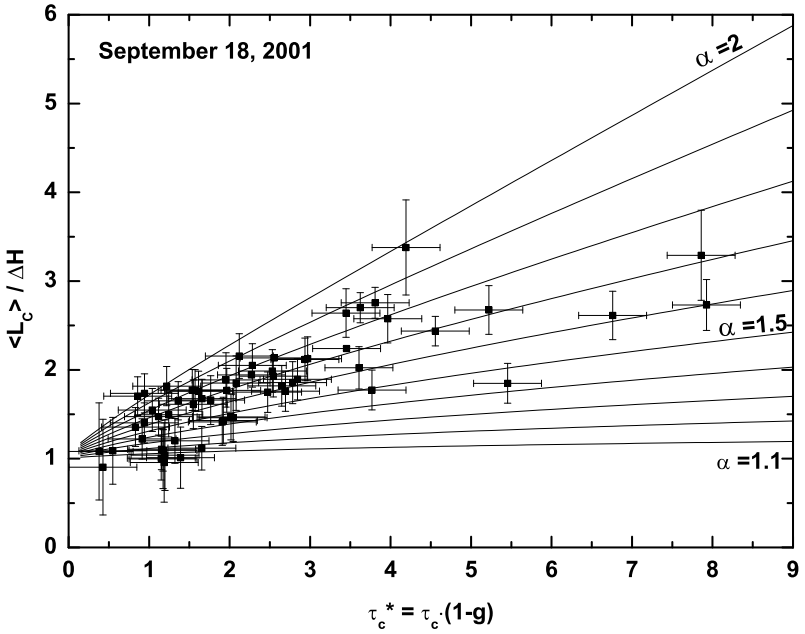

Figure 5.3: *Mean cloud photon paths* $\langle L_c \rangle$ *as a function of effective cloud optical depth* τ_c^* *for September 18, 2001. The black lines are predictions for different values of the Lévy exponent* $\alpha \leq 2$.

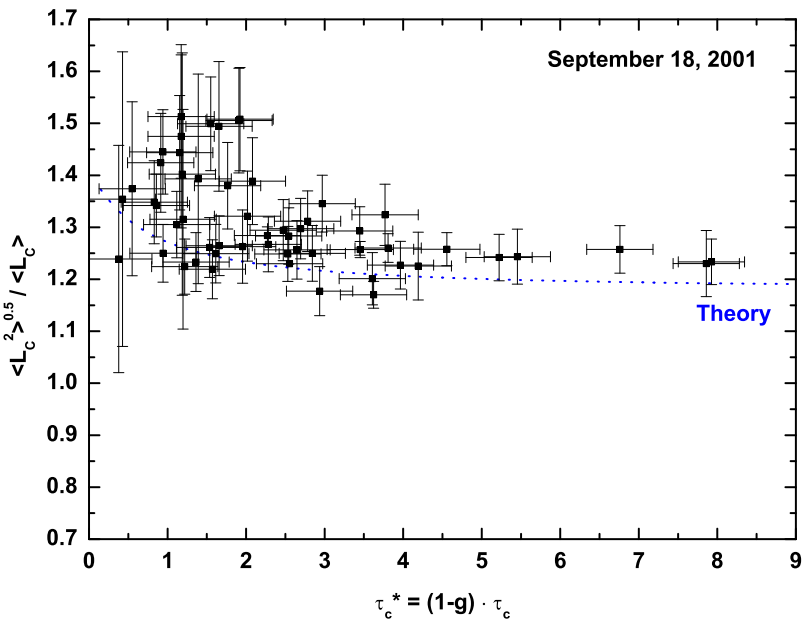

Figure 5.4: *Measured ratio of the first and second moment* ($\langle L_c \rangle$ *and* $\sqrt{\langle L_c^2 \rangle}$) *for September 18, 2001. The predicted ratio, based on the classical diffusion theory, is indicated by the dashed blue line.*

September 23, 2001

On September 23, 2001 the cloud scene is dominated by single layered cumuli clouds. The upper panel of figure 5.6 shows the cloud radar images measured by the 95 GHz cloud radar MIRACLE from UT 11:52 to UT 12:48. During the presented period cloud top varies between 1200 m and 1400 m. To determine the cloud base, KNMI ceilometer data are used (red dots). The high reflectivity signal below the cloud base is due to insects, since their large size induces a large backscatter signal.

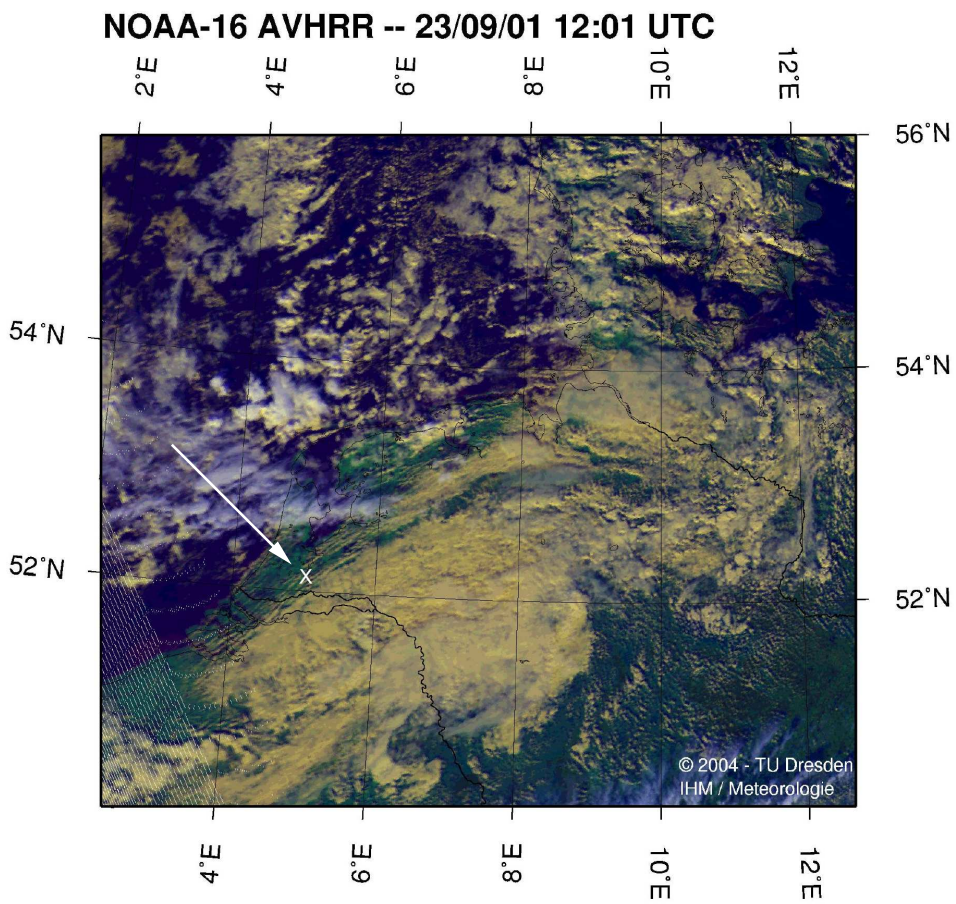

Figure 5.5: *NOAA-AVHRR Satellite Image of Central Europe for September 23, 2001*

In the lower panel of figure 5.6 the measured moments of the photon path length and the measured liquid water path are shown. Again, the dotted line indicates the light path for direct sun observations. It can be seen, that the values for the mean photon path are two times (UT 12:15 and UT 12:40) equal to the direct sun light

path. This indicates, that no clouds are in the field of view of the oxygen A-band spectrometer, which is approved by the cloud radar measurements. The retrieved total path lengths are between 1.7 and 1.95 VODs.

The satellite image shows a large low cloud cover south of the measurement site indicated by the white cross in figure 5.5, while high cirrus clouds are in the north. The measurement site lies below the outer edge of the cloud cover leading to a broken cloud cover, as seen in the cloud radar.

In figure 5.7 the in-cloud mean photon path length in units of ΔH is plotted against the rescaled cloud optical depth. Most of the data for this time period indicate a Lévy index smaller than 2, indicating anomalous diffusion.For the presented single layer broken cloud cover a value of α between 1.6 and 2 is determined.
The ratio of the square-root of the second moment and the mean moment of the retrieved path length distribution for the presented time period is plotted in figure 5.8 against the retrieved cloud optical depth. Again the theoretical prediction is plotted as a blue line. For rescaled cloud optical depths smaller than 6 the measured ratio is smaller than the predicted value of 1.18.

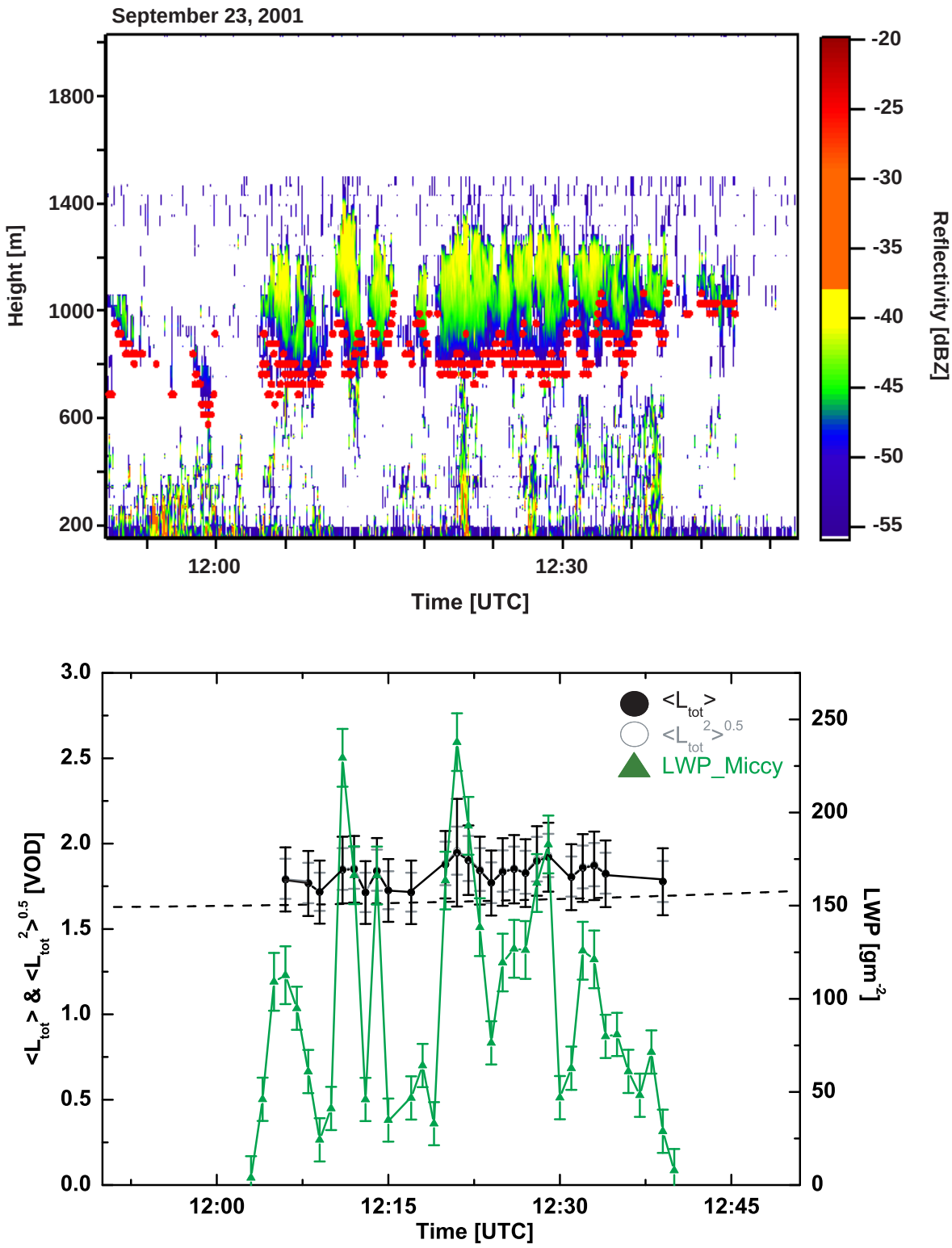

Figure 5.6: *Upper panel: Radar reflectivity measured by the GKSS 95 GHz Radar at Cabauw (NL) on September 23, 2001 between UT 11:52 and UT 12:48. The red dots indicate the cloud bottom measured from the KNMI ceilometer. Lower panel: Time series of inferred first two moments of the photon paths ($\langle L_{tot} \rangle$ and $\sqrt{\langle L_{tot}^2 \rangle}$) in VOD units of the oxygen atmospheric column (left ordinate-axis) and liquid water path (LWP, right ordinate-axis) measured by MICCY. The dashed black line shows the photon path lengths for direct sunlight.*

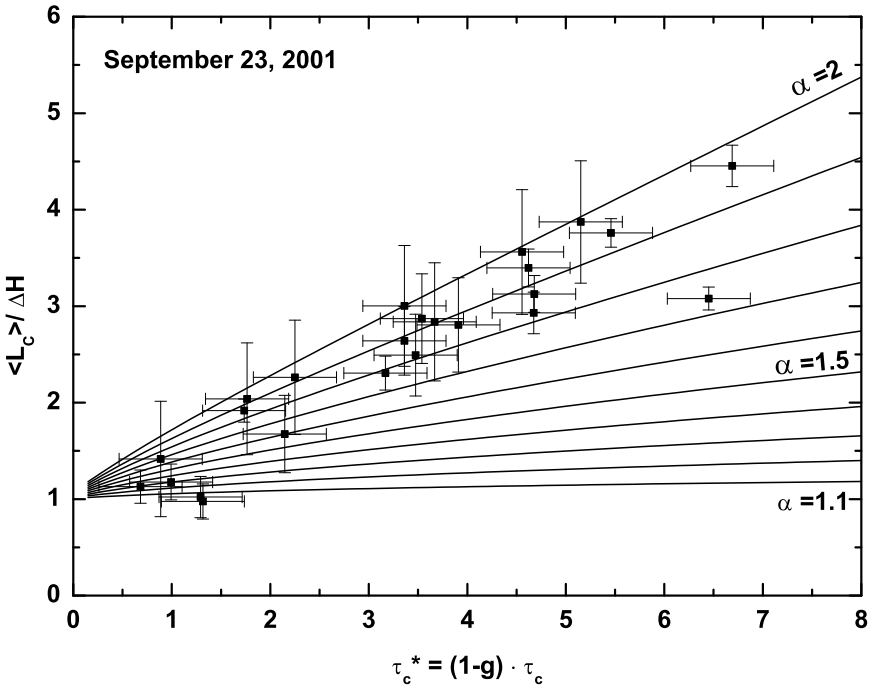

Figure 5.7: *Mean cloud photon paths* $\langle L_c \rangle$ *as a function of effective cloud optical depth* τ_c^* *for September 23, 2001. The black lines are predictions for different values of the Lévy exponent* $\alpha \leq 2$.

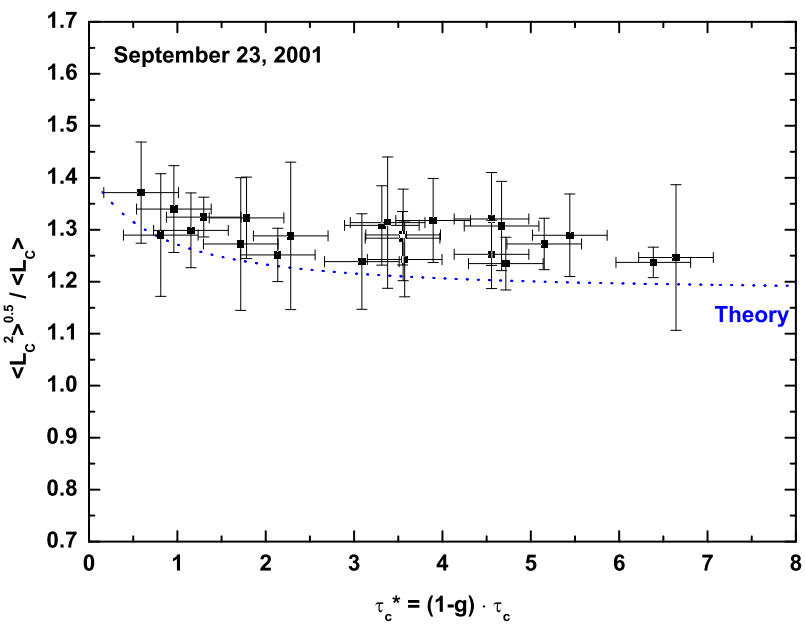

Figure 5.8: *Measured ratio of first and second moment(*$\langle L_c \rangle$ *and* $\sqrt{\langle L_c^2 \rangle}$*) for September 23, 2001. The predicited ratio, based on the classical diffusion theory, is indicated by the dotted blue line.*

5.2.2 BBC2 Campaign May 2003

Due to bad weather during the first BBC campaign a second one, namely BBC2, was carried out during May 2003 in Cabauw/Netherlands. In comparison to the BBC1 campaign it was possible to examine more days and more different cloud types. In this section four different days will be discussed in detail.

A short time period of 45 minutes, measured on May the 8th, is discussed. Total day time series are available for the 11th and 22nd of May, 2003. Additional four hours of measurements performed on the evening of May 21 are also discussed.

In addition to the microwave radiometer MICCY, a 'low cost' microwave radiometer system RPG-HATPRO (Humidity And Temperature PROfiler) from Radiometer Physics GmbH (RPG) [*Rose et al.* 2005] was operated. As far as available both cloud liquid water measurements are taken to retrieve the rescaled cloud optical depth (see equation 3.10). To determine the geometrical vertical structure, the radar measurements from the 95 GHz cloud radar MIRACLE from the GKSS Research Center and additionally from the 35 GHz cloud radar operated by KNMI are used. For all days, except for May 8, cloud camera images observing the area of measurement are available.

May 8, 2003

A cold front crosses the Netherlands during the night and the morning of May 8. High clouds associated with this front moves over the northern part of the Netherlands. In the southern part of the Netherlands, scattered thin cirrus clouds associated with a warm front approach. During the second half of the day a rain front spread out over the central part of the country. This front reaches the measurement site around UT 15:30.

The cloud radar image (upper panel of figure 5.10) shows the existing cloud situation. At the beginning of the observed period strong convective cells leading to cumuli clouds with weak precipitation are present. Starting UT 15:15 these cumuli clouds become more compact and develope a nimbostratus cloud deck leading to heavy rain. The cloud base height is measured by a ceilometer. The blue dots indicate the cloud bottom. This information cannot be provided by cloud radar, as the rain drops cause a strong backscatter signal. For this reason the measurement of geometrical cloud extension is only useful in combined measurements of cloud radar and ceilometer. The cloud height is almost constant over the discussed time

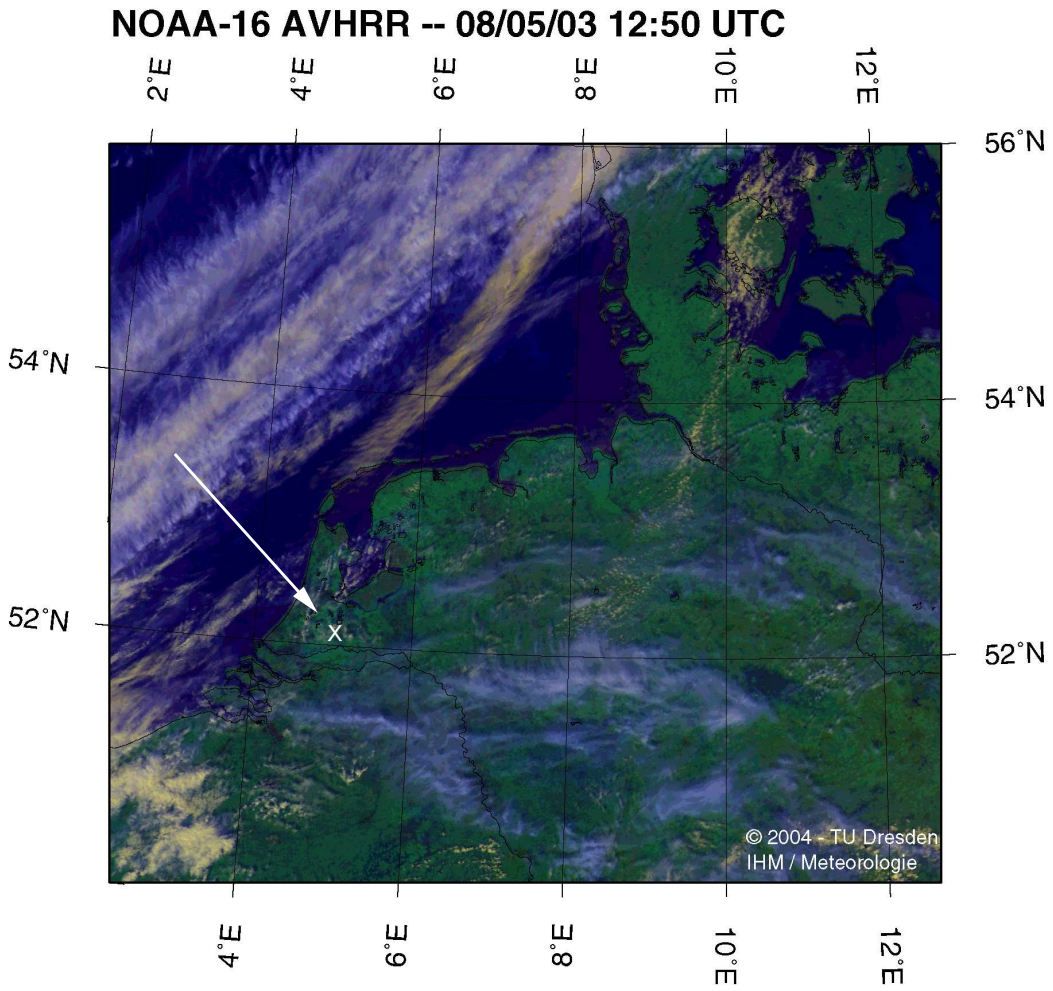

Figure 5.9: *NOAA-AVHRR Satellite Image of Central Europe for the May 8, 2003 observation*

period. From UT 14:30 to UT 15:12 the geometrical extension is 1200 m and afterwards rise up to 3000 m. From UT 15:30 on the rain drops reach ground and measurements stop.

The first and second moment of the photon path length distributions are plotted in the lower panel of figure 5.10. Due to technical and mechanical problems with the microwave radiometer Miccy, the cloud optical depth is calculated using the LWP data from HATPRO. For completeness the retrieved LWP data from Miccy are also plotted. It can be seen that the mean and the variance of the photon path length distribution is parallel to the cloud LWP. This is the expected behavior, since with more liquid water inside the cloud, more particles acting as scattering particles

are available. This results in a longer photon path inside the cloud. The incoming rain front can clearly be seen in the measured mean photon path length data as well as the measured liquid water path data from both microwave radiometers. Beginning at the mentioned time the LWP rise very quickly until UT 15:30, when measurements stop. Simultaneously the measured first and second moment of the photon path length distribution increase due to more available scattering particles. As expected the path lengths are parallel the measured liquid water path, as the path length is proportional to the optical depth and therefore proportional to the cloud liquid water content.

Figure 5.9 shows the satellite image. A huge cloud band is visible in the northwest of the measurement site. From the southwest the mentioned rain clouds approach.

In Figure 5.11 the Lévy index α is between 1.7 and 1.9 for rescaled cloud optical depth $\tau_c^* \geq 4$. These data points correspond to the measurements after UT 15:15. The retrieved values for α for a nimbostratus cloud deck are in very good agreement with the findings from September 18, 2001 with a Lévy index between 1.7 and 2 for an altostratus cloud deck. For smaller rescaled cloud optical depths α varies between 1.2 and 2.

The measured ratio $\langle L_c^2 \rangle^{0.5} / \langle L_c \rangle$ is shown in figure 5.12. For rescaled cloud optical depths larger than 8, all retrieved ratios follow the theoretical prediction. For smaller τ_c^* the retrieved ratios are between 1.1 and 1.6.

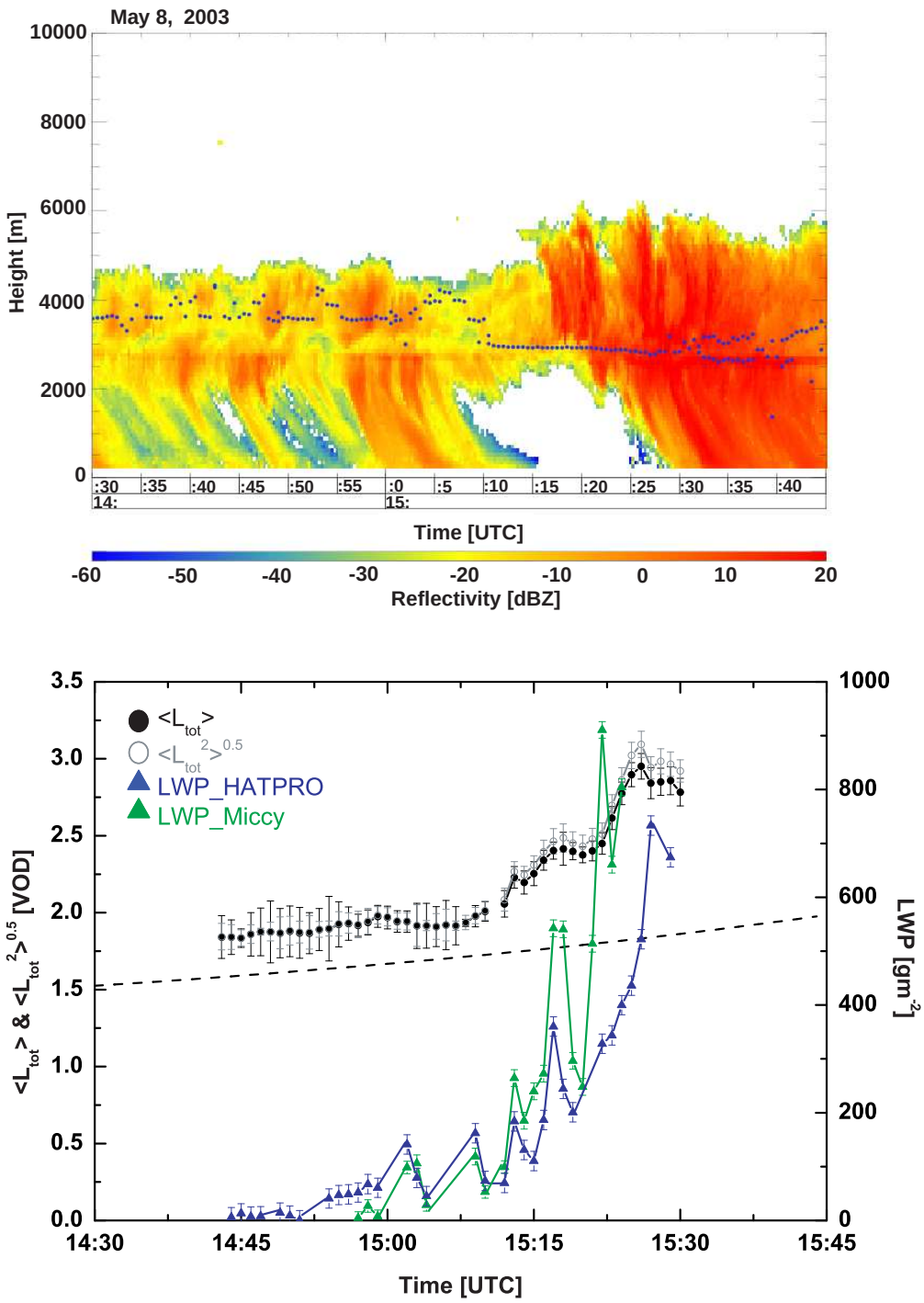

Figure 5.10: *Upper panel: Radar reflectivity measured by the KNMI 35 GHz Radar at Cabauw (NL) on May 8, 2003 between UT 14:43 and UT 15:30. The blue dots indicate the cloud bottom measured from the KNMI ceilometer. Lower panel: Time series of inferred first two moments of the photon paths ($(\langle L_{tot}\rangle$ and $\sqrt{\langle L_{tot}^2\rangle})$) in VOD units of the oxygen atmospheric column (left ordinate-axis) and liquid water path (LWP, right ordinate-axis) measured by MICCY and by HATPRO. The dashed black line shows the photon path lengths for the direct sunlight 1/cos(SZA).*

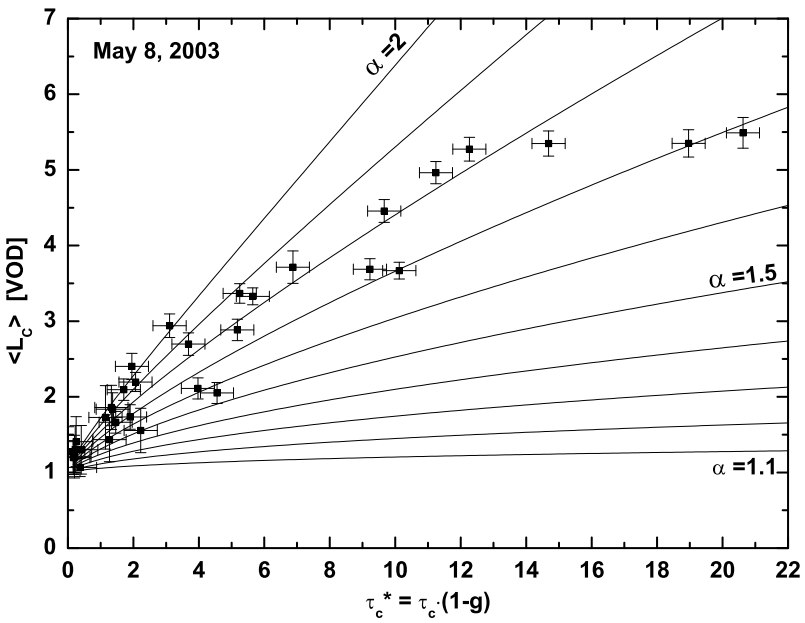

Figure 5.11: *Mean cloud photon paths* $\langle L_c \rangle$ *as a function of effective cloud optical depth* τ_c^* *for May 8, 2003. The black lines are predictions for different values of the Lévy exponent* $\alpha \leq 2$.

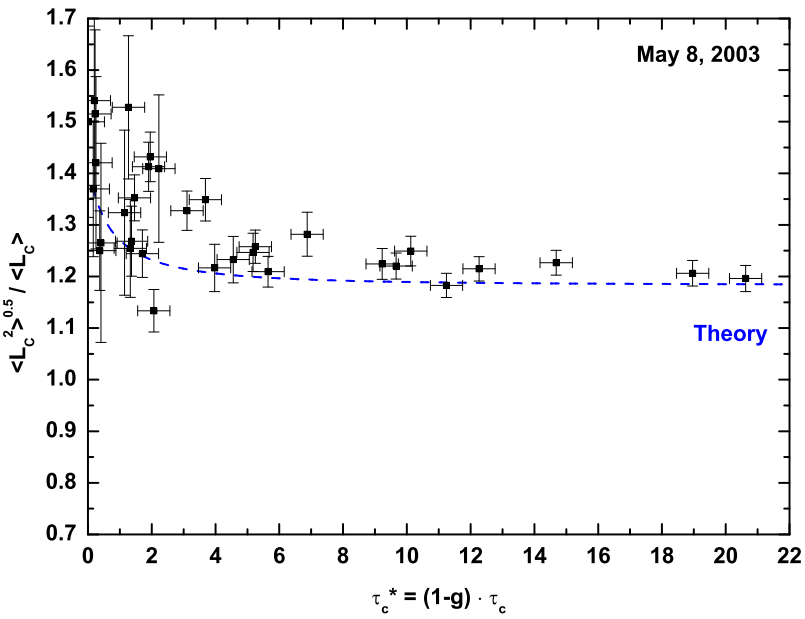

Figure 5.12: *Measured ratio of first and second moment(*$\langle L_c \rangle$ *and* $\sqrt{\langle L_c^2 \rangle}$*) for May 8, 2003 . The predicted ratio, based on the classical diffusion theory, is indicated by the dotted blue line.*

May 11, 2003

The upper panel of figure 5.14 shows the cloud radar image, measured by the 35 GHz KNMI radar. The cloud top height varies between 5500 m and 6000 m. The cloud base height at 2000 m is with some exceptions, almost constant over the whole observed time period. Interestingly the cloud radar could not measure this low cloud base. This can be explained by a second very thin stratus layer with very small droplet sizes, which cannot been seen by the radar. Clouds become optically thick for backscatter ratios larger than -20 dBZ. The backscatter signal in the cloud radar image below 1000 m is again due to insects. For the retrieval of the in-cloud photon path length the combined ceilometer and cloud radar measurements are used, leading to a geometrical cloud thickness ΔH = 3500 m to 4000 m.

In the lower panel of figure 5.14 the retrieved first two moments of the path length distribution and the measured liquid water path are shown. The measurements show that the retrieved photon path length follows nearly the dotted line indicating the direct sun path length values, except at UT 12:00. Starting at UT 16:00 a large cloud system with high liquid water content passes the measurement site, leading to weak precipitation.

Figure 5.15 shows a sequence of sky images[2]. At UT 12:00 a closed cloud cover is visible. The ceilometer measurements give the cloud base height at 1800 m. Also the measured liquid water path increases similar to the retrieved mean photon path length. The cloud radar shows only a weak backscatter signal. Since all other instruments show a clear signal, it can be concluded, that clouds are above the measurement site at this point. The clouds themselves must consist of very small water droplets, as the cloud radar cannot detect them due to sensitivity of the radar to droplet size.

Between UT 13:00 and UT 16:00 all measurements indicate very thin clouds. The measured liquid water path is low and also the measured path length is slightly larger than the direct sun light path. The images and the ceilometer measurements show a patchy cloud structure. After UT 16:00 optically thicker clouds cross the measurement site. The liquid water path and the mean photon path length increase. The cloud drop size increases, as the cloud base height measured by the cloud radar is now equal to the ceilometer measurements.

[2] The camera is a commercial observation camera equipped with a 120° camera lens. The images are continuously recorded and for nearly all days available. To illustrate the cloud situation over the measurement site and to show the clouds corresponding to the presented measurements, cloud images for every full hour are shown.

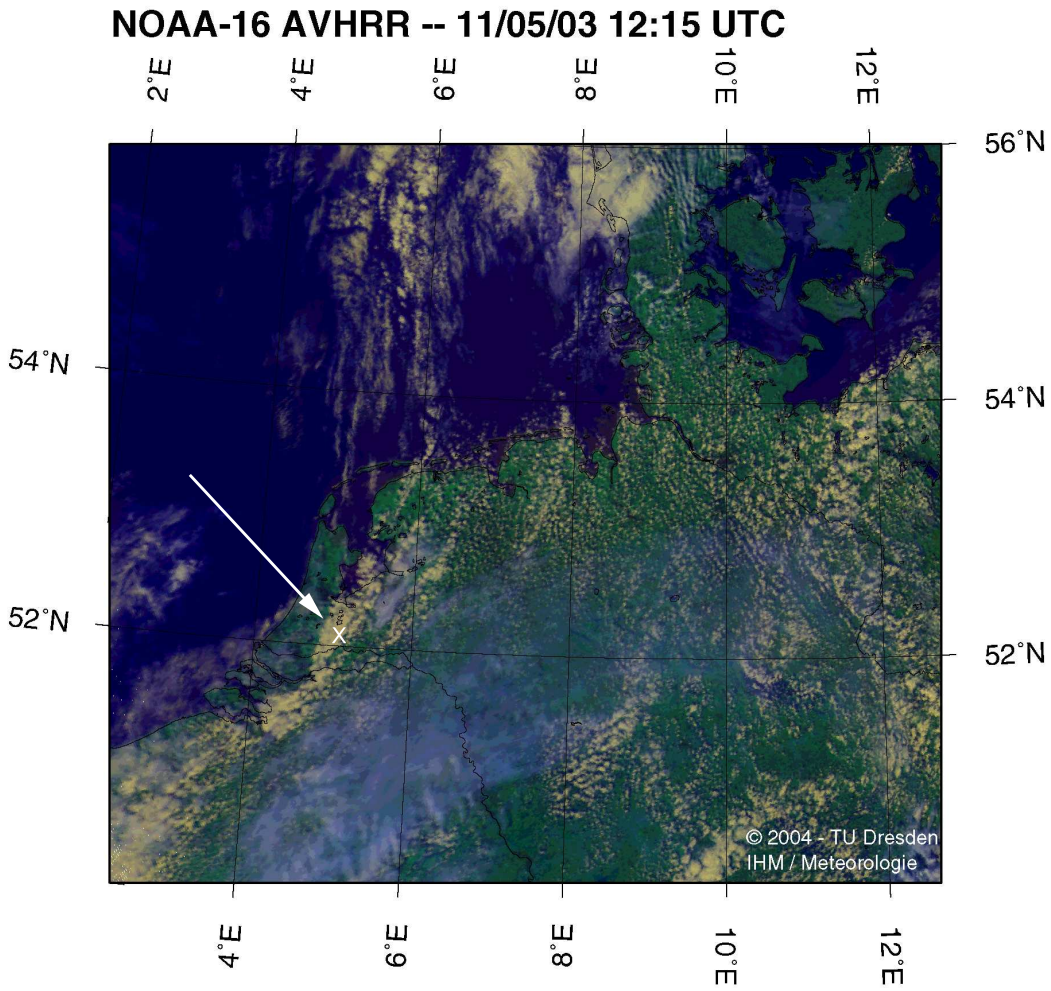

Figure 5.13: *NOAA-AVHRR Satellite Image of Central Europe for the May 11, 2003 observation*

This special cloud situation for this day can also be seen in the Lévyplot (figure 5.16) and the ratio of the second and first moment of the photon path length distribution (figure 5.17). For small rescaled cloud optical depths ($\tau_c^* < 6$) a Lévy index smaller than 1.5 is found. The behavior of the measured photon path length is as expected. For optical thin clouds the mean path length should be comparable to the direct path. As it can be seen in the lower panel of figure 5.14 measured path length and path length for direct sun match exactly for the most observations over the day, except for time periods from UT 11:53 to UT 12:30 and UT 16:00 to UT 18:00.

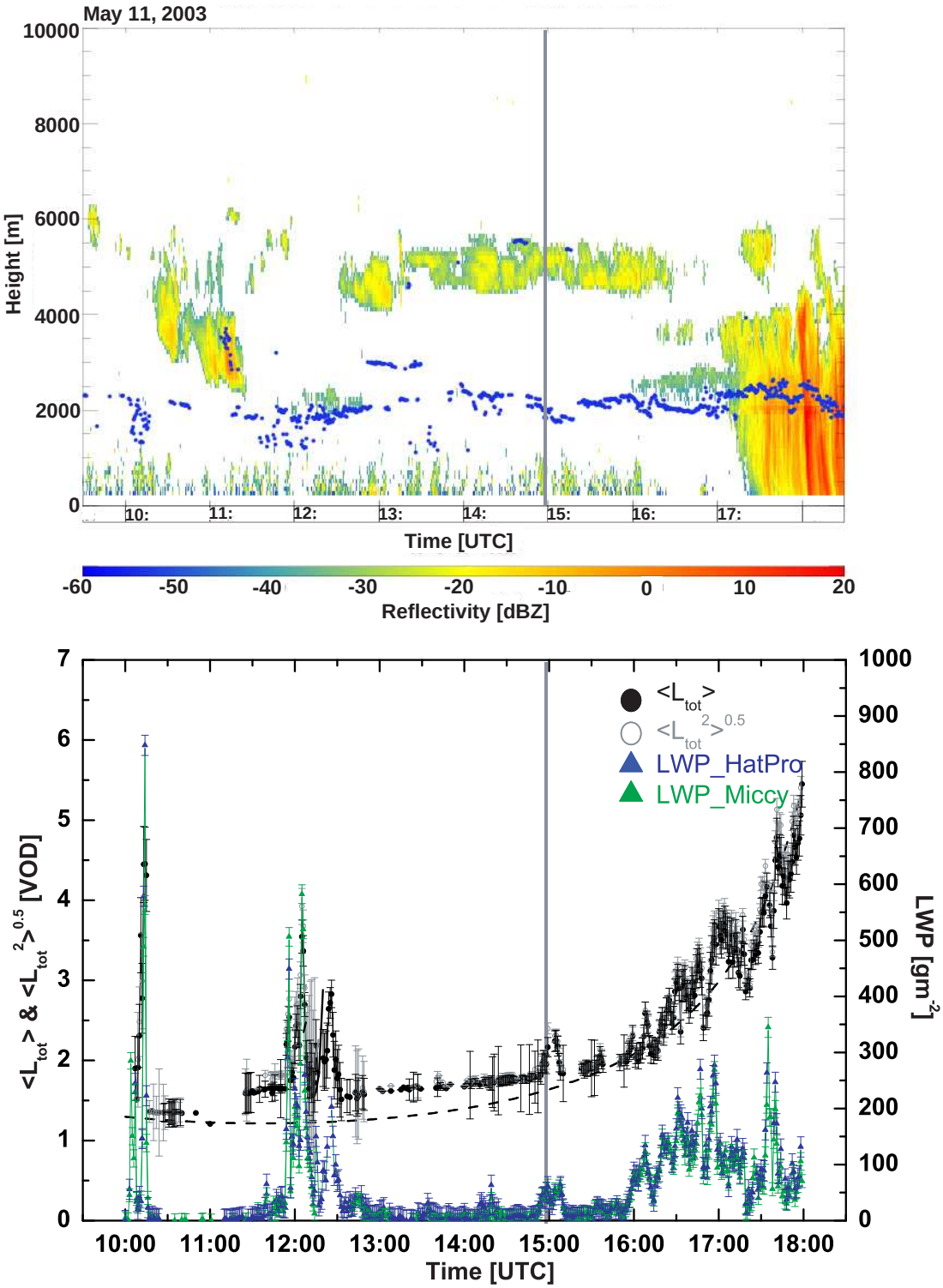

Figure 5.14: *Upper panel: Radar reflectivity measured by the KNMI 35 GHz Radar at Cabauw (NL) on May 11, 2003 between UT 10:00 and UT 18:00. The blue dots indicate the cloud bottom measured from the KNMI ceilometer. Lower panel: Time series of inferred first two moments of the photon paths ($\langle L_{tot} \rangle$ and $\sqrt{\langle L_{tot}^2 \rangle}$) in VOD units of the oxygen atmospheric column (left ordinate-axis) and liquid water path (LWP, right ordinate-axis) measured by MICCY and by HATPRO. The dashed black line shows the photon path lengths for the direct sunlight.*

Figure 5.15: *Cloud camera image sequence from the KNMI cloud camera for May 11, 2003*

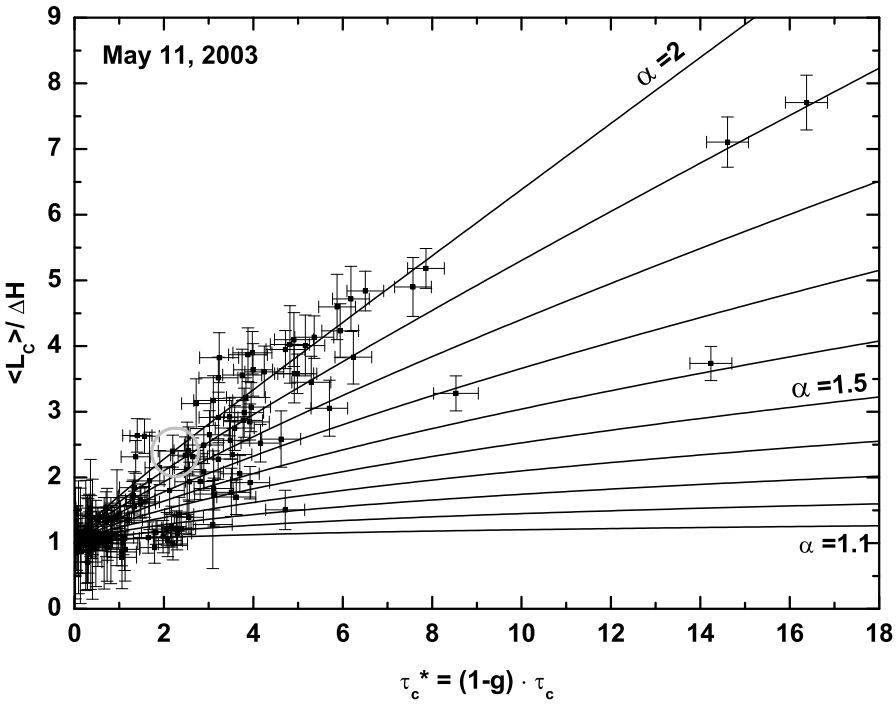

Figure 5.16: *Mean cloud photon paths* $\langle L_c \rangle$ *as a function of effective cloud optical depth* τ_c^* *for the May 11, 2003 observations. The black lines are predictions for different values of the Lévy exponent* $\alpha \leq 2$.

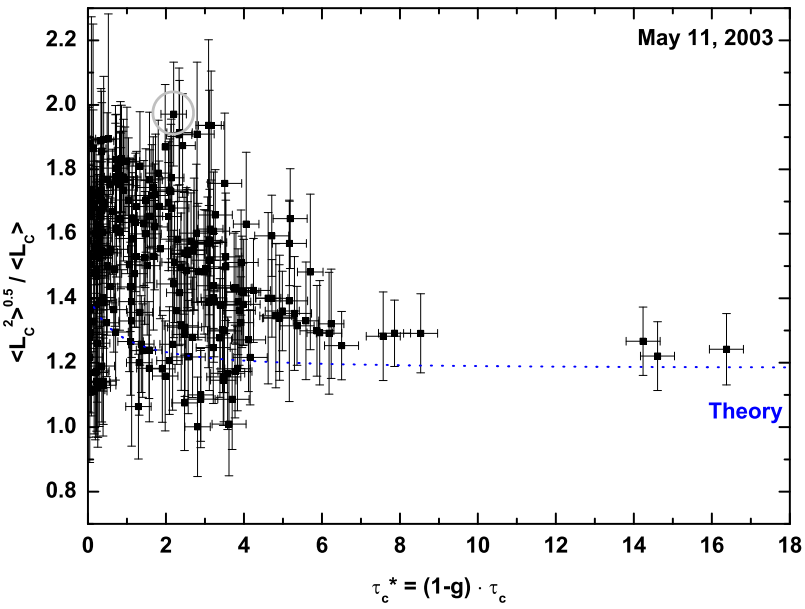

Figure 5.17: *Measured ratio of first and second moment(*$\langle L_c \rangle$ *and* $\sqrt{\langle L_c^2 \rangle}$*) for May 11, 2003 observations. The predicted ratio, based on the classical diffusion theory, is indicated by the dotted blue line.*

May 21, 2003

Figure 5.20 shows the cloud radar measurements for May 21, from UT 14:00 to UT 17:00. During the whole observed period a thin stratus cloud deck between 2000 m and 2500 m is present. Starting at UT 15:00, an increasing cirrus cloud appears over the measurement site. In contrast to May 11 observations, the cloud base retrieved from the radar backscatter signal and from ceilometer measurements are similiar.

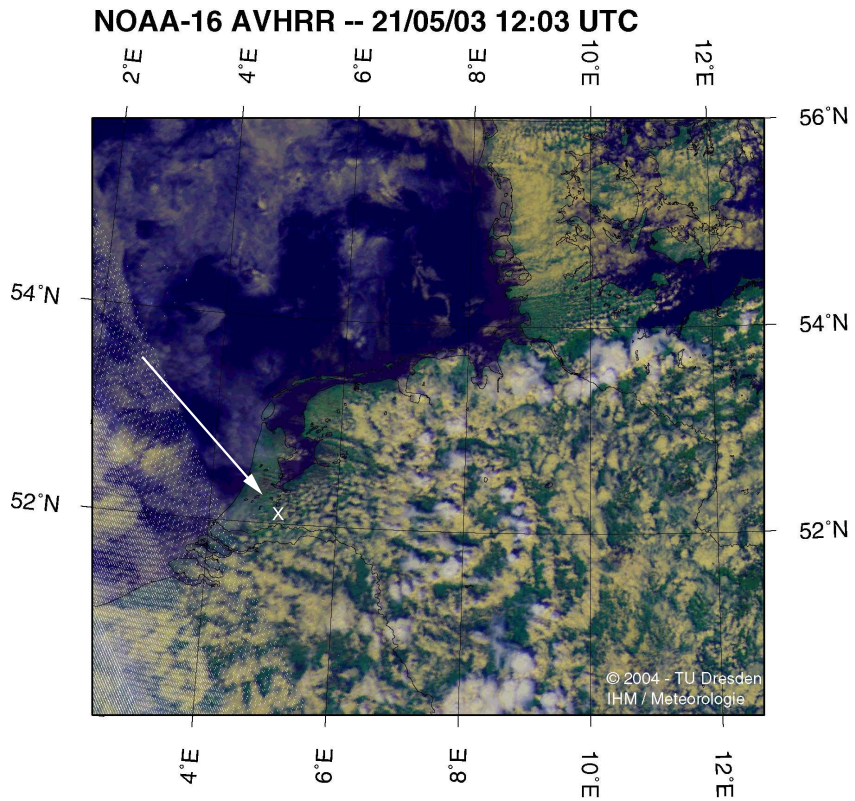

Figure 5.18: *NOAA-AVHRR Satellite Image of Central Europe for May 21, 2003*

In the lower panel of figure 5.20 the retrieved first two moments of the photon path length distributions and the microwave radiometer measurements are shown. From UT 15:12 to UT 15:33 and UT 16:40 to UT 16:55 the mean photon path length is shorter than the direct path, indicated by the dotted line. This reduction in the mean photon path length can be explained by a single scattering event within the clouds. The incident light beam reaches the cloud and is scattered by the cloud droplets. Therefore a considerable amount of photons is scattered vertically from the clouds into the instrument. As consequence the direct path length from the top of the atmosphere to the cloud and vertically from the cloud to the instru-

ment, is smaller than the direct light path from top of the atmosphere to the ground.

Figure 5.19: *Image sequence from the KNMI cloud camera for May 21, 2003*

Figure 5.18 shows the cloud situation for the presented day at UT 12:03. Over the Netherlands the cloud deck is very patchy. This structure seen in the satellite image can also be found in the cloud camera pictures (see figure 5.19). At UT 14:00 the patchy cloud structure can even be found for situations when the sky is completely covered with more or less thick clouds. The stratus cloud deck detected by the cloud radar can also be seen in the first three images, while the vanishing low clouds and the incoming high cirrus cloud can be found in the last picture at UT 17:00.

As expected from diffusion theory the lower cloud behaves like a diffusion plate. This leads to a Lévy index α around 2. For this cloud case the index α is not smaller than 1.6. The ratio between the square root of the second moment and the first moment is larger than the theoretical value (dotted blue line in figure 5.22), but for a larger rescaled optical depth ($\tau_c^* > 6$) converges to the theoretical value of 1.18. These optical depth belongs to clouds with high cloud liquid water content at UT 14:33, UT 14:59 and UT 15:56.

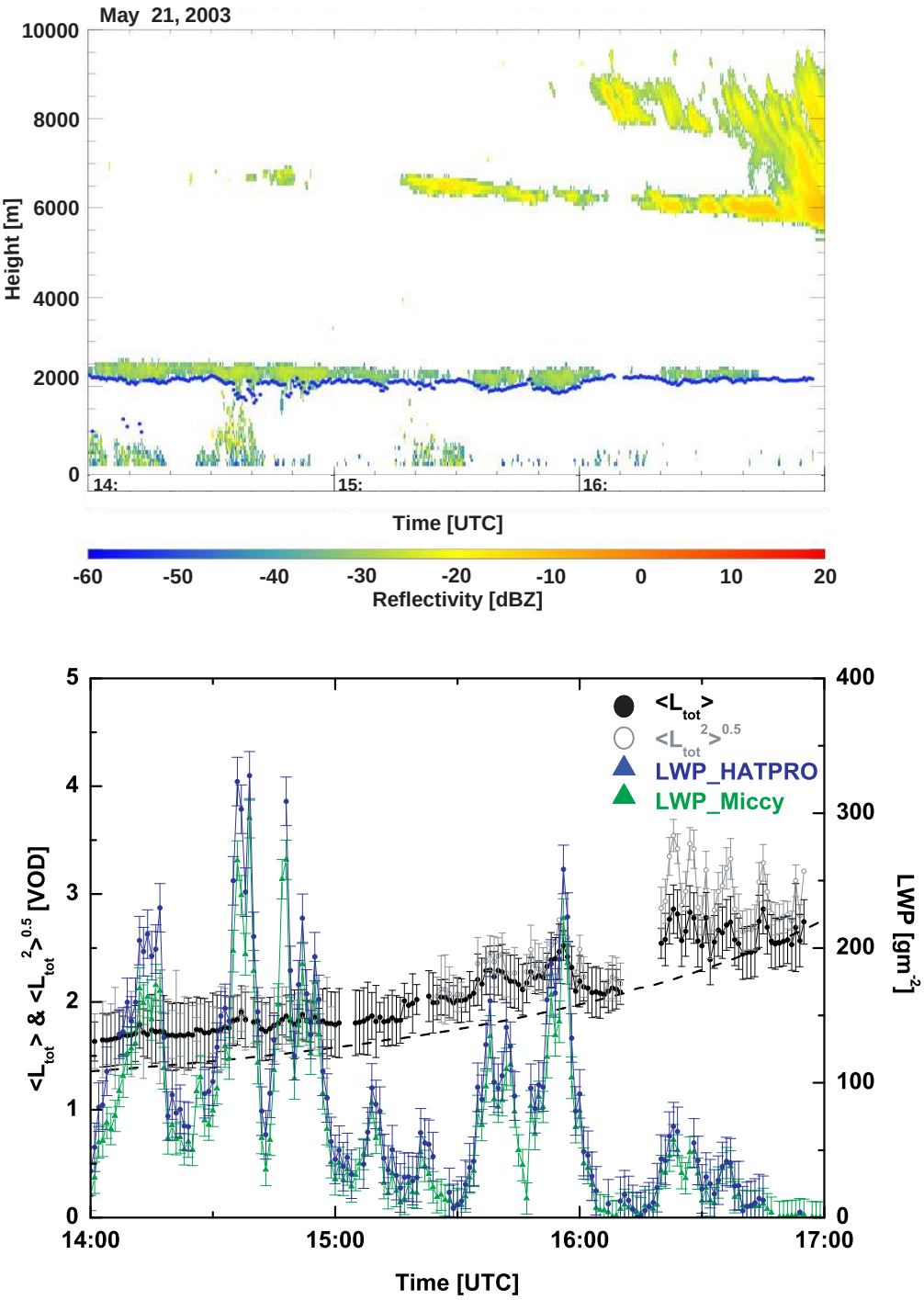

Figure 5.20: *Upper panel: Radar reflectivity measured by the KNMI 35 GHz Radar at Cabauw (NL) on May 21, 2003 between UT 14:00 and 17:00. The blue dots indicate the cloud bottom measured from the KNMI ceilometer. Lower panel: Time series of inferred first two moments of the photon paths ($\langle L_{tot} \rangle$ and $\sqrt{\langle L_{tot}^2 \rangle}$) in VOD units of the oxygen atmospheric column (left ordinate-axis) and liquid water path (LWP, right ordinate-axis) measured by MICCY and by HATPRO. The black dashed line shows the photon path lengths for the direct sunlight.*

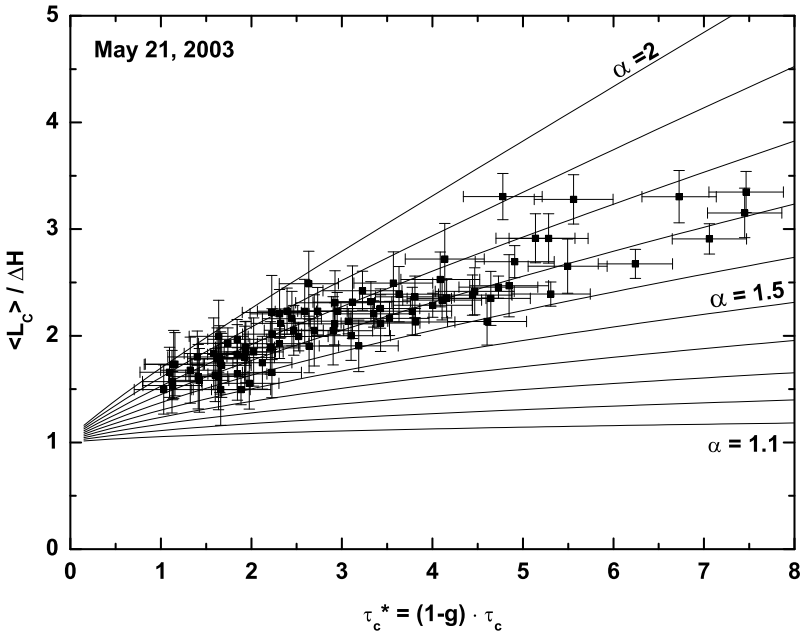

Figure 5.21: *Mean cloud photon paths* $\langle L_c \rangle$ *as a function of effective cloud optical depth* τ_c^* *for the May 21, 2003 observation. The black lines are predictions for different values of the Lévy exponent* $\alpha \leq 2$.

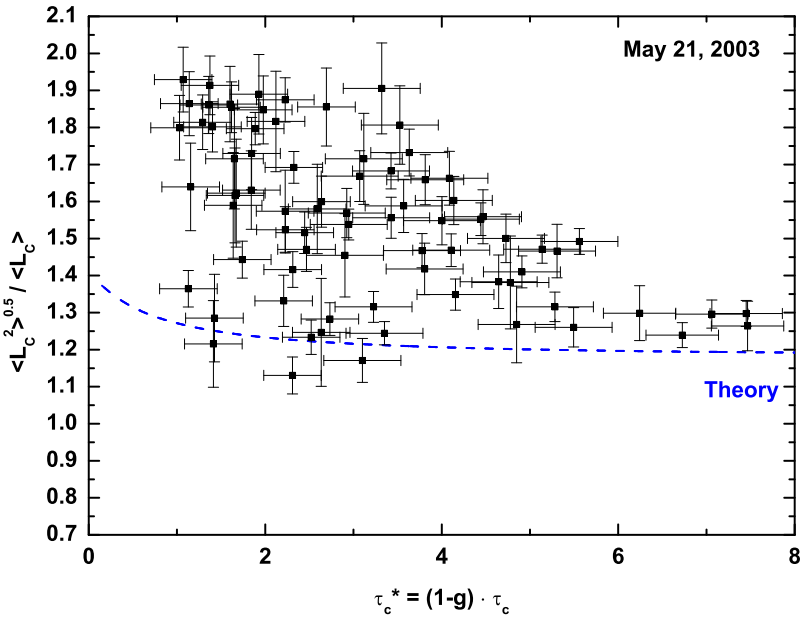

Figure 5.22: *Measured ratio of first and second moment(*$\langle L_c \rangle$ *and* $\sqrt{\langle L_c^2 \rangle}$*) for May 11, 2003 observations. The predicted ratio, based on the classical diffusion theory, is indicated by the dotted blue line.*

May 22, 2003

The KNMI cloud radar image shows a complex cloud situation for May, 22 (upper panel in Figure 5.23). A low stratus cloud deck below 1000 m is present during the whole day. Between UT 10:00 and UT 11:30 a convective cell with cumuli cloud formation and precipitation is embedded. This rain is the reason why no path length data is available from UT 10:00 and UT 12:00. At that time high cirrus clouds appeared. The mentioned cirrus is associated with a warm front which is coming from the west. In the afternoon a mid-high altostratus cloud formats and is present for the rest of the observation time.

The lower panel in figure 5.23 shows the retrieved first and second moment of the photon path length distributions and the corresponding liquid water path measurements. The rain mentioned above can be found in the microwave measurements, as the retrieved liquid water path is larger than 600 gm^{-2}. The retrieved photon path lengths also increase, until the measurements stop from UT 10:00 to UT 12:00. After UT 12:00 the retrieved path length and the measured liquid water path decrease stepwise until UT 13:00. This time period will be discussed later in this section. From UT 14:00 the incoming middle-high clouds vary the retrieved path lengths slightly. In agreement with the cloud radar measurements and the microwave radiometer measurements the two clouds at UT 14:15 and UT 14:40 are also seen in the photon path length measurements, as the values increase for the time the clouds are present above the measurement site.

The satellite image (Figure 5.24) shows the cloud situation on that day. Again the ocher-colored clouds denote low cloud height, while white colored clouds stand for high level clouds. Nearly the whole area is covered with low stratus cumulus clouds, while high level cirrus clouds appear from the west.

Figure 5.25 shows a detailed cloud radar image from UT 12:00 to UT 13:00. Three different parts are color coded and will be discussed. From UT 12:00-12:23 (green bar) a thick stratus cloud with embedded cumulus cloud (UT 12:15-12:23) below 2000 m and a cirrus cloud at 9000-10000m are present. In the second part from UT 12:23-12:46 (red bar) the lower cloud deck is much thinner than before. Also the cirrus cloud seems to break up. In the third part from UT 12:46-13:00 (blue bar) the cirrus cloud and the stratus cloud deck are thinner compared to the middle part, as the backscatter signal is now smaller. Figure 5.26 shows the cloud camera image sequence for the discussed period.

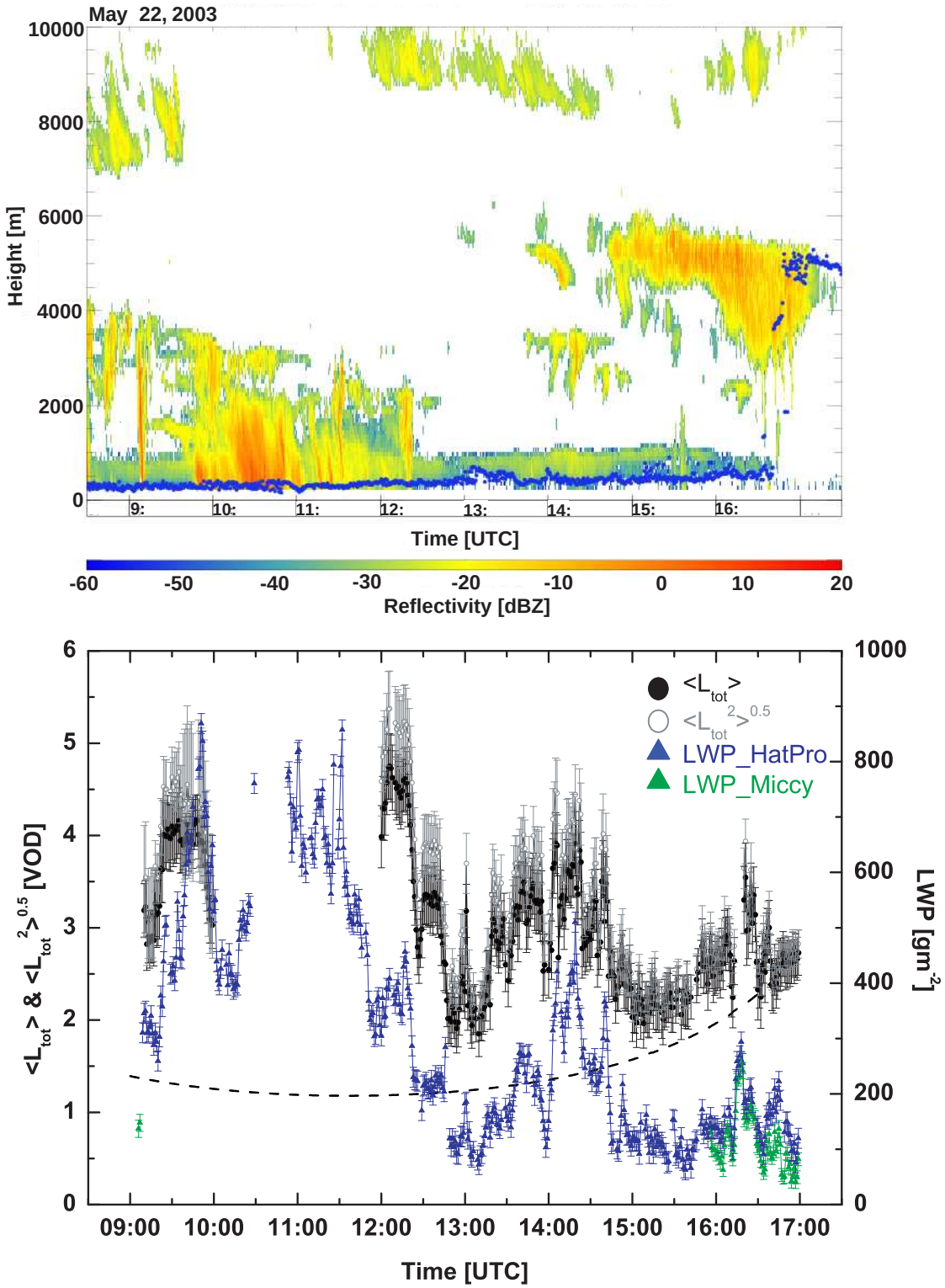

Figure 5.23: *Upper panel: Radar reflectivity measured by the KNMI 35 GHz Radar at Cabauw (NL) on May 22, 2003 between UT 09:00 and 17:00. The blue dots indicate the cloud bottom measured from the KNMI ceilometer. Lower panel: Time series of inferred first two moments of the photon paths ($\langle L_{tot} \rangle$ and $\sqrt{\langle L_{tot}^2 \rangle}$) in VOD units of the oxygen atmospheric column (left ordinate-axis) and liquid water path (LWP, right ordinate-axis) measured by MICCY and by HATPRO. The black dashed line shows the photon path lengths for the direct sunlight 1/cos(SZA).*

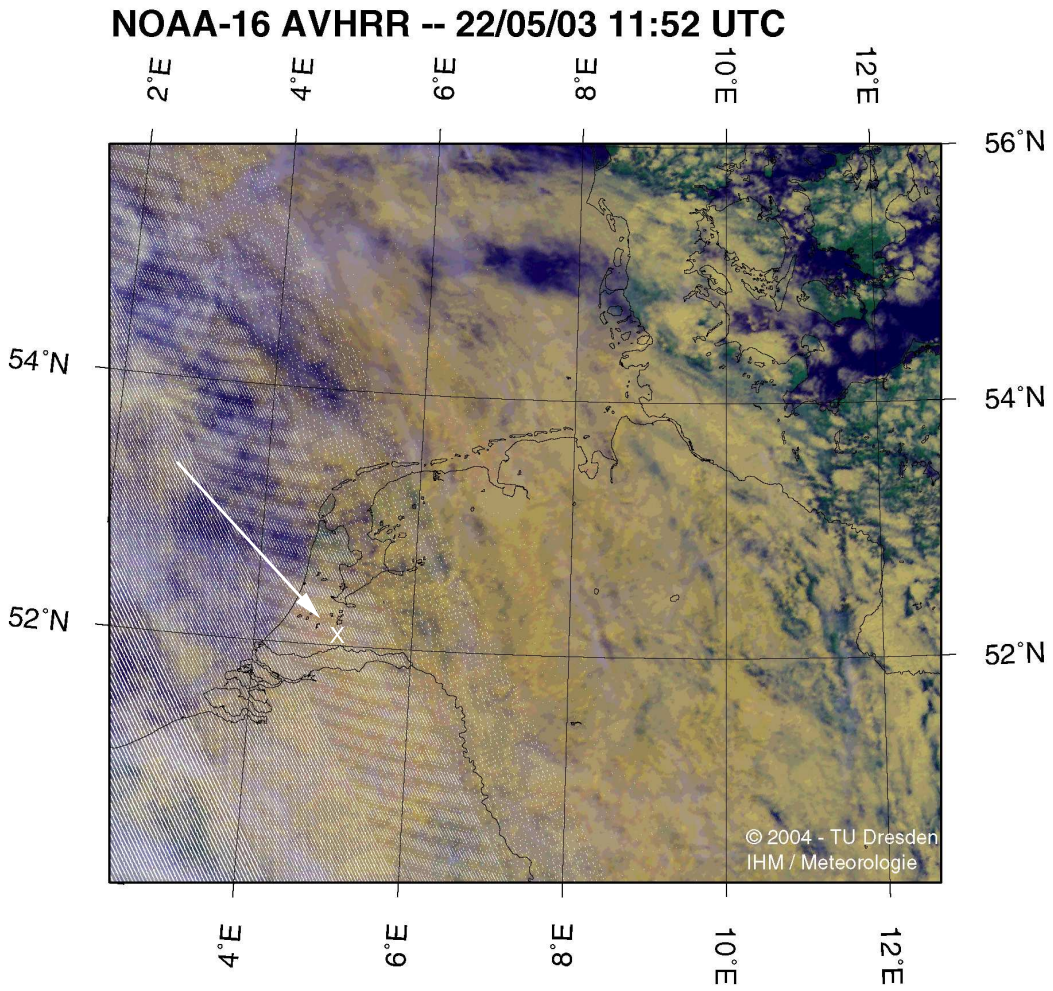

Figure 5.24: *NOAA-AVHRR Satellite Image of Central Europe for the May 22, 2003 observation*

The measured mean path lengths $\langle L_c \rangle$ are plotted as a function of the rescaled cloud optical depths τ_c^*, see Figure 5.27. All three periods, found in the cloud radar image, can be identified in this plot. During the first period (green circle) the clouds are optically thickest, with a rescaled cloud optical depth between 10 and 14. During the second (red circle) and third part (blue circle) the cloud optical thickness decreases stepwise. In this respect, it is evident that the optically much thinner cirrus cloud deck does not increase the photon path significantly. It acts as a diffuser for the solar radiation. This behavior is found in the corresponding photon path length measurements between UT 12:00 and UT 13:00. During the third period the clouds are optically thinnest, so that more photons could pass the clouds without being scattered. This can be seen in the Lévy index α reaching

values round 1.3 to 1.7. For the optically thick clouds (green mark) α is between 1.9 to 1.8, which is in good agreement with the other observed values for stratus cloud decks.

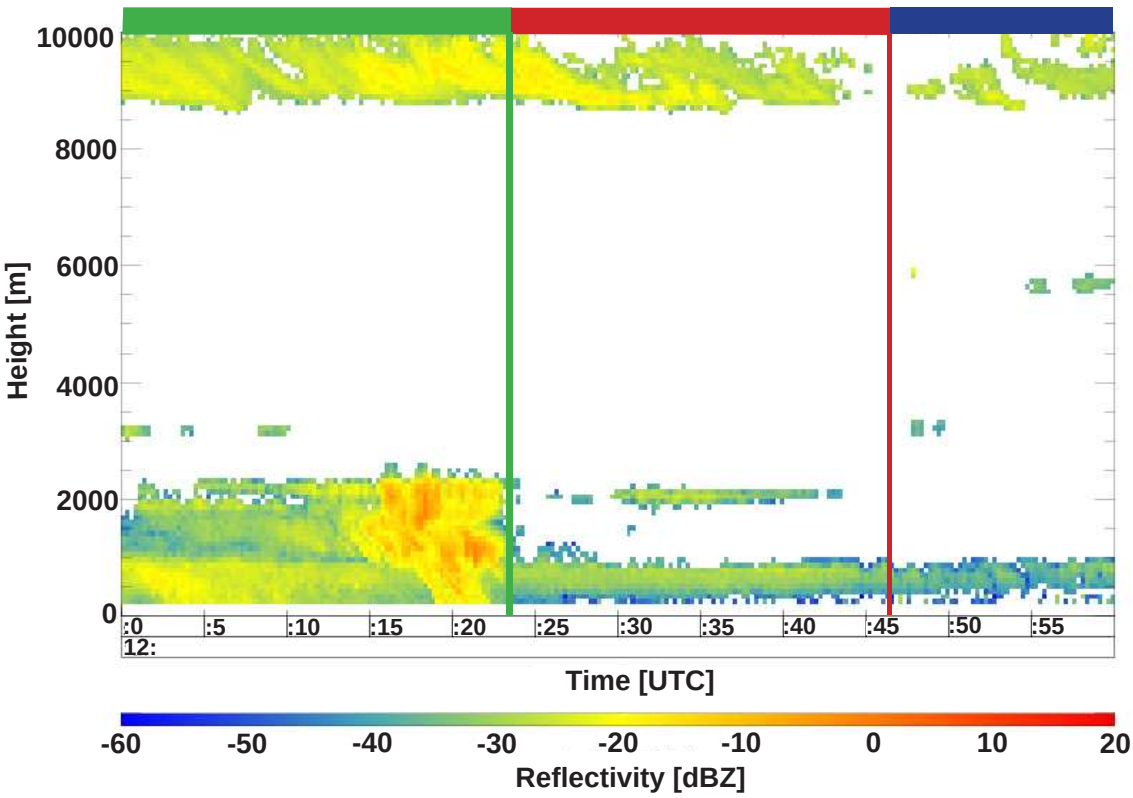

Figure 5.25: *Detailed zoom (UT 12:00-13:00) of measured radar reflectivities from KNMI 35 GHz Radar for May 22, 2003*

In figure 5.28 the ratio of the inferred mean photon path length $\langle L_c \rangle$ and the square-root second moment $\sqrt{\langle L_c^2 \rangle}$ of the path length is investigated. For small rescaled cloud optical thickness (blue circle) the ratio is higher than the theoretical prediction, while for higher τ_c^* the ratio approaches the theoretical value of 1.18.

Figure 5.26: *Image sequence from the KNMI cloud camera for UT 12:00-13:00 for May 22, 2003*

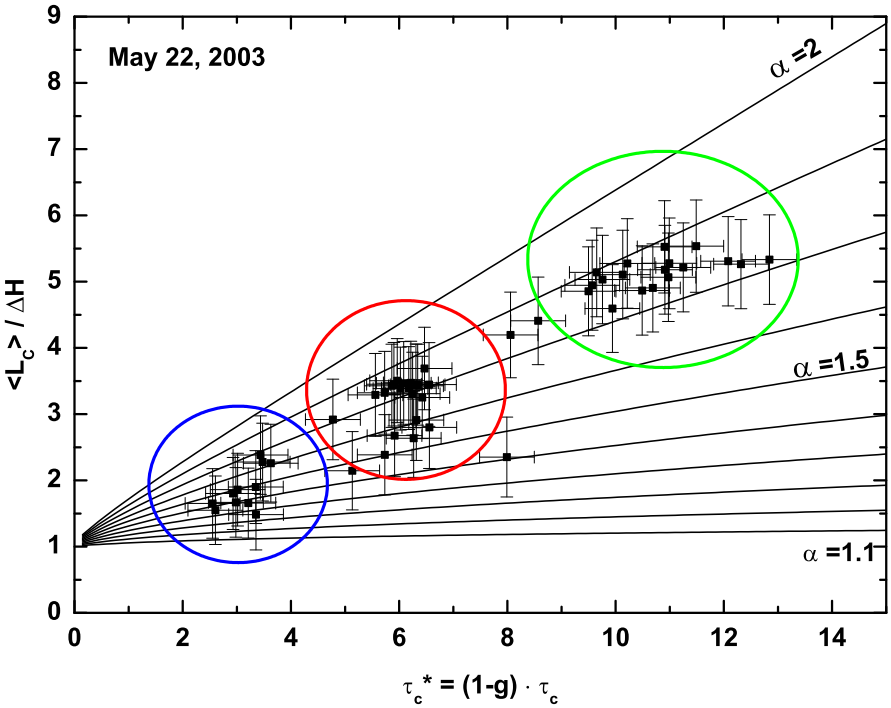

Figure 5.27: *Mean cloud photon paths $\langle L_c \rangle$ as a function of effective cloud optical depth τ_c^* for the May 22, 2003 observation. The black lines are predictions for different values of the Lévy exponent $\alpha \leq 2$. The 3 data clusters (color-coded blue, red and green) correspond to the 3 different cloud situations probed between UT 12:00-12:23, UT 12:23-12:46, and UT 12:46-13:00 in figure 5.25.*

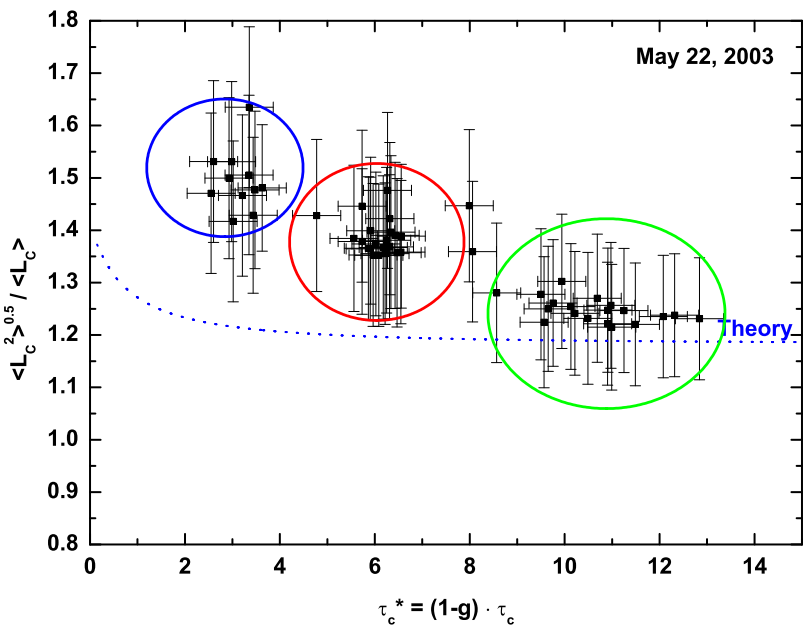

Figure 5.28: *12. Ratio of inferred first two photon path length moments($\langle L_c \rangle$ and $\sqrt{\langle L_c^2 \rangle}$) for the May 22, 2003 observations, and comparison with the predicted ratio (dashed blue line) based on the classical diffusion theory. The 3 data clusters (color-coded blue, red and green) correspond to those in figures 5.25 and 5.27.*

5.3 Discussion

The validation of the theory of anomalous photon diffusion in clouds is motivation for the presented measurements. The theoretical predictions for the mean photon path in clouds (equation 3.18) and the ratio of the first and second moment are investigated. For that purpose the measured first two moments of the photon PDF combined with the other in-situ measurements (cloud vertical extension and liquid water path) presented in the previous section are used.

For all presented observations and retrieved photon PDFs the Lévy index α is inferred. This is done by inspecting the mean path length in the cloud $\langle L_c \rangle$ in units of ΔH in VOD as a function of the rescaled cloud optical depth τ_c^*, see figures 5.7, 5.3, 5.11, 5.16 and 5.27. The measurements for all presented days demonstrate that the effective Lévy index α of the improved photon diffusion model attains all values between 1 and 2. The limiting case $\alpha = 2$ (classical diffusion) occurs only rarely in the data. By contrast, the limiting case $\alpha = 1$ (direct transmission) occurs more frequently and, in particular, when the cloud cover loosens-up.
For stratus clouds a Lévy index between 1.7 and 2.0 is found, while for cirrus clouds α is between 1.3 and 1.5. As consequence of the scaling relation of the Lévy model, the mean total photon path length is reduced and therefore the atmospheric absorption. In this respect, it is evident that an optically much thinner cirrus deck does not significantly increase the photon paths but in first instance act as diffuser for the solar radiation [*Pfeilsticker et al.* 1998]. All these findings on photon path statistics are largely in agreement with earlier empirical findings by *Pfeilsticker* [1999] and *Min et al.* [2001]. It provides further evidence for the suggestion of *Davis and Marshak* [1997] on the non classical nature of photon path statistics under real cloud covers.

The ratio of the inferred square-root of the second moments and the mean photon paths $\sqrt{\langle L_c^2 \rangle}/\langle L_c \rangle$ is also of interest. *Davis and Marshak* [2002] proposed for the ratio of the two moments a value of 1.18. For all discussed observations this ratio is determined from the measurements, see figures 5.4, 5.8, 5.12, 5.17 and 5.28. The ratios provide evidence that the numerical values of the exponents and prefactors in the hypothetical generalization of equations 3.18 and 3.20 is reasonably accurate for the predominant anomalous diffusion regime. The findings thus largely confirm the 2-moment calculus of the *Davis and Marshak* [2002] study, and it provides further evidence that the photon path statistics for real three dimensional cloud covers requires elements of non-classical (i.e., anomalous) diffusion transport physics. For rescaled cloud optical depth $\tau_c^* < 6$ the ratio of the square-root second moment and

first moment of the photon PDF varies between 1.1 and 1.8, while for $\tau_c^* > 6$ the ratio follows the theoretical predicted value of 1.18.

The presented results provide further evidence for the 3D effect of radiative transfer in clouds. As consequence the cloud RT in present GCMs has to be extended to real 3D calculations in comparison to the state-of-the-art IPA or plane-parallel cloud RT. Global warming case studies show an increase of global temperature from 2 to 5 °C for CO_2 doubling, depending from the treatment of cloud feedback. The difference between plane-parallel and IPA is so large that it would change the results in the climate models of the temperature change within the predicted range. The use of 3D cloud RT modelling could solve the problem of this large deviation between the different models. An alternative is the in this study examined Lévy model. The troposphere can be characterized as possibly cloudy medium by two free parameters, namely the cloud optical thickness and the Lévy index α. For homogeneous clouds a cloud optical thickness comparable to the IPA results and a Lévy index close to 2 are expected. On the other hand α is close to 1 and the cloud optical thickness is low for mostly clear sky and thin clouds, respectively. Besides the Lévy index the effective mean free path[3] is larger than the mean free path within the are the only required parameters to generate the photon PDF according to the Lévy model. This model is therefore well suited for a general parameterization for inhomogeneous cloudiness, requiring only a small set of observables.
The treatment of clouds in this manner has an important influence on the results of cloudy skies RT. The atmospheric absorption is reduced as the mean total path length is reduced due to cloud inhomogeneities. On the other hand multiple scattering enhance the photon path through the absorbing gas thereby enhancing the absorption. The characteristics of 3D photon transport is measurable in the radiation field and uniquely defined by the PDF. Consequently the concept of photon PDF will be the central concept of cloud RT modelling in the next GCM generation.

[3]The effective mean free path incudes also large steps between cloud patches or cloud and surface and is therefore much larger than the local mean free path within the clouds

Chapter 6

Summary and Outlook

The prime purpose of the presented thesis is to investigate the path length distribution of solar photons for cloudy skies. The objective is achieved by using high spectral resolution oxygen A-band spectroscopy of zenith scattered skylight.

Within the thesis, the previously existing experimental set-up as been largely improved by using a new and more sensitive CCD detector for light detection, and by mounting the whole instrument into a sealed, thermostated and transportable container. These improvements allow us (a) to measure skylight spectra on spatial scales smaller than radiative smoothing scale which determines cloudy sky RT, (b) to ship the equipment to any measurement site where other cloudy parameters are measured, and (c) to use the full potential of a newly developed spectral retrieval algorithm for the path length distribution detection [*Funk and Pfeilsticker* 2003].

Within the 4-D clouds AFO-2000 project, the novel instrument was operated during two field campaign which were held at Cabauw/NL in fall 2001 and spring 2003. The deployment of the instrument on the campaigns largely provided the benefit of the additional measurement of other cloudy sky parameters, such as the cloud vertical extension (by Radar and ceilometers), liquid water path by microwave spectrometry and the effective cloud droplet radius, and the vertical temperature and pressure profiles by radiosonde ascents, which were all found to be necessary for the interpretation of the inferred cloudy sky photon path PDF.

The method to infer cloudy sky photon path PDFs has been validated by two means: In a first test, sensitivity studies were conducted which clearly demonstrated the information content of the measured spectra. This investigation provides basics information on the mathematical requirements in assuming wide vs narrow distributed photon path PDFs. The second test addressed, the analysis of a Monte

Carlo modelled oxygen a-band spectrum for a modelled cloud scene from which the photon path PDF is inferred using our retrieval tools and compared with the simulated PDF. The comparison resulted in an excellent agreement for $\langle L_t ot \rangle$, but in an different widths for both PDFs.

The measured field data were used to study classical vs anomalous photon diffusion in real cloud covers. The study essentially confirmed the predictions and findings of earlier studies [*Pfeilsticker* 1999], [*Min et al.* 2001] and [*Davis and Marshak* 1997], however it went beyond these by testing the theoretical predictions for first and second moments of the photon path PDFs made in a recent study [*Davis and Marshak* 2002]. Basically the following is found.

(1) The ratio of the measured first two moments $\sqrt{\langle L_c^2 \rangle}/\langle L_c \rangle$ is found to excellently agree with the theoretical prediction [*Davis and Marshak* 2002]. Hereby for re-scaled optical depth $\tau_c^{>}$ 6, the ratio is found to exactly follow the theoretical predicted value of 1.18, while for smaller optical depth the ratio spread into a wider range between 1.1 and 1.8. Remarkably the first and second moment behave like mono-fractals as they were found to increase with the same power of the moment rank even though the underlying liquid cloud water field is known to be a multi-fractal.

(2) The investigated cloud cases show clearly that under cloudy skies the first two moments of the photon path length distribution scale like $< L_c > /\Delta H \sim (\tau_c^*)^{\alpha-1}$ and $< L_c^2 > /\Delta H^2 \sim (\tau_c^*)^{\alpha}$ with α being in the range between 1 and 2. The observations indicated that, optically thick single cloud decks tend to support Lévy indices close to $\alpha = 2$ which indicate classical photon transport. For complicated cloud covers, i.e. broken in place and multi-layered cloud covers, however, the radiative transport is obviously being better characterized as anomalous diffusion since the Lévy indices α attain values between 1 and 2. In agreement with previous studies ([*Wagner et al.* 1998] and [*Pfeilsticker et al.* 1998]) it is found that for cirrus clouds the photon paths become shorter than for low and middle-high stratus clouds. This study also confirmed predictions of the size of the pre-factor in the classical path length to optical depth relations elaborated in a recent study [*Davis and Marshak* 2002] for the anomalous photon diffusion regime. This study also extended the parameter range of previous studies, [*Pfeilsticker* 1999] and [*Min et al.* 2001], to smaller cloud optical depths.

The present result thus provides further evidence that, cloudy skies photon path lengths, and hence atmospheric absorption require some elements of non-classical

photon transport.

Here this study could also show that the theory of anomalous diffusion of clouds is well developed for the transmission case. In order to prove the photon path theory for the reflection case, a similar instrument should be set-up on air-borne platforms like balloons or airplanes. Such measurements and a robust and validated theory for the reflection cases were also very helpful to improve the satellite retrieval for cloud top height measurements using A-band spectroscopy from satellites.

One consequence of the detected scaling relation of the Lévy model is the reduction in the total photon path length. Evidently a reduction of photon pathes leads to a reduction in atmospheric absorption. On the other hand, the Lévy distribution also support a larger fraction of photons travelling extra long pathes, increasing atmospheric absorption. The cooperate action of both effects may lead to smaller or larger atmospheric absorption largely depending on the geometry, size and microphysics of the clouds cover [*Scheirer and Macke* 2003]. Finally photon path PDF measurements may also help to develop refined parameterization of cloud covers and their interaction with radiation in global circulation models (GCMs).

The present study thus underlines that the photon path PDF measurements using oxygen A-band spectroscopy developed into a matured technique in recent years.

Appendix A

HITRAN

In table A.2 the used spectroscopic data are listed. For the (0,0) $^{16}O_2$ the line strength data based on *Funk* [2000] were used, whereas the other data are taken from HITRAN2000. For the (0,0) $^{16}O^{18}O$ transitions and for the (1,1) $^{16}O_2$ transitions the spectroscopic data are also from HITRAN2000.

Table A.1: *Format of the HITRAN output for spectroscopic line data. For details see [Rothman et al. 2003].)*

`FORMAT(I2,I1,F12.6,1P2E10.3,0P2F5.4,F10.4,F4.2,F8.6,2I3,A9,2(A1,I2),2X,A1,3I1,3I2)`

Mol, Iso, ν, S, $\Re$, γ_{air}, γ_{self}, E'', n, δ, iν', iν'', q', br, N'', br, J'', sym, ierr, iref

Mol	molecule identifier, 7: oxygen
Iso	isotope identifier, 1: $^{16}O_2$, 2: $^{18}O^{16}O$, 3: $^{17}O^{16}O$
ν	line center in cm^{-1}, in vacuum
S	line strength in cm (or $cm^{-1}molec^{-1}cm^2$)
γ_{air}	air broadened half width in $cm^{-1}atm^{-1}$
γ_{self}	self broadened half width in $cm^{-1}atm^{-1}$
E''	initial state energy in cm^{-1}
n	coefficient of the temperature dependence of air-broadened half width
upper and lower state global quanta:	
iν',	1: $X^3\Sigma_g^-{}_{(\nu=0)}$, 2: $X^3\Sigma_g^-{}_{(\nu=1)}$
iν''	5: $b^1\Sigma_g^+{}_{(\nu=0)}$, 6: $b^1\Sigma_g^+{}_{(\nu=1)}$
upper and lower state local quanta:	
br, N''	branch (P or R) for ΔN, and N'' of inital state
br, J''	branch (P, R or Q) for ΔJ, and J'' of inital state

Table A.2: *Oxygen line data in 100 character HITRAN format, see Table A.1*

.

(0,0) $^{16}O_2$:

```
7113021.291250 4.410E-25 3.250E-08.0391.0390  933.5311 .63 -.00900  5  1         P25P25  d46535 2 5
7113023.079050 4.220E-25 3.211E-08.0388.0387  931.7330 .63 -.00900  5  1         P25Q24  d46535 2 5
7113010.812660 2.270E-25 3.253E-08.0376.0375 1085.2037 .63 -.00900  5  1         P27P27  d46535 2 5
7113012.582860 2.180E-25 3.218E-08.0373.0372 1083.4335 .63 -.00900  5  1         P27Q26  d46535 2 5
7112999.957240 1.100E-25 3.258E-08.0363.0362 1248.2019 .63 -.00900  5  1         P29P29  d46535 2 5
7113001.709840 1.060E-25 3.223E-08.0355.0354 1246.4493 .63 -.00900  5  1         P29Q28  d46535 2 5
7112988.722740 5.093E-26 3.263E-08.0349.0348 1422.4995 .63 -.00900  5  1         P31P31  d46535 2 5
7112990.458040 4.925E-26 3.231E-08.0341.0340 1420.7642 .63 -.00900  5  1         P31Q30  d46535 2 5
7112977.107380 2.199E-26 3.268E-08.0336.0335 1608.0680 .63 -.00900  5  1         P33P33  d46535 2 5
7112978.825380 2.132E-26 3.238E-08.0325.0324 1606.3500 .63 -.00900  5  1         P33Q32  d46535 2 5
```

(1,1) $^{16}O_2$:

```
7112974.659503 6.478E-28 1.705E-08.0563.0656 1560.3249 .70 .000000  6  2         R 1R 1  d00624 5 5
7112976.544618 1.503E-27 2.351E-08.0563.0556 1558.4398 .70 .000000  6  2         R 1Q 2  d00624 5 5
7112979.661297 1.812E-27 2.189E-08.0540.0534 1574.5429 .74 .000000  6  2         R 3R 3  d00624 5 5
7112981.617678 2.622E-27 2.440E-08.0540.0534 1572.5865 .74 .000000  6  2         R 3Q 4  d00624 5 2
7112984.269584 2.665E-27 2.320E-08.0518.0512 1600.1329 .73 .000000  6  2         R 5R 5  d00624 5 5
7112986.263595 3.391E-27 2.473E-08.0518.0512 1598.1388 .73 .000000  6  2         R 5Q 6  d00624 5 5
7112988.482825 3.116E-27 2.379E-08.0498.0493 1637.0905 .74 .000000  6  2         R 7R 7  d00624 5 5
7112990.504718 3.730E-27 2.488E-08.0498.0493 1635.0686 .74 .000000  6  2         R 7Q 8  d00624 5 5
7112992.299261 3.165E-27 2.413E-08.0478.0475 1685.4100 .72 .000000  6  2         R 9R 9  d00624 5 5
7112994.344885 3.658E-27 2.497E-08.0478.0475 1683.3643 .72 .000000  6  2         R 9Q10  d00624 5 5
7112995.716909 2.893E-27 2.434E-08.0460.0459 1745.0832 .70 .000000  6  2         R11R11  d00624 5 5
7112997.784119 3.267E-27 2.503E-08.0460.0459 1743.0160 .70 .000000  6  2         R11Q12  d00624 5 5
7112998.733564 2.420E-27 2.449E-08.0443.0444 1816.1005 .66 .000000  6  2         R13R13  d00624 5 5
7113000.821111 2.689E-27 2.507E-08.0443.0444 1814.0129 .66 .000000  6  2         R13Q14  d00624 5 5
7113001.346797 1.871E-27 2.460E-08.0428.0431 1898.4502 .65 .000000  6  2         R15R15  d00624 5 5
7113003.453896 2.053E-27 2.510E-08.0428.0431 1896.3431 .65 .000000  6  2         R15Q16  d00624 5 5
7113003.553955 1.344E-27 2.468E-08.0414.0420 1992.1189 .64 .000000  6  2         R17R17  d00624 5 5
7113005.352162 9.016E-28 2.474E-08.0401.0411 2097.0913 .63 .000000  6  2         R19R19  d00624 5 5
7113005.680082 1.462E-27 2.513E-08.0414.0420 1989.9928 .64 .000000  6  2         R17Q18  d00624 5 5
7113006.738312 5.662E-28 2.479E-08.0389.0403 2213.3501 .63 .000000  6  2         R21R21  d00624 5 5
7113007.496952 9.731E-28 2.513E-08.0401.0411 2094.9465 .63 .000000  6  2         R19Q20  d00624 5 5
7113007.709074 3.336E-28 2.484E-08.0379.0397 2340.8764 .63 .000000  6  2         R23R23  d00524 5 5
7113008.092279 4.721E-29 2.495E-08.0356.0388 2790.8417 .63 .000000  6  2         R29R29  d00524 5 5
7113008.260888 1.847E-28 2.488E-08.0370.0392 2479.6492 .63 .000000  6  2         R25R25  d00524 5 5
7113008.389964 9.621E-29 2.491E-08.0362.0389 2629.6458 .63 .000000  6  2         R27R27  d00524 5 5
7113008.901504 6.074E-28 2.515E-08.0389.0403 2211.1869 .63 .000000  6  2         R21Q22  d00624 5 5
7113009.890476 3.561E-28 2.516E-08.0379.0397 2338.6950 .63 .000000  6  2         R23Q24  d00524 5 5
```

(0,0) $^{16}O^{18}O$:

```
7213005.105811 1.978E-28 3.192E-08.0422.0414 1259.1207 .63 -.00900  5  1         P30Q29  d00526 2 5
7213008.628940 2.932E-28 3.218E-08.0422.0414 1179.8725 .63 -.00900  5  1         P29P29  d00526 2 5
7213010.393614 2.832E-28 3.190E-08.0426.0418 1178.1078 .63 -.00900  5  1         P29Q28  d00526 2 5
7213013.816926 4.144E-28 3.216E-08.0426.0418 1101.5383 .63 -.00900  5  1         P28P28  d00526 2 5
7213015.589817 3.996E-28 3.186E-08.0430.0422 1099.7654 .63 -.00900  5  1         P28Q27  d00526 2 5
7213018.913674 5.776E-28 3.215E-08.0430.0422 1025.8778 .63 -.00900  5  1         P27P27  d00526 2 5
7213020.694808 5.561E-28 3.184E-08.0437.0428 1024.0966 .63 -.00900  5  1         P27Q26  d00526 2 5
7213023.919552 7.935E-28 3.213E-08.0437.0428  952.8937 .63 -.00900  5  1         P26P26  d00526 2 5
```

Appendix B

Andor basics

An Andor CCD camera is used as detector for the oxygen A-band measurements (see section 4.1). The camera itself is controlled by its own software, which provides a simple basic script language.
To perform the spectroscopic measurements automatically, the following program is used. The temperature of the CCD chip is set to -50° Celsius. To check the accuracy of the spectral measurements periodically dark current and offset measurements were performed automatically during the day. These were done in addition to the dark current and offset measurements at the beginning and the end of the daily measurements. To provide a full saturation of the CCD registers a automatic exposure time control is included. It uses the maximum counts derived from the previous spectrum multiplied by an empirically derived factor to calculate the exposure time for the actual measurement. For each spectrum an entry is written to a log file, containing all important information. The exact time (hour, minute, second) is written as first column in the log file and in addition used to name the spectrum data file. Also the average counts per pixel, the exposure time and the CCD chip temperature is saved. The spectra are saved in ASCII format, containing pixel number and counts per pixel. For the full spectrum evaluation, the AFIT and PDFFIT routines were used. A detailed description of these programs can be found in *Funk* [2000].

```
//*********************************************************************
// program in AndorBasic
//*********************************************************************

// global options and settings

//Temperature of CCD-Cooler
Temperatur = -50

//time do measure dark current
darktime=60

// timer
```

```
Startzeithour=5 //hour to begin at Startzeitmin=0  //minute to
begin at Endzeithour=18  //hour to end at Endzeitmin=0    //minute
to end at

//path to files
root$="C:\measurement\"

maxmesszeit=5 belichter=0.5 //dont touch


cls() gosub .setshutter gosub .cooler gosub .gettime gosub .htos


input "Shutter-Time: " messzeit

//------------ ende der Einstellungen -----------//

zaehler=0 absmax=0 writecount=0 counts=belichter*65535*2048

print Startzeit,Endzeit,aktzeit while(1)
    while ( (aktzeit>=Startzeit) AND (aktzeit<Endzeit) )

    // Alle 500 Messungen Dunkelstrom und Offset Messungen //

        if (zaehler==0) then
            gosub .darkcurrent
            gosub .offset
        endif

        if (zaehler<500) then
            gosub .messung
        else
            gosub .darkcurrent
            gosub .offset
            zaehler=0
        endif

            if (aktmax>absmax && zaehler!=0) then
                absmax=aktmax
            endif

            print zaehler, dayy$;":";hourr$;":";min$;":";sec$,"AMax: "; aktmax, "Max: ";
            absmax,"Counts: ";counts,"Singl: ";single, "STime: "; messzeit, "Temp: "; GetTemperature()
            gosub .writelog
        zaehler=zaehler+1

        wend

    gosub .gettime
    delay(10000)
wend closewindow(#0) end

//---- Unterprogramme ---//

.writelog
    if (writecount==0) then
        logfile$ = root$;dayy$;"\";hourr$;min$;sec$;".log"
        write(logfile$, "NR", "Filename", "AktM", "Max", "Counts", "Singl", "STime", "Temp")
        writecount=writecount+1
    else
        write(logfile$, zaehler, dayy$;hourr$;min$;sec$;".o2a",aktmax, absmax, counts,
        single, messzeit, GetTemperature())
        writecount=writecount+1
    endif
return
```

```
.gettime
    min$=mid$(time$(),4,2)
    hour$=mid$(time$(),1,2)
    sec$=mid$(time$(),7,2)
    day$=left$(date$(),2)

    if (strcomp(left$(day$,1)," ")) then
      dayy$=day$
    else
      dayy$="0";right$(day$,1)
    endif

    if (strcomp(left$(hour$,1)," ")) then
      hourr$=hour$
    else
      hourr$="0";right$(hour$,1)
    endif

    acthour=val(hourr$)*3600
    actmin=val(min$)*60
    aktzeit=acthour+actmin
return


.darkcurrent                    // Dunkelstrommessung
      SetSingleTrack(256,400)  // CCD liest Pixel 56 bis Pixel 456 aus
      SetSingleScan(darktime)  // Belichtungszeit eines Spektrums
      SetShutter(0,1)          // Shuttersteuerung erfolgt automatisch
      SetReadoutTime(16)       // Pixel Readout Time in mysec
      run()
      gosub .gettime
      file$ = root$;dayy$;"\";hourr$;"\";dayy$;hourr$;min$;sec$;".dc"
      copy(#0,#1)
      print "Dark Current: ";file$
      saveAsciiXY(#1,file$)
return

.offset                           // Offsetmessung
    SetSingleTrack(256,400)    // CCD liest Pixel 56 bis Pixel 456 aus
    SetAccumulate(0.02,40,1.0) // 40 Messungen (Dauer0.2sec, Abstand 1.0sec) aufaddiert
    SetShutter(0,1)          // Shuttersteuerung erfolgt automatisch
    SetReadoutTime(16)       // Pixel Readout Time in mysec
    run()
    delay(300)
    gosub .gettime
    file$ = root$;dayy$;"\";hourr$;"\";dayy$;hourr$;min$;sec$;".ofs"
    copy(#0,#2)
    print "Offset: ";file$
    saveAsciiXY(#2,file$)
    rem CloseWindow(#1)
return

.messung
  SetSingleTrack(256,400)  // CCD liest Pixel 56 bis Pixel 456 aus
  gosub .getbelicht
  SetSingleScan(messzeit)       // Belichtungszeit eines Spektrums
  SetShutter(2,1)          // Shuttersteuerung erfolgt automatisch
  SetReadoutTime(16)       // Pixel Readout Time in mysec
  run()
  delay(300)
  gosub .gettime
  file$ = root$;dayy$;"\";hourr$;"\";dayy$;hourr$;min$;sec$;".o2a"
  aktmax=maxval(#0,1,2048)
  counts=area(#0_sig,1,2048)
```

```
  single=(counts/aktmax)/1500
  saveAsciiXY(#0,file$)
return

.htos
    Startzeithour=Startzeithour*3600
    Startzeitmin=Startzeitmin*60
    Endzeithour=Endzeithour*3600
    Endzeitmin=Endzeitmin*60
    Startzeit=Startzeitmin+Startzeithour
    Endzeit=Endzeitmin+Endzeithour
return

.cooler
    SetTemperature(Temperatur)
    Cooler(1)
return

.setshutter
    SetShutterTransferTime(0.006)
    SetTriggerMode(0)
return

.getbelicht
    tempmaxmesszeit=messzeit*1.2
    messzeit=messzeit*(belichter*65535*2048)/counts
    if(messzeit>tempmaxmesszeit) then
        messzeit=tempmaxmesszeit
        if (messzeit>maxmesszeit) then
            messzeit=maxmesszeit
        endif
    endif
return
```

List of Figures

1.1 Earth's atmosphere energy balance 12
1.2 Sources of uncertainties in climate modelling 14

2.1 Mie scattering phase function of cloud water droplets 21
2.2 The DOAS principle 24
2.3 Cross section spectrum of the oxygen A-band 28

3.1 Comparison of the most important spectral line shapes 43
3.2 Schematic view of the photon path length retrieval process 47
3.3 Schematics of the cloudy sky radiative transfer 52

4.1 Instrumental Set-up 58
4.2 Functional principle of an Echelle grating 59
4.3 Dispersion function for the used SOPRA F1500 spectrometer 60
4.4 Out of band rejection 63
4.5 Schematic of the equivalent width W of an absorption line 64
4.6 Curve of growth 66
4.7 Spectrum analysis using delta peak 68
4.8 Spectrum analysis using lognorm distribution 69
4.9 Spectrum analysis using gamma distribution 70
4.10 Simulated GESIMA cloud 72
4.11 Comparison of the different model resolutions 75
4.12 High resolved modelled spectrum 75
4.13 Residual of the Monte Carlo simulation and the evaluation program . 77
4.14 Inferred Photon Path PDF using the Monte Carlo simulation and evaluation program 78

5.1 Radar reflectivity, measured photon path length and liquid water path for September 18, 2001 . . . 82
5.2 Satellite image for September 18, 2001 . . . 83
5.3 Lévyplot for September 18, 2001 . . . 85
5.4 Ratio of first and second moment for September 18, 2001 . . . 85
5.5 Satellite image for September 23, 2001 . . . 86
5.6 Radar reflectivity, measured photon path length and liquid water path for September 23,2001 observation . . . 88
5.7 Lévyplot for September 23, 2001 . . . 89
5.8 Ratio of first and second moment for September 23, 2001 . . . 89
5.9 Satellite image for the May 8, 2003 observation . . . 91
5.10 Radar reflectivity, measured photon path length and liquid water path for May 8, 2003 . . . 93
5.11 Lévyplot for May 8, 2003 . . . 94
5.12 Ratio of first and second moment for May 8, 2003 . . . 94
5.13 Satellite image for the May 11, 2003 observation . . . 96
5.14 Radar reflectivity, measured photon path length and liquid water path for May 11, 2003 . . . 97
5.15 Cloud camera images for May 11, 2003 . . . 98
5.16 Lévyplot for May 11, 2003 . . . 99
5.17 Ratio of first and second moment for May 11, 2003 . . . 99
5.18 Satellite image for May 21, 2003 . . . 100
5.19 Cloud camera images for May 21, 2003 . . . 101
5.20 Radar reflectivity, measured photon path length and liquid water path for May 21, 2003 observations . . . 102
5.21 Lévyplot for May 21, 2003 observations . . . 103
5.22 Ratio of first and second moment for May 11, 2003 observations . . . 103
5.23 Radar reflectivity, measured photon path length and liquid water path for May 22, 2003 observation . . . 105
5.24 Satellite image for the May 22, 2003 observation . . . 106
5.25 Detailed KNMI radar image for UT 12:00-13:00 for May 22, 2003 observations . . . 107
5.26 Cloud camera images for UT 12:00-13:00 for May 22, 2003 . . . 108
5.27 Lévyplot for UT 12:00-13:00 for May 22, 2003 . . . 109
5.28 Ratio of first and second moment for May 22, 2003 . . . 109

List of Tables

2.1 The oxygen absorption bands 27

A.1 HITRAN format 117
A.2 Oxygen line data 118

References

Andor (1999). *A programmer's guide to Andor basic, Version 2A*. Andor. 4.1.1

Beirle, S., U. Platt, M. Wenig, and T. Wagner (2004). Highly resolved global distribution of tropospheric NO_2 using GOME narrow swath mode data. *Atmos. Chem. Phys.,* Vol. 4, 1913 1924. 2.3

Blobel, V. and E. Lohrmann (1998). *Statistische und numerische Methoden der Datenanalyse*. Stuttgart: Teubner. 3.5.1

Boas, M. L. (1983). *Mathematical methods in the physical sciences*. New York: John Wiley & Sons. 3.3

Bobrowski, N., G. Hönninger, B. Galle, and U. Platt (2003). Detection of bromine monoxide in a volcanic plume. *Nature,* Vol. 423, No. 6937, 273 – 276. 2.3

Bösch, H., C. Camy-Peyret, M. Chipperfield, R. Fitzenberger, H. Harder, U. Platt, and K. Pfeilsticker (2003). Upper limits of stratospheric IO and OIO inferred from center-to-limb-darkening-corrected balloon-borne solar occultation visible spectra: Implications for total gaseous iodine and stratospheric ozone. *J. Geophys. Res,* Vol. 106, No. D15, doi: 10.1029/2002JD003078. 2.3

Buldyrev, S. V., S. Havlin, A. Y. Kazakov, M. G. E. da Luz, E. P. Raposo, H. E. Stanley, and G. M. Viswanathan (2001). Average time spent by Lévy fights and walks on an interval with absorbing boundaries. *Phys. Rev. E,* Vol. 64, 41108 – 41118. 3.1.5

Burrows, J., E. Hölzle, A. Goede, H. Visser, and W. Fricke (1995). SCIAMACHY - Scanning Imaging Absorption Spectrometer for Atmospheric Chartography. *Acta Astronautica,* Vol. 35, 445. 2.3

Burrows, J., U. Platt, K. Chance, M. Vountas, V. Rozanov, A. Richter, H. Haug, and L. Marquard (1996). *Study of the Ring Effect*. Noordivijk, The Netherlands: European Space Agency.

Burrows, J., M. Weber, M. Buchwitz, V. Rozanov, A. Ladstaetter-Weisenmeyer, A. Richter, R. de Beek, R. Hoogen, K. Bramstadt, K. Eichmann, M. Eisinger, and D. Perner (1999). The Global Ozone Monitoring Experiment (GOME): Mission concept and first scientific results. *J. Atmos. Sci.,* Vol. 56, 151 – 175. 2.4.1

Cahalan, R. and J. Snider (1989). Marine stratocumulus structiure. *Remote Sens. Environ.,* Vol. 28, 95–107.

Case, K. and P. Zweifel (1967). *Linear Transport Theory.* Addison-Wesley. 3.1.4, 3.9.1

Crewell, S., H. Bloemink, A. Feijt, S. García, D. Jolivet, O. Krasnov, A. van Lammeren, U. Löhnert, E. van Meijgaard, J. Meywerk, M. Quante, K. Pfeilsticker, S. Schmidt, T. Scholl, C. Simmer, M. Schröder, T. Trautmann, V. Venema, M. Wendisch, and U. Willén (2004). The BALTEX Bridge Campaign - An integrated approach for a better understanding of clouds. *Bull. Am. Met. Soc.,* Vol. 85, 1565 – 1584. 3.9.1, 5.2.1

Crewell, S., H. Czekala, U. Lhnert, C. Simmer, T. Rose, R. Zimmermann, and R. Zimmermann (2001). Microwave Radiometer for Cloud Carthography: A 22-channel ground-based microwave radiometer for atmospheric research. *Radio Science,* Vol. 36, 621 – 638. 5.2.1

Davis, A., R. Cahalan, J. Spinhirne, M. McGill, and S. Love (1999). Off-beam lidar: An emerging technique in cloud remote sensing based on radiative Green-function theory in the diffusion domain. *Phys. Chem. Earth (B),* Vol. 24, 241 – 260, (Erratum 757 – 765). 3.9.1, 3.9.1

Davis, A. and A. Marshak (1997). Lévy kinetics in slab geometry: Scaling of transmission probability. In M. M. Novak and T. G. Dewey (Eds.), *Fractal Frontiers*, pp. 63–72. World Sci., River Edge, N.J. 3.1.5, 6

Davis, A. B. and A. Marshak (2002). Space-time characteristics of light transmitted by dense clouds: A Green function analysis. *J. Atmos. Sci.,* Vol. 59, 2713 – 2727. 6

Demtröder, W. (1998). *Laser Spectroscopy* (2. ed.). Berlin: Springer. 3.4.2

Dicke, R. H. (1953). The effect of collisions upon the Doppler widths of spectral lines. *Phys. Rev.,* Vol. 89, 472–473.

Donovan, D. P., A. C. A. P. van Lammeren, R. J. Hogan, H. W. J. Russchenberg, A. Apituley, P. Francis, J. Testud, J. Pelon, M. Quante, and J. Goddard (2001). Cloud effective particle size and water content profile retrievals using combined lidar and radar observations - 2. Comparison with IR radiometer and in situ measurements of ice clouds. *J. Geophys. Res,* Vol. 106, No. (D21), 27449 – 27464. 5.2.1

Frankenberg, C., U. Platt, and T. Wagner (2004). Retrieval of CO from SCIAMACHY onboard ENVISAT: detection of strongly polluted areas and seasonal patterns in global CO abundances. *Atmos. Chem. Phys. Discuss.,* Vol. 4, 8425 8438. 2.3

Funk, O. (1996). Bestimmung optischer Weglängenverteilungen mittels Absorptionsspektroskopie an der Sauerstoff A-Bande. Diploma thesis, University of Heidelberg, Heidelberg, Germany. D533. 1, 5

Funk, O. (2000). *Photon Pathlengths Distributions for Cloudy Skies - Oxygen A-Band Measurements and R Radiative Transfer Model Calculations.* Ph. D. thesis, Institut für Umweltphysik, Ruprecht-Karls-Universität Heidelberg. 1, 2.3, 3.4.1, 3.7

Funk, O. and K. Pfeilsticker (2003). Photon path length distributions for cloudy skies: Oxygen A-Band measurements and model calculations. *Annal.Geophysicae,* Vol. 21, 615 – 626. 6

Galatry, L. (1961). Simultaneous effect of Doppler and foreign gas broadening on spectral lines. *Phys. Rev.,* Vol. 122, No. 4, 1218–1223.

Gamache, R. R., A. Goldman, and L. S. Rothman (1998). Improved Spectral Parameters for the Three Most Abundant Isotopomers of the Oxygen Molecule. *J. Quant. Spectr. Rad. Trans.,* Vol. 59, No. 3-5, 495–509. 2.1

GOME (1995). *GOME, Global Ozone Monitoring Experiment, users manual.* European Space Research and Technology Centre (ESTEC), Frascati, Italy: ESA Publication Division (SP-1182), edited by F. Bednarz. 2.3

Goody, R. and Y. Yung (1989). *Atmospheric Radiation - Theoretical Basis.* Oxford University Press.

Grainger, J. R. and J. Ring (1962). Anomalous Fraunhofer line profile. *Nature,* Vol. 193, 762. 2.2.3

Greiner, B. (1998). Aufbau und Charakterisierung eines hochauflösenden Gitterspektrographen. Diploma thesis, University of Heidelberg, Heidelberg, Germany. D568. 1, 5

Guzzi, R., J. Burrows, T. Kurosu, V. Rozanov, K. Chance, P. Watts, and K. Muirhead (1994). *A study of cloud detection*. ESA/ESTEC: Report for ESA Contract 10997/94/NL/CN. 2.4.1

Haken, H. and H. C. Wolf (1994). *Molekülphysik und Quantenmechanik: Einführung in die experimentellen und theoretischen Grundlagen* (2. ed.). Berlin, Heidelberg, New York: Springer. 2.4

Haug, H. (1996). Raman-Streuung von Sonnenlicht in der Erdatmosphäre. Diploma thesis, University of Heidelberg, Heidelberg, Germany. D467.

Heidinger, A. K. and G. L. Stephens (1998). *Nadir sounding of clouds and aerosol in the O_2-A-band* (Atmos. Science Blue Book 650 ed.). Colarado State University, Fort Collins, CO 80523-1371: Dept. of Atmospheric Science. 2.4.1

Heidinger, A. K. and G. L. Stephens (2000). Molecular Line Absorption in a Scattering Atmosphere. Part II: Application to Remote Sensing in the O_2 A band. *J. Atmos. Sci.,* Vol. 57, No. 10, 1615–1634. 2.4.1, 4.2

Herzberg, G. (1950). *Molecular Spectra and Molecular Structure Volume I - Spectra of Diatomic Molecules* (second edition ed.). Malabar, Florida: Robert E. Krieger Publishing Company. 2.4

Heue, K.-P., A. Richter, T. Wagner, M. Bruns, J. Burrows, C. v. Friedeburg, W. Lee, U. Platt, I. Pundt, and P. Wang (2004). Validation of SCIAMACHY tropospheric NO_2-columns with AMAXDOAS measurements. *Atmos. Chem. Phys. Discuss.,* Vol. 4, 7513–7540. 2.3

Houghton, J., Y. Ding, D. Griggs, M. Noguer, P. van der Linden, X. Dai, K. Maskell, and C. Johnson (2001). *IPCC, 2001: Climate Change 2001: The Scientific Basis. Contribution of Working Group I to the Third Assessment Reoprt of the Intergovernmental Panel on Climate Change*. Cambridge University Press. 1.1

Hulst, H. C. v. d. (1957). *Light Scattering by Small Particles*. New York: Dover Publications, Inc. 3.3

Kokhanovsky, A. and V. Rozanov (2004). The physical parameterization of the

top-of-atmosphere reflection function for a cloudy atmopshere - underlying surface system: the oxygen A-band case study. *JQSRT,* Vol. 85, 35 – 55. 2.4.1

Kurucz, R. L., I. Furenlid, J. Brault, and L. Testerman (1984). *Solar Flux Atlas from 296 to 1300 nm.* Sunspot, New Mexico, U.S.A.: National Solar Observatry. 3.7

Levkov, L., B. Rockel, H. Kapitza, and E. Raschke (1992). 3D mesoscale numerical studies of cirrus and stratus clouds by their time and space evolution. *Contrib. Atmos.Phys.,* Vol. 65, 35 – 58.

Macke, A., D. Mitchell, and L. v. Bremen (1999). Monte Carlo radiative transfer calculations for inhomogenous mixed phase clouds. *Phys.Chem.Earth (B),* Vol. 24, No. 3, 237 – 241.

Marshak, A. and A. Davis (2005). *3D radiative transfer in cloudy atmospheres.* Berlin, Heidelberg, New York: Springer.

Marshak, A., A. Davis, W. Wiscombe, and R. Cahalan (1995). Radiative smoothing in fractal clouds. *J. Geophys. Res.,* Vol. 100, No. D12, 26247–26261. 3.3

Mie, G. (1908). Beiträge zur Optik trüber Medien, speziell kolloidaler Metallösungen. *Annalen der Physik,* Vol. 4, No. 25, 377–445. 2.2.2

Min, Q.-L., L. Harrison, and E. Clothiaux (2001). Joint statistics of photon path-length and cloud optical depth: Case studies. *J. Geophys. Res.,* Vol. 106, 7375–7386. 1, 6

Min, Q.-L., L. Harrison, P. Kiedron, and J. Berndt (2004). A high-resolution oxygen A-band and water vapor spectrometer. *J. Geophys. Res.,* Vol. 109, No. D02202, 10.1029/2003JD003540. 1

MINUIT (1992). *CERN Program Library Long Writeup D506: MINUIT, Function Minimazation and Error Analysis, Reference Manual.* Geneva, Switzerland: CERN Application Software Group. 3.5.1

Nägele, U. (2002). Vergleich von Sauerstoff A-Banden Messungen im Himmelsstreulicht mit einem Gitter- und einem Fouriertransform - Spektrometer. Diploma thesis, University of Heidelberg, Heidelberg, Germany. D668. 4.1

Nicolet, M. (1984). On the Molecular Scattering in the Terrestrial Atmosphere: An Empirical Formula for its Calculation in the Homosphere. *Planet. Space Sci.,* Vol. 32, No. 11, 1467–1468. 2.2.1

NOAA (1976). *US Standard Atmosphere* (NOAA-S/T76-1562, Supplement Documents ed.)., pp. 50 – 216. Washington DC: US Printing Documents. 3.7

Penndorf, R. (1957). Tables of the refractive index for standard air and the rayleigh scattering coefficient for the spectral region between 0.2 and 200 μ and their application to atmospheric optics. *J.Opt. Soc. Am.,* Vol. 47, No. 2, 176–182. 2.2.1

Pfeilsticker, K. (1999). First geometrical path lengths probability density function derivation of the skylight from spectroscopically highly resolving oxygen Aband observations 2. Derivation of the Lévyindex for the skylight transmitted by midlatitude clouds. *J. Geophys. Res.,* Vol. 104, No. D4, 4101–4116. 6

Pfeilsticker, K., F. Erle, O. Funk, L. Marquard, T. Wagner, and U. Platt (1998). Optical path modifications due to tropospheric clouds: Implications for zenith sky measurements of stratospheric gases. *J. Geophys. Res,* Vol. 103, 25323 – 25335. 6

Pfeilsticker, K., F. Erle, O. Funk, H. Veitel, and U. Platt (1998). First geometrical path lengths probability density function derivation of the skylight from spectroscopically highly resolving oxygen Aband observations 1. Measurement technique, atmospheric observations, and model calculations. *J. Geophys. Res.,* Vol. 103, No. D10, 11483–11504. 1, 5.3

Platt, U. (1994). Differential optical absorption spectroscopy (DOAS). In W. M. Sigrist (Ed.), *Air Monitoring by Spectroscopic Techniques*, Volume 127, pp. 27–84. John Wiley & Sons, Inc.

Platt, U., D. Perner, and H. Pätz (1979). Simultaneos measurement of atmospheric CH_2O, O_3 and NO_2 by differential optical absorption. *J. Geophys. Res.,* Vol. 84, 6329–6335.

Platt, U. and J. Stutz (2004). *Differential Optical Absorption Spectroscopy: Principles and Application.* Springer.

Polonski, I. and A. Davis (2004). Lateral photon transport in dense scattering and weakly-absorbing media of finite thickness: Asymtotic analysis of the space-time Green function. *J. Opt. Soc. Am. A,* Vol. 21, 1018 – 1025.

Quante, M., H. Lemke, H. Flentje, P. Francis, and J. Pelon (2000). Boundaries an internal structure of mixed phaes clouds as deduced from ground-based

95-Ghz Radar and airborne Lidar measurements. *Phys. Chem. Earth,* Vol. 25, No. 10 - 12, 889 – 895. 5.2.1

Ritter, K. J. and T. D. Wilkerson (1987). High resolution spectroscopy of the oxygen A-band. *J. Molec. Spectrosc.,* Vol. 121, 1–19. 3.4.2

Roscoe, H. K., D. J. Fish, and J. R. L. (1996). Interpolation errors in UV-visible spectroscopy for stratospheric sensing: implications for sensitivity, spectral resolution, and spectral range. *Applied Optics,* Vol. 35, No. 3, 427–432. 4.1.1

Rose, T., S. Crewell, U. Löhnert, and C. Simmer (2005). A network suitable microwave radiometer for operational monitoring of the cloudy atmosphere. *Atmospheric Research,* Vol. 7, 183 – 200. 5.2.2

Rothman, L., A. Barbe, D. Chris Benner, L. Brown, C. Camy-Peyret, M. Carleer, K. Chance, C. Clerbaux, V. Dana, V. Devi, A. Fayt, J.-M. Flaud, R. Gamache, A. Goldman, D. Jacquemart, K. Jucks, W. Lafferty, J.-Y. Mandin, S. Massie, V. Nemtchinov, A. Newnham, D, A. Perrin, C. Rinsland, J. Schroeder, K. Smith, M. Smith, K. Tang, R. Toth, J. Vander Auwera, P. P. Varanasi, and K. K. Yoshino (2003). The HITRAN molecular spectroscopic database: edition of 2000 including updates though 2001. *J. Quant. Spectroscopy and Rad. Transfer,* Vol. 82, 5–44. 3.4.2, 4.5.2, A.1

Rozanov, V., A. Kokhanovsky, and J. Burrows (2004). The determination of cloud altitude using GOME reflectance spectra: Multilayered cloud systems. *IEEE Trans. Geosci. and Remote Sens.,* Vol. 42, 1009– 1017. 2.4.1

Sanghavi, S. (2005). Online tool for Mie phase function calculation. http://cezanne.iup.uni-heidelberg.de/˜sanghavi/mie_doc/.

Savigny, C. v., O. Funk, U. Platt, and K. Pfeilsticker (1999). Radiative Smoothing in Zenith-Scattered Skylight Transmitted Through Optically Thick Clouds to the Ground. *Geophys. Res. Lett.,* Vol. 26, No. 19, 2949–2952. 3.1.4

Scheirer, R. (2001). *Solarer Strahlungstransport in der inhomogenen Atmosphäre.* Ph. D. thesis, Institut für Meereskunde, Christian-Albrechts-Universität Kiel. Nr. 322. 4.5.2

Scheirer, R. (2002). *Grimaldi User Manual, Version 0.9.* Institut für Meereskunde, Christian-Albrechts-Universität Kiel. 4.5.2

Scheirer, R. and A. Macke (2003). Cloud-Inhomogeneity and Broadband Solar

Fluxes. *J. Geophys. Res,* Vol. 108, No. D19, 4599, doi:10.1029/2002JD003321. 6

Schmidt, S., K. Lehmann, and M. Wendisch (2004). Minimizing instrumental broadening of the drop size distribution with the M-Fast-FSSP. *J. Atmos. and Oceanic Tech,* Vol. 21, 1855 – 1867. 5.2.1

Scholl, T., K. Pfeilsticker, A. Davis, H. K. Baltink, S. Crewell, U. Löhnert, C. Simmer, J. Meywerk, and M. Quante (2004). Path length distributions for solar photons under cloudy skies: Comparison of measured first and second moments with predictions from classical and anomalous diffusion theories. *J. Geophys. Res.,* Vol. revised.

Sioris, C. E. and W. F. J. Evans (1999). Filling in of Fraunhofer and gas-absorption lines in sky spectra as caused by rotational Raman scattering. *Appl. Opt.,* Vol. 38, No. 12, 2706–2713.

Sopra. *UHRS Monochromators Operating Manual.* Sopra. 4.1.1

Stephens, G. L. and A. K. Heidinger (2000). Molecular Line Absorption in a Scattering Atmosphere. Part I: Theory. *J. Atmos. Sci.,* Vol. 57, No. 10, 1599–1614. 2.4.1, 4.2

Stutz, J. and U. Platt (1996). Numerical analysis and estimation of the statistical error of differential optical absorption spectroscopy measurements with least-squares methods. *Applied Optics,* Vol. 35, No. 30, 6041–6053.

Trick, S. (2004). *Formation of nitrous acid on urban surfaces.* Ph. D. thesis, Institut für Umweltphysik, Ruprecht-Karls-Universität Heidelberg. 2.3

Van de Hulst, H. C. (1980). *Multiple Light Scattering, Tables, Formulas and Applications, Volume 1 and 2.* London: Academic Press.

Veitel, H. (1997). Messungen atmosphärischer Photonenweglängen für verschiedene meteorologische Situationen. Diploma thesis, University of Heidelberg, Heidelberg, Germany. D555. 5

Veitel, H., O. Funk, C. Kurz, U. Platt, and K. Pfeilsticker (1998). Geometrical pathlength probability density functions of the skylight transmitted by mid-latitude cloudy skies: Some case studies. *Geophys. Res. Lett.,* Vol. 25, No. 17, 3355–3358. 1

Volkamer, R. (2001). *A DOAS Study on the Oxidation Mechanism of Aromatic Hydrocarbons under Simulated Atmospheric Conditions*. Ph. D. thesis, Institut für Umweltphysik, Ruprecht-Karls-Universität Heidelberg. 2.3

Wagner, T., F. Erle, L. Marquard, C. Otten, K. Pfeilsticker, T. Senne, J. Stutz, and U. Platt (1998). Cloudy Sky Optical Paths as derived from DOAS Observations. *J. Geophys. Res,* Vol. 103, 25307 – 25321. 6

Wagner, T. and U. Platt (1998). Satellite mapping of enhanced BrO concentrations in the troposphere. *Nature,* Vol. 395, 486–490. 2.3

Wendisch, M., P. Pilewskie, E. Jäkel, S. Schmidt, J. Pommier, S. Howard, H. Jonsson, H. Guan, M. Schröder, and B. Mayer (2004). Airborne measurements of areal spectral surface albedo over different sea and land surfaces. *J. Geophys. Res.,* Vol. 109, doi:10.1029/2003JD004392. 3.9.1

Yamamoto, G. and D. Q. Wark (1961). Discussion of the Letter by R. A. Hanel, 'Determination of Cloud Altitude from a Satellite'. *J. Geophys. Res.,* Vol. 66, No. 10, 3596.

Acknowledgements

First of all, i want to take this opportunity to say 'thank you' to all the people who supported me during my PhD. The successful completion of this thesis would not be possible without the support and promotion on various fields.

I would like to express my gratitude to my supervisor Prof. Klaus Pfeilsticker for his inspiring and encouraging discussions and for the possibility to write this thesis. I also want to thanks to my second referee Prof. Frank Arnold for his survey of this thesis. I also would like to thanks Prof. Ulrich Platt for many fruitful discussions.

I want to thank all people from the institute who joint me during this thesis, namely Andre Butz, Marcel Dorf, Andreas Lotter, Jutta Zingler, Thierry Marbach, Christoph Kern, Roland von Glasow and Susanne Marquart. I also have to mention Frank Weidner, Sebastian Trick, Markus Pettinger and Nicolas Latuske for the great time in our office and Ulrich Nägele for his support during the BBC1 campaign.

I would like to thank all participants of the BBC1 and BBC2 campaign in Cabauw. I had a great time there and learned a lot. Thank you very much to Willem Hovius, Andre van Lammeren, Arnout Feijt and Henk Klein Baltink from KNMI for organisation both campaigns and for providing access to Cabauw. Also thanks for providing the cloud radar and ceilometer data for both campaigns. The people from GKSS, Gesthaacht, namely Markus Quante, Oliver Sievers and Jens Meywerk thanks for the cloud radar data and for teaching me, how to interpret these data. For the microwave and liquid water path data i thank the people from the University of Bonn Clemens Simmer and Victor Venema and from the University of Munich Susanne Crewell and Ulrich Löhnert. I thank Alexander Marshak, NASA/Goddard and Anthony Davis, Los Alamos National Labs for many inspiring and interesting discussions. Also thanks to Clemens Barfus from the University of Dresden for the satellite images.

I would like to thank everybody from the IUP mechanics and electronics workshop for their support and their fast and uncomplicated help setting up the instrument and adapting the instrument. It has always been finished yesterday.

I thank my parents for their support during my study and my PhD thesis.

Finally special thanks to my wife Jana who supported me the whole time and for so many things I cannot write them down here.